

# Doctoral Dissertation

## A Soft Robotic Skin with Integrated Optical Sensing and Jamming Mechanism

Tatsuya Sakuma

September 30, 2023

Graduate School of Information Science  
Nara Institute of Science and Technology

A Doctoral Dissertation  
submitted to Graduate School of Information Science,  
Nara Institute of Science and Technology  
in partial fulfillment of the requirements for the degree of  
Doctor of ENGINEERING

Tatsuya Sakuma

Thesis Committee:

Professor Takamitsu Matsubara	(Supervisor)
Professor Takahiro Wada	(Co-supervisor)
Assistant Professor Hikaru Sasaki	(Co-supervisor)
Assistant Professor Takuya Kiyokawa	(Co-supervisor)

# A Soft Robotic Skin with Integrated Optical Sensing and Jamming Mechanism\*

Tatsuya Sakuma

## Abstract

To enable robots to manipulate objects with capabilities comparable to the human hand, improvements in tactile sensing and grasping performance are essential. In this research, we propose a novel soft robotic skin, combining vision-based sensing and a jamming mechanism, to enhance tactile sensing and grasping abilities. By incorporating transparent beads and transparent oil with an adjusted refractive index, our soft skin achieves high spatial resolution tactile sensing through vision-based methods. Additionally, the control of skin stiffness is achieved by utilizing the jamming transition of the filled transparent beads, enabling effective grasping. To establish the practicality of our concept, we design and test three robotic devices, namely a gripper, fingertips, and a jig, that utilize the proposed robotic skin. First, we designed a ball-shaped gripper capable of sensing skin deformation and grasping objects through granular jamming. Next, we developed a miniaturized fingertip device. This fingertip device was less than half the size of a ball-type gripper yet functioned correctly for parallel gripper and successfully grasped both fragile objects and heavy objects. Finally, we created a soft jig that ensured object fixation and accurate pose estimation even when its size was doubled from the ball-type gripper. The results confirm that the proposed skin structure is achievable to enhance tactile sensing and grasping capabilities and can be used as a scalable basic element in robotic applications.

## Keywords:

Soft Material Robotics, Sensors, Mechanism Design, Grippers, Sensor-based Control

---

\*Doctoral Dissertation, Graduate School of Information Science, Nara Institute of Science and Technology, September 30, 2023.

# 光学センシングとジャミング機構を 統合したソフトロボットスキン\*

佐久間 達也

## 内容梗概

ロボットへ人の手のように万能な物体操作能力を実現するためには、触覚センシングと把持性能の向上が不可欠である。本研究では、触覚センシングと把持能力を向上させるために、視覚に基づくセンシングとジャミング機構を組み合わせた新しいソフトロボットスキンを提案する。屈折率を調整した透明ビーズと透明オイルを組み込むことで、提案ソフトロボットスキンはビジョンベース手法による高空間分解能の触覚センシングを実現する。さらに、充填された透明ビーズのジャミング転移現象を利用することで、皮膚の硬さ制御による把持を実現する。提案手法の実用性を確立するために、提案するソフトロボットスキンを利用したグリッパー、指先デバイス、柔軟治具を開発した。はじめに、皮膚の変形を感知し、粒状ジャミングによって物体を把持できるボール型グリッパーを開発した。このグリッパは物体へボール部を押し付けるだけで、ジャミング機構による把持が可能であり、なおかつその際のボール部の変形をセンシングすることが可能である。次に、ボール型グリッパーの半分以下の大きさである小型指先デバイスを開発した。この指先デバイスによって、平行グリッパはセンシングに基づく脆弱物体把持と、ジャミング機構による重量物把持の両方を実現することができる。最後に、ボール型グリッパーの倍の大きさを持つ柔軟治具を開発し、物体固定と正確な物体姿勢推定が可能であることを確認した。これらの結果より、提案ソフトロボットスキンは、様々なサイズのロボットアプリケーションに対して触覚センシングと把持能力を向上させることが可能であり、把持のための基本構造として活用可能であることが示された。

## キーワード

ソフトロボティクス, 触覚センサ, 機構設計, ロボットグリッパ, 把持制御

---

\*奈良先端科学技術大学院大学 情報科学研究科 博士論文, 2023年9月30日.

# Contents

<b>1. Introduction</b>	<b>1</b>
1.1 Background . . . . .	1
1.2 Related work . . . . .	3
1.2.1 Gripper . . . . .	3
1.2.2 Sensor . . . . .	3
1.2.3 Fingertip device for improved grasping . . . . .	5
1.2.4 Jig . . . . .	5
1.3 Research purpose . . . . .	6
1.4 Contributions . . . . .	7
1.5 Thesis organization . . . . .	7
<b>2. Proposed soft robotic skin</b>	<b>8</b>
2.1 Overview . . . . .	8
2.2 Proposed mechanism . . . . .	9
2.2.1 Filling materials . . . . .	9
2.2.2 Markers . . . . .	10
2.3 Optical Tactile Sensing . . . . .	13
2.3.1 Sensing method overview . . . . .	13
2.3.2 Preprocessing . . . . .	13
2.3.3 Deformation depth of the membrane . . . . .	16
2.3.4 Contact position and area . . . . .	16
2.3.5 Normal vectors and radius of curvature of the object surface . . . . .	16
2.3.6 Visualization of tactile information . . . . .	16
<b>3. Robotic devices development</b>	<b>18</b>
3.1 Introduction . . . . .	18
3.2 Universal gripper . . . . .	20
3.2.1 Design . . . . .	21
3.2.2 Fabrication . . . . .	21
3.3 Fingertip device . . . . .	25
3.3.1 Design . . . . .	25
3.3.2 Fabrication . . . . .	27

3.3.3	A strategy for the grasping actions . . . . .	28
3.4	Soft jig . . . . .	30
3.4.1	Design . . . . .	30
3.4.2	Fixing and Sensing System . . . . .	33
<b>4.</b>	<b>Sensing and grasping evaluation with developed robotic devices</b>	<b>40</b>
4.1	Evaluate universal gripper . . . . .	40
4.1.1	Tactile sensing . . . . .	40
4.1.2	Object grasping . . . . .	43
4.1.3	Simultaneous grasping and sensing . . . . .	45
4.1.4	Discussion . . . . .	47
4.2	Evaluate fingertip device . . . . .	48
4.2.1	Tactile sensing . . . . .	48
4.2.2	Fragile object grasping . . . . .	51
4.2.3	Heavy object grasping using jamming transition . . . . .	53
4.2.4	Stable grasping for manipulation . . . . .	55
4.2.5	Discussion . . . . .	59
<b>5.</b>	<b>Gentle grasping with a manipulator and a parallel gripper</b>	<b>60</b>
5.1	Introduction . . . . .	60
5.2	Experiment setup . . . . .	60
5.3	Object recognition . . . . .	61
5.4	Objects grasping and sensing . . . . .	62
5.5	Experiment . . . . .	63
5.6	Result . . . . .	67
5.7	Discussion . . . . .	69
<b>6.</b>	<b>Evaluate soft jig</b>	<b>70</b>
6.1	Jig Coordinate Calibration . . . . .	70
6.2	Pushed Object Pose Estimation . . . . .	78
6.3	Placed Object Fixing . . . . .	83
6.4	Fixing Force . . . . .	87

<b>7. Discussion</b>	<b>91</b>
7.1 Precise Estimation . . . . .	91
7.2 Hardware Limitations for Sensing . . . . .	91
7.3 Hardware Limitation for Fixing . . . . .	92
<b>8. Conclusion</b>	<b>93</b>
<b>Acknowledgements</b>	<b>95</b>
<b>References</b>	<b>96</b>

## List of Figures

1	Research objectives . . . . .	2
2	The spectrum of the design space dimension . . . . .	4
3	Mechanisms for granular jamming-based grasping . . . . .	9
4	Mixed oil with acrylic beads . . . . .	11
5	Three possible marker patterns . . . . .	12
6	Integration of proposed sensing system . . . . .	14
7	Circular markers embedded in the membrane . . . . .	15
8	Viewer tool illustrating the deformation of the gripper . . . . .	17
9	Base structure of the proposed robotic skin . . . . .	19
10	Structure of the proposed universal gripper . . . . .	20
11	Fabrication description of the membrane . . . . .	22
12	Fabrication description of the bulkhead . . . . .	24
13	Structure of the proposed fingertip gripper . . . . .	25
14	Mold for the membrane . . . . .	27
15	Fabrication of the membrane . . . . .	28
16	Grasping strategy using fingertip device . . . . .	29
17	Structure of the soft jig . . . . .	30
18	Appearance of the soft jig . . . . .	31
19	Mold to fabricate the membrane of the soft jig . . . . .	32
20	System configuration of the soft jig . . . . .	33
21	Oil level measurement system . . . . .	35
22	Appearance of markers . . . . .	36
23	Flowchart of the proposed membrane shape-sensing . . . . .	37
24	Point-to-function ICP to find a transformation . . . . .	38
25	Pre-processing to convert a CAD model into points . . . . .	39
26	Transparency of the granular filling . . . . .	41
27	Pins of different heights . . . . .	42
28	Membrane deformation while palpating pins . . . . .	42
29	Equipment used in the grasping experiment . . . . .	44
30	Cylindrical and rectangular objects . . . . .	45
31	A scene from the grasping experiments . . . . .	46
32	Tactile sensing with cylinders . . . . .	49



33	Deformation depth of the membrane with cylinders . . . . .	50
34	Experimental setup for fragile object grasping . . . . .	52
35	Grasping experiment with closed loop system . . . . .	52
36	Heavy grasping experiment using jamming transition . . . . .	54
37	Snapshots of the pouring motion . . . . .	56
38	Electrical and piping system connected to the pump . . . . .	57
39	Tilt angle of the cup at each trial measured by the IMU . . . . .	58
40	The grasping states when manipulating a cup filled with beads . . .	58
41	Grasping system configuration using tactile information . . . . .	61
42	Experimental setup for automatic grasping system . . . . .	62
43	Depth camera with retro-reflective markers . . . . .	63
44	Chronology of the object grasping and sensing . . . . .	65
45	Joint angle limitation of the parallel gripper . . . . .	65
46	Sensing result from reached goal position . . . . .	68
47	Experimental setup for soft jig . . . . .	71
48	Three cylindrical objects with different diameters . . . . .	72
49	Illustration of the motion of the robot to press the object . . . . .	72
50	Tilt angles and residuals before calibration . . . . .	74
51	Estimated tilt angles and their residuals after calibration (50 mm)	75
52	Estimated tilt angles and their residuals after the calibration (30 mm)	76
53	Estimated tilt angles and their residuals after the calibration (80 mm)	77
54	Variations of the positions that the robot pressed on the jig . . . .	79
55	Setup to evaluate the estimation performance of the soft jig . . . .	79
56	Tilt estimation results around the y-axis and the ground truth measured by motion capture . . . . .	81
57	Position estimation results in the x-direction and the ground truth measured by motion capture . . . . .	82
58	Estimated tilt angles from pressed to fixed . . . . .	84
59	Displacements from pressed to released . . . . .	85
60	Difference between pushed and released pose . . . . .	86
61	Measurement results of the torque exerted by the driver . . . . .	88
62	Screw tightening experiment . . . . .	89
63	Rotation angle of the object during screw tightening . . . . .	90

## List of Tables

1	Selection of possible filling materials . . . . .	10
2	Fluid actuation methods for jamming transition. . . . .	34
3	Performance when grasping long cylinders . . . . .	43
4	Performance when grasping dumbbells . . . . .	53
5	Performance when pouring beads without slipping the cup . . . . .	55
6	Target objects to test the accuracy of grasping and sensing . . . . .	66
7	Results of grasping and sensing accuracy . . . . .	67
8	Capabilities of proposed skin in acquiring tactile information and potential extensions . . . . .	94

# 1. Introduction

## 1.1 Background

What is the suitable robot hand to manipulate objects? In most cases, robot hands have been developed depending on the applications and the environments. However, the robot should be able to work like the human in a wide range of environments that are not set for the robot such as manufacturing factories. To that end, robot hands will need robust grasp and sense like the human hand. Specifically, it is important that the robot hand has softness like a human skin to allow object grasping with a large contact area and to acquire tactile information sensitively.

The human hand is a very universal and complex grasping tool that can recognize and handle objects. Its remarkable elastic properties, frictional properties, sensing accuracy and sensing resolution allow us for various manipulations [1]. For example, in the kitchen we can handle extremely fragile foods and manipulate heavy objects like a skillet without spilling the ingredients inside.

Tactile sensing is a particularly important factor in the above example. It would be very difficult unless the grasping force is evaluated according to identification of the object properties. Not only that tactile sensing allows us to supplement sight and to compensate for the uncertainty caused by occlusions when the human approaches the target object.

In addition to tactile sensing, improved robust grasping is also required to manipulate a wide variety of objects like a human. This is to achieve a powerful grasping that does not rely solely on force control using information feedback from sensor to the gripper.

The human hand, with its intricate blend of elastic and frictional properties, high sensing accuracy, and superior sensing resolution, serves as a remarkable model for advanced robotic manipulation. These features enable humans to execute a wide array of tasks, ranging from delicately holding fragile items to firmly gripping heavy objects. As illustrated in Fig. 1, the vision is to capture the essence of this functionality using a streamlined configuration. This minimalistic approach aims to concentrate on core attributes that mirror the human hand's versatility and adaptability in robotic applications.

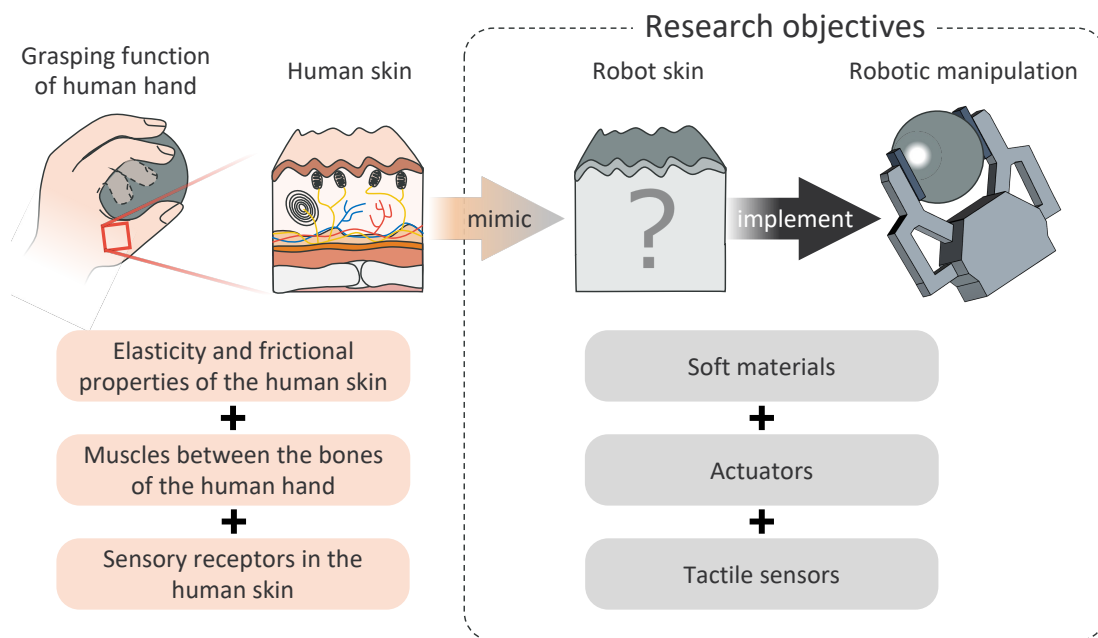


Figure 1: Research objectives

## 1.2 Related work

This research focuses on the sensing and grasping functions of grippers with rigid or soft body. Therefore, we explain related research divided into three sections: grippers, sensors, fingertip devices for improved grasping, and jigs.

### 1.2.1 Gripper

Many works on grippers have concentrated on rigid materials, but the morphologies are diversified depending on the field called Soft Robotics.

Hughes *et al.* [2] summarized soft grippers and they drew the spectrum of the design space dimension (Fig. 2). At start of the spectrum is a finger-based manipulator, which is a common type of gripper. Among these, parallel gripper with only two fingers are used widely not only in research fields but also in manufacturing factories.

At one end of the spectrum is the universal gripper which uses the jamming transition to grasp objects [3]. It attracts attention because it is able to grasp a wide variety of objects using a simple mechanism. This gripper conforms to the target object's shape, and then holds the object in place when air is evacuated out of the gripper, causing the granular filling to jam and the gripper's shape to become rigid.

As shown in the Fig. 2, it can be said that these two morphologies are in contrast with the universality of grasping, ease of in-hand manipulation, and degree of freedom. In addition, we think that the degree of freedom can be rephrased as the difficulty of attaching sensors.

### 1.2.2 Sensor

There are various kinds of tactile sensors for robot hands to use tactile information in autonomous manipulation [4]. Among all of these, sensors with high spatial resolution like human hands are attracting attention because they provide much more object information such as pose, shape, and surface texture [5].

Many high resolution sensors have been developed based on multiple small sensors. Tenzer *et al.* developed tactile array sensors based on barometric pressure sensor chips with MEMS technology that have pressure and temperature

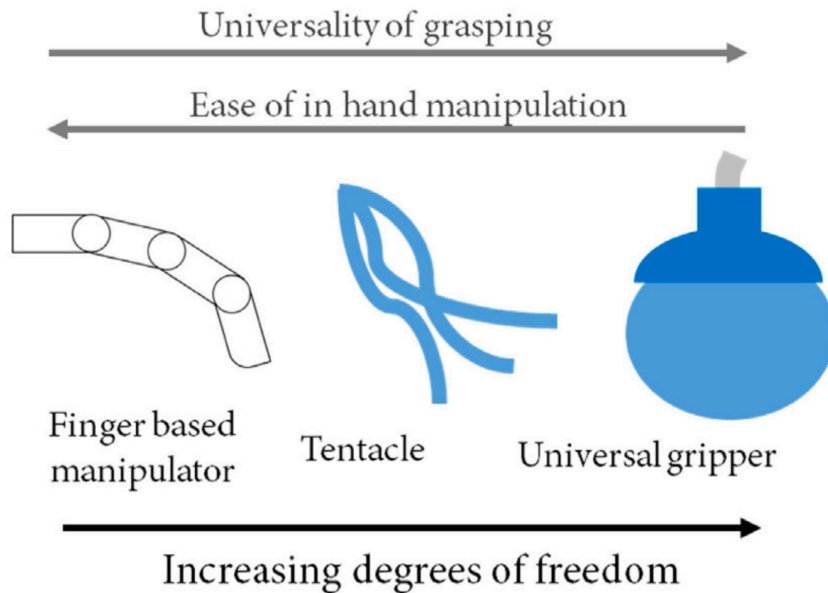


Figure 2: The spectrum of the design space dimension from [2]

sensing capabilities [6]. Tomo *et al.* measured three-axis force by monitoring magnetic field changes using a Hall-effect sensor and small magnets [7].

Also, various optical tactile sensing methods based on embedded cameras have been proposed and have achieved high spatial resolution [8]. The GelSight [9] and the GelSlim [10, 11, 12] sensors acquired various tactile information using an illumination source, a flexible gel membrane, and the pixel intensity values captured by an embedded camera. The TacTip family [13] sensors acquired tactile information by using an embedded camera to measure the motion of pins imitating the structure of the human skin. The FingerVision sensor [14] acquired object and external scene information by using a flexible transparent rectangular film with a grid of markers embedded. Ueda *et al.* [15] performed marker tracking through a transparent matrix and tracked the contact state by using a backlight to determine the onset of slippage. *SoftBubble* [16] [17] uses an air-inflated balloon to acquire the shape of the object with a depth camera through the balloon membrane. Lin *et al.* [18] proposed a sensor that estimates the curvature of a flexible material using the subtractive color-mixing principle.

These high resolution sensors have improved grasping performance incorpo-

rating slippage detection [19], [20], [21], hardness estimation [22], and regrasp [23], [24] using the tactile information.

In addition, sensors are being developed not only for mounting on fingertips, but also for application to large areas as skin [25, 26]. The multiple tactile modules method with electric circuits [27, 28] or the vision-based tactile sensing method [29, 30] is used for large-area sensing.

### 1.2.3 Fingertip device for improved grasping

In addition to tactile sensing, improved robotic gripper is also required to improve grasping performance for robot manipulation. Although parallel grippers are widely used in factories, they can only restrain the target object from two directions, which allows slippage in the remaining directions.

To improve the grasping performance of parallel grippers, fingertip devices have been developed. Many previous researchers added specific texture to the gripper surface to prevent slippage. Guo *et al.* created numerous texture prototypes because the interaction between the gripper and the object surface is difficult to predict in simulation [31]. As a result, it showed higher performance than the texture imitating the gecko hand which had been highly evaluated in the past. Mizushima *et al.* developed deformable fingertip for stable grasping under both wet and dry conditions by combining texture and fluid fingertip [32].

Also, the granular jamming techniques were proposed to execute complex manipulation tasks with multi-finger grippers. Amend and Lipson developed a two-finger gripper called JamHand with pockets of granular material in the fingertips [33]. The JamHand showed dexterous in-hand manipulation such as cracking eggs, assembling LEGO blocks, and using chopsticks. Tsugami *et al.* also proposed a gripper using two universal-gripping fingertips [34]. This gripper can grasp objects quickly and silently by using reformed magnetorheological fluid as the inner filling material.

### 1.2.4 Jig

In factories, jigs as well as parallel grippers are devices that are used extensively. Positioning the target object with a jig designed based on the object shape facilitates precise and efficient robotic assembly [35, 36].

Modular jigs [37, 38] or reconfigurable jigs [39, 40, 41] fix objects and support their surfaces by rearranging or replacing multiple components according to the shape of the object. The ability to change a fixed configuration provides flexibility. Pin array jigs [42, 43, 44] use a shape-memorable mechanism to fix objects by constraining multiple points of an object with pins. When fixing components using pins, a high degree of freedom (DoF) facilitates flexibility. Flexible material jigs [45, 46] use elastomeric materials to deform the surface of the fixture depending on the object shapes to be fixed.

### 1.3 Research purpose

In this research, we aimed to build grippers with improved grasping and tactile performance.

The successful combination of both tactile sensing and more-constrained grasping would have a large impact on robust robotic manipulation. However, it is extremely difficult to apply the high resolution sensor to a gripper while maintaining a special surface shape or a high degree of freedom surface by soft materials. It is difficult to arrange the a multi-array sensor on a flexible surface if the surface is not a planar shape and three-dimensional deformable. It is also difficult to use the embedded camera-based sensor on a typical granular-jamming gripper because the texture and the interior filling material would obstruct the camera. Hughes and Iida proposed a method to calculate local deformation of large soft bodies with strain gages [47], [48], which they applied with some success to the membrane of a jamming-based gripper.

To achieve higher resolution sensing to gripper without sacrificing its functions, we develop a novel soft robotic skin by combining optical sensing and the jamming transition. We use granular jamming-based mechanism to improve grasping performance and tune the refractive indices of the interstitial fluid and granular filling to achieve a transparent filling. We also use a semi-transparent membrane with embedded markers to determine the gripper’s deformation and allow detection of the grasped object by optical sensing. In order to confirm the mechanism performance, three types of robotic devices are created with using the proposed mechanism based on universal gripper, parallel gripper, and jig.



## 1.4 Contributions

The contributions of this thesis are:

1. a mechanism combining both the tactile sense via optical sensing and improvement in the holding stability by tightly restraining the object using the jamming transition
2. a method to acquire tactile information even if a large part of the gripper surface is in contact with the object and the membrane is significantly deformed
3. the experimental results showed that our approach has merit, and that visual sensing and grasping can be performed simultaneously

## 1.5 Thesis organization

Section 2 first gives an overview of the proposed soft robotic skin, and then describes details of its hardware and software approaches. Section 3 describes developed robotic devices in details. Section 4 shows experiments using grippers, and the discusses the limitations. Section 5 shows an application of the parallel gripper with the tactile sensing. Section 6 concludes the thesis and suggests future work.

## 2. Proposed soft robotic skin

### 2.1 Overview

This is a soft robotic skin for robot grasping and sensing based on jamming transition and optical sensing by using transparent materials and flexible membrane with markers.

As shown in Fig. 3(a), ground coffee beans are commonly selected as the granular filling, with air for the interstitial fluid, so that a vacuum pump can be used to actuate the gripper in conventional universal grippers. Even if a camera is embedded in it, the filler materials will obstruct the camera.

This soft robotic skin is designed as shown in Fig. 3(b), therefore we achieve both a tactile sense via optical sensing and grasping capability by tightly restraining the object.

Our approach can be roughly divided into two parts to satisfy this design.

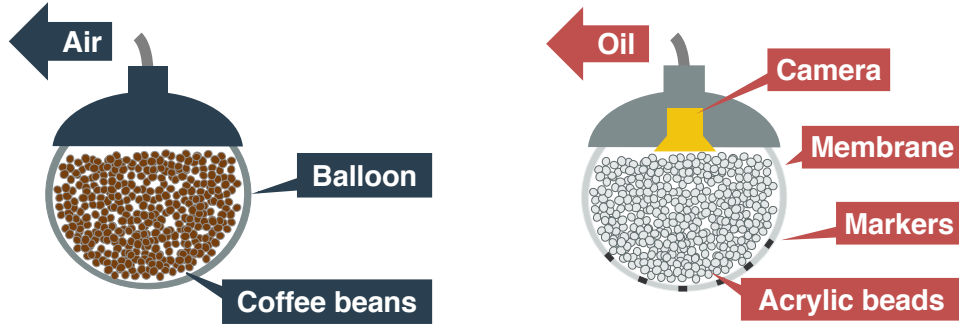
In the hardware part, we change the constituent material of the universal gripper. We set out to design a transparent filling, so that optical sensing can be used by changing the inner filling material and by changing the drive method from pneumatic to hydraulic.

In the software part, we achieve optical sensing using transparent elastomer membrane with markers. The markers on the elastomer membrane are used to obtain information about the contact and the deformation of the membrane.

This special structure handled by the hardware part is the key technology of this research, and the software part can not function without this structure.

By adding embedded markers and vision sensing to the granular jamming approach to grasping, we provide a way to:

- measure the deformation of the gripper, allowing palpation of the object and environment
- determine the grasped item and perform detection
- confirm grasp success and detect if an object fell from the grasp



(a) Conventional universal gripper that is pneumatic driven (b) Proposed mechanism with hydraulic drive

Figure 3: Mechanisms for granular jamming-based grasping

## 2.2 Proposed mechanism

We use the well-known mechanism for granular jamming-based grasping using a thin flexible membrane containing beads and oil to grasp or restrain objects. We also use a transparent filling and a semi-transparent membrane with markers to allow optical sensing.

The flexible membrane is deformed along the object shape and hardened by the pressure control inside the device. By using a transparent filling instead of using an opaque filling, markers can be captured by embedded camera.

In addition, our gripper design is hydraulically driven, thus it may generate significant increases in holding force by the incompressibility of the oil.

### 2.2.1 Filling materials

The filling materials requirements to develop proposed mechanism are:

1. colorless and transparent
2. liquid has a high refractive index and low viscosity
3. solid is non-deformable and has a low refractive index

Table 1: Selection of possible filling materials. Materials used in prototype are bolded.

Material	State	Refractive Index
Glycerol	Liquid	1.473
Vegetable Oil	Liquid	1.47 - 1.48
<b>Paraffin Oil</b>	Liquid	1.48
Sugar Solution	Liquid	1.47 - 1.49
<b>Silicone Oil</b>	Liquid	1.375 - 1.575
<b>Acrylic</b>	Solid	1.490 - 1.492
Crown Glass	Solid	1.485 - 1.755
Flint Glass	Solid	1.523 - 1.925

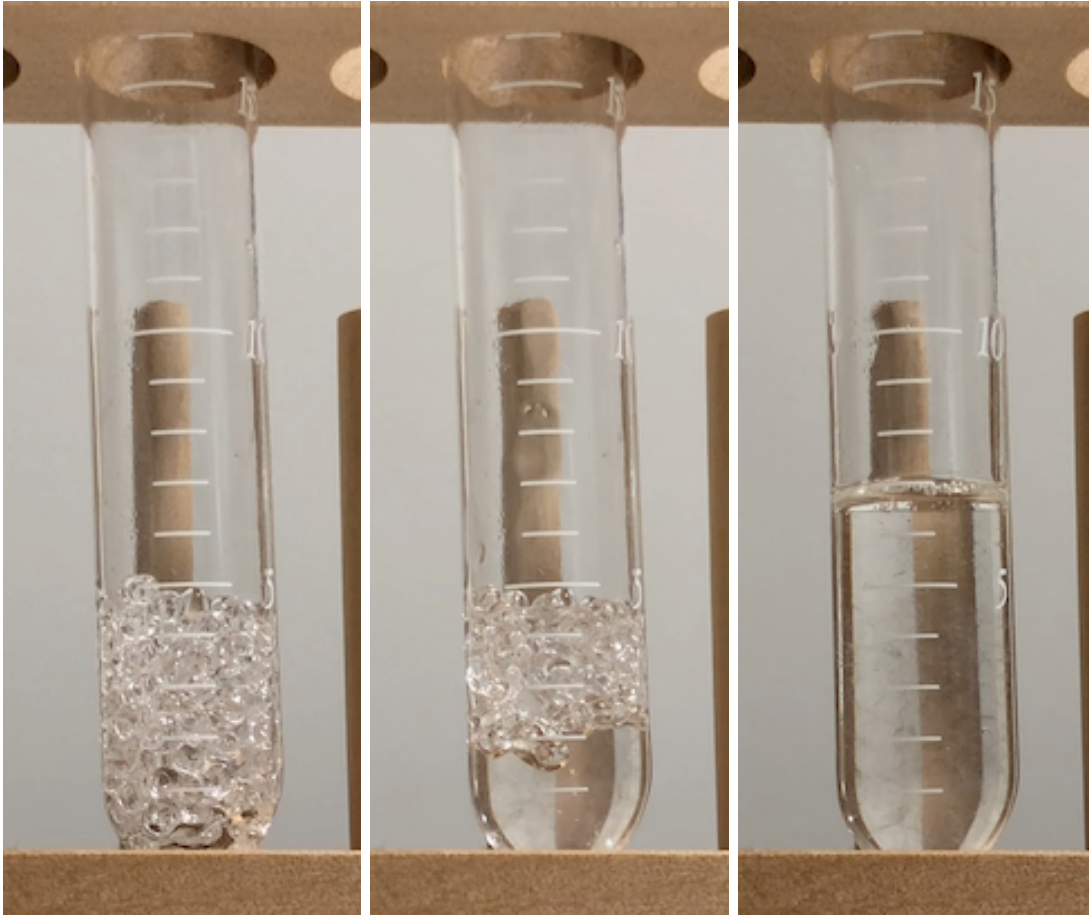
Table 1 shows possible filler materials. We selected the granular filling and interstitial fluid to maximize the transparency of the resulting mixture. First, we selected acrylic as the filling solid because of its small specific gravity, high transparency, and good workability. Second, we mixed paraffin oil and silicone oil to achieve a refractive index similar to that of acrylic, which is 1.49.

Fig. 4 shows the transparent medium after adjusting the refractive index of an oil mixture to the refractive index of the granular bodies.

### 2.2.2 Markers

It is necessary to consider different marker patterns, such as those shown in Fig. 5. In this case, the icosahedron base pattern is used to determine the position of the marker.

Ward-Cherrier *et al.* proposed increasing the efficiency of tactile information acquisition by using a concentric ray pattern [49]. However, since the sensing resolution decreases as the contact position of the object moves away from the center of the gripper, it is not ideal for this application. The golden spiral or the icosahedron pattern offers better sensing resolution outside of the center. We chose the icosahedron base pattern for its symmetry and due to the lack of concentricity in the golden spiral pattern.

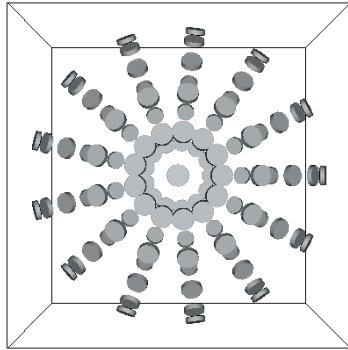


(a) Before immersion

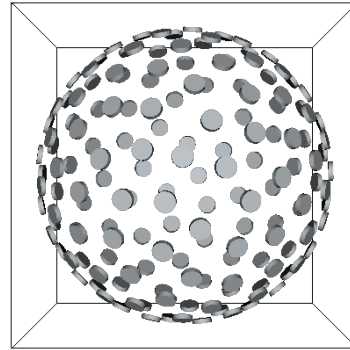
(b) Half immersed

(c) Completely immersed

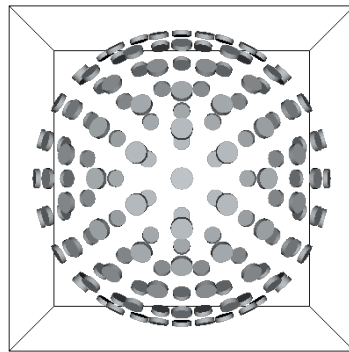
Figure 4: Mixed oil with acrylic beads. Beads are not visible if they are immersed because the refractive index of the beads are almost the same as oil.



(a) Rays



(b) Golden Spiral



(c) Icosahedron

Figure 5: Three possible marker patterns (we used c)

## 2.3 Optical Tactile Sensing

### 2.3.1 Sensing method overview

Fig. 6 shows the workflow of the optical tactile sensing and the object grasping when using the developed grippers. In this optical tactile sensing method, we can acquire tactile information with five element from membrane shape:

1. deformation depth on the membrane
2. object contact position
3. object contact area
4. object normal vector
5. object curvature radius

The membrane shape is acquired by wide angle camera using pinhole camera model and recognition of markers on the elastomer membrane filled with a transparent medium.

The image processing pipeline used in this analysis is based on C++ using ROS, OpenCV, PCL, and VTK libraries.

### 2.3.2 Preprocessing

In order to acquire tactile information, we calculate the three-dimensional position of the marker and estimate the membrane shape. By using the marker's pixel width and the pinhole camera model, we can calculate the three-dimensional position of the marker from the focal position of the camera. Also, in order to estimate the shape of the membrane including the part without the marker, surfaces are created from each neighboring markers' position.

As our camera used a fisheye lens, we first correct image distortion by calibrating it using the camera calibration algorithm proposed by Zhang *et al.* [50].

Then, markers are detected based on OpenCV blob detection. The input undistorted image was converted to grayscale image, and thresholding applied

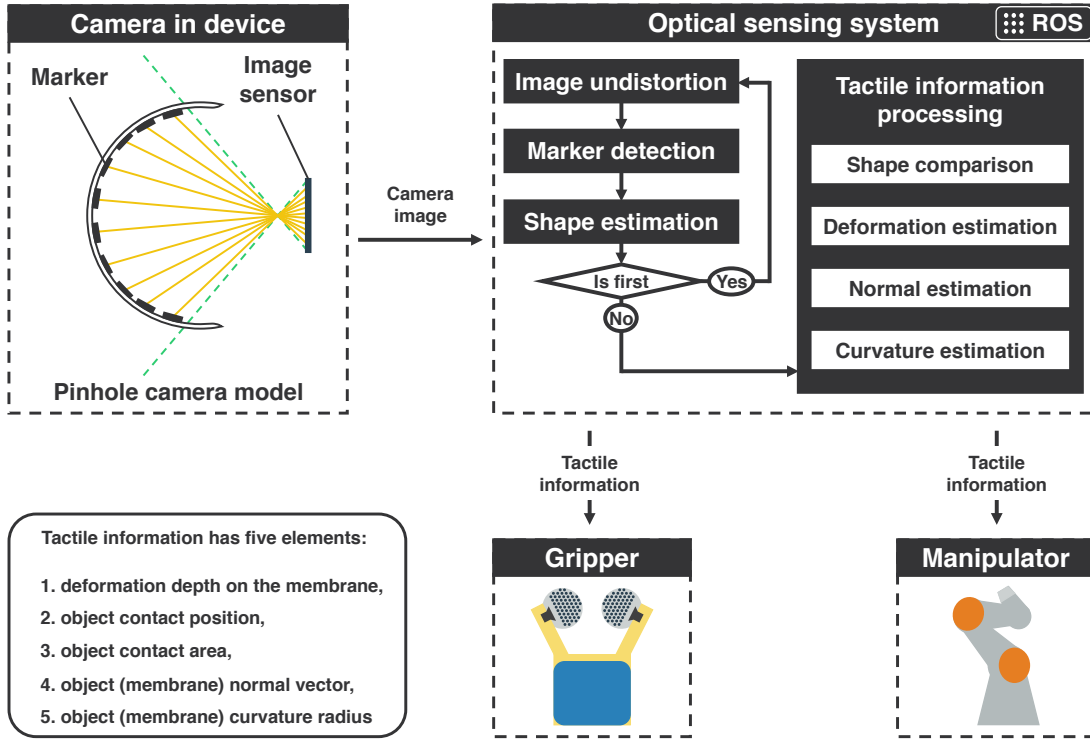


Figure 6: Integration of proposed sensing system

with several different thresholds. After that, connected components were extracted from every binary image using contour detection. For each image, grouping was performed using the blobs' position information, and median size blob information returned as the marker information.

Also, we estimate the shape of the marker to calculate its distance from the camera. As shown in Fig. 7, the diameter of the circular marker is twice the semi-major axis of the ellipse shown in the camera image. The semi-major and semi-minor axes were obtained using the ellipse fitting algorithm by Fitzgibbon *et al.* [51]. Using the detected marker's pixel size from the undistorted image, we can calculate the three-dimensional position by the following equations:



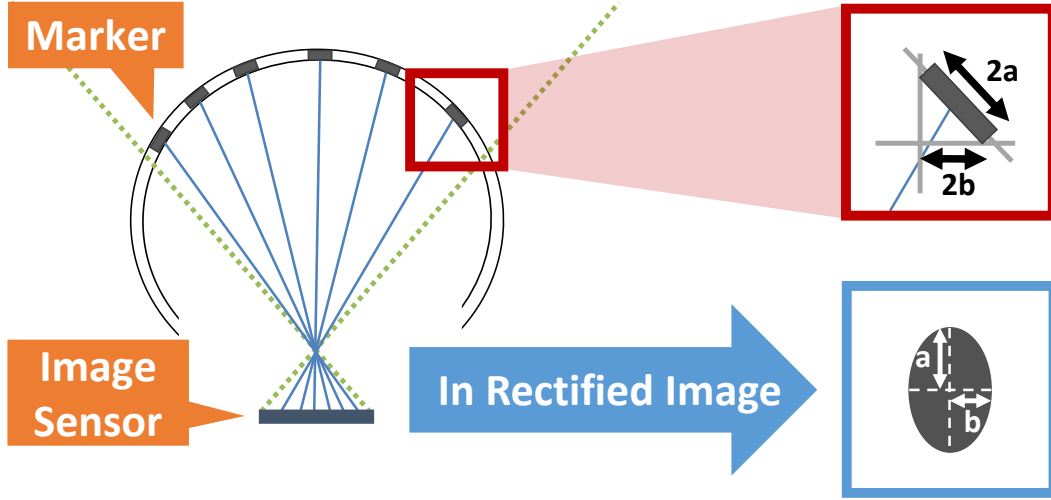


Figure 7: Circular markers embedded in the membrane are searched for in the camera images as ellipses

$$X = \frac{(u - c_x) \times O_{mm}}{O_{px}} \quad (1)$$

$$Y = \frac{(c_y - v) \times O_{mm}}{O_{px}} \quad (2)$$

$$Z = \sqrt{\left(\frac{f_x \times O_{mm} \times I_{px}}{O_{px} \times I_{mm}}\right)^2 - X^2} \quad (3)$$

where:

- $(u, v)$  : Coordinates of the object in pixel units
- $(c_x, c_y)$  : Principal point, usually at the image center
- $(f_x, f_y)$  : Focal length in metric units
- $O_{mm}$  : Object width in metric units
- $O_{px}$  : Object width in pixels
- $I_{mm}$  : Image sensor width in metric units
- $I_{px}$  : Image sensor width in pixels

When the membrane contacts the object, the marker deforms and appears as an ellipse in the image. Using the major axis of the ellipse as the marker width,

we adequately measure markers even if they are rotated into other orientations caused by more extreme deformation. The membrane shape can also be estimated by applying a Delaunay triangulation for a set of marker points in the two-dimensional plane.

### **2.3.3 Deformation depth of the membrane**

The membrane deformation is calculated as the distance between each marker's position and the nearest surface points on the initial membrane shape. This deformation can also be calculated by not comparing the initial membrane shape to the markers' new position but marker tracking. However, one issue with the device is that large marker displacements are difficult to track. Additionally, because the membrane is transparent to acquire object grasping information, marker positions are occasionally lost due to the influence of the outside world.

### **2.3.4 Contact position and area**

It is difficult to calculate the exact object contact position and contact area when the membrane is transparent, because the image intensity from the camera includes the information of not only the contact area but also the non-contact area. In this system, the maximum membrane deformation position is taken as the object contact position. The object contact area is calculated by approximating with the convex hull of the markers' position where the deformation amount is larger than the threshold value.

### **2.3.5 Normal vectors and radius of curvature of the object surface**

During grasping, the shape of the membrane can represent the shape of the contact object. The normal vectors and the radius of curvature of the contact object surface are estimated by performing an eigendecomposition using neighboring markers' position for each marker.

### **2.3.6 Visualization of tactile information**

By using the information about the three-dimensional position of the markers, we can visualize the three-dimensional shape of the gripper membrane and a normal

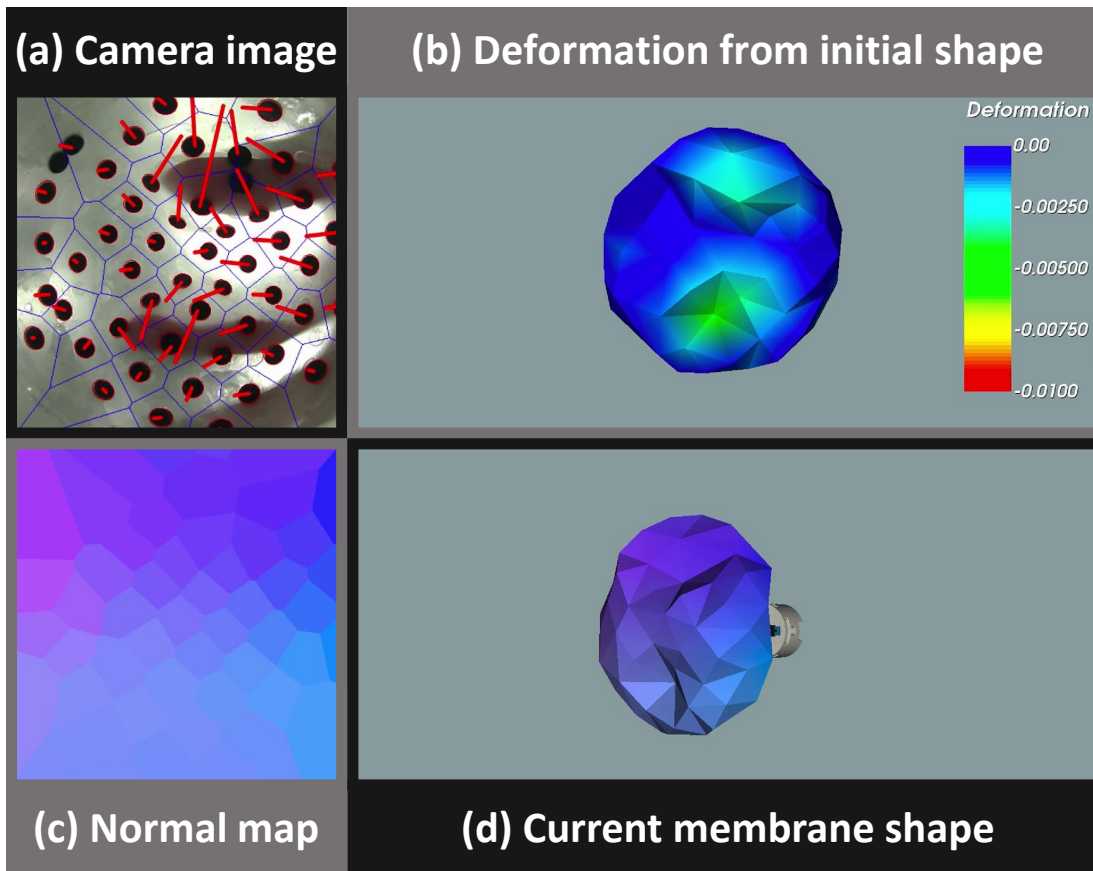


Figure 8: Viewer tool illustrating the deformation of the gripper

map superimposed on the camera image. Fig. 8 shows a viewer tool displaying this information. A normal map shown in Fig. 8(c) is uses the Voronoi diagram to define each marker area on the membrane, and these areas are painted with colors that indicate the normal directions.

## 3. Robotic devices development

### 3.1 Introduction

In developing the mechanism, we work on three types of robotic devices. First, we develop a universal gripper using optical sensing to show experimentally that a mechanism can acquire tactile information. Second, we develop a fingertip device for parallel gripper to grasp wide variety of objects. In addition, we develop a soft jig to fix assembly parts.

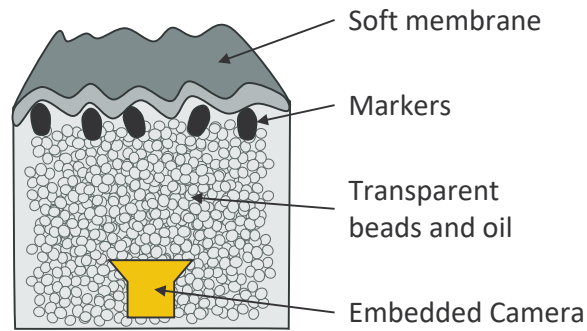
As illustrated in Fig. 9, the proposed mechanism is employed in various ways depending on the specific task at hand. For instance, grippers are utilized in underwater manipulations where tactile feedback is crucial for effective operation. In contrast, fingertip devices are utilized in food manipulation where force control is of paramount importance. Jig devices are particularly effective for assembly tasks that require manipulating a range of objects while simultaneously acquiring their orientation.

Fig. 9 (a) illustrates how to grasp and sense with a universal gripper. A universal gripper can grasp and palpate simultaneously by pressing itself only once against the object. The entire gripper surface is sensitive to deformation, effectively transforming it into a large tactile sensor that is also capable of palpating the environment to detect objects such as cables, irregularities, or obstacles. In addition, it is possible to grasp a contacted objects by hardening the deformed membrane.

Fig. 9 (b) illustrates how to leverage a fingertip device with a parallel gripper. Combining the granular jamming system with the parallel gripper enables us to grasp fragile or heavy object with low grasping force, because it can change the stiffness of the flexible membrane. The flexible membrane is deformed along the object shape and hardened by the pressure control inside the device. Also, tactile information helps to determine pushing depth and internal pressure.

Fig. 9 (c) illustrates how to fix and sense an object with a soft jig.

### Base structure of the proposed robotic skin

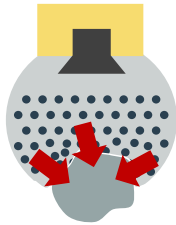


**Tactile servoing**  
e.g., Underwater manipulation

**Force control**  
e.g., Food manipulation

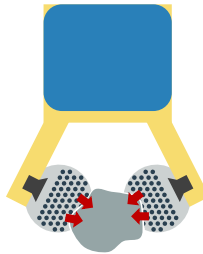
**Pose estimation**  
e.g., Robotic assembly

(a) Ball-shaped gripper



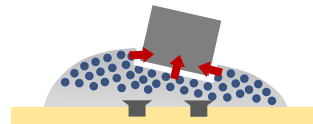
- Palpate the object and environment using the gripper
- Determine the grasped item and perform detection

(b) Fingertip devices



- Grasp fragile objects or heavy objects
- Control grasping stability based on the acquired tactile information

(c) Soft jig device



- Fix object in arbitrary orientation
- Acquire a fixed orientation

Figure 9: Base structure of the proposed robotic skin

### 3.2 Universal gripper

Fig. 10 shows the structure of the proposed universal gripper. The gripper is composed of five parts:

- an elastomer membrane for object grasping
- a granular filling for the jamming transition
- a bulkhead separating the filling and camera
- a camera for optical sensing
- a base part to assemble and mount the gripper

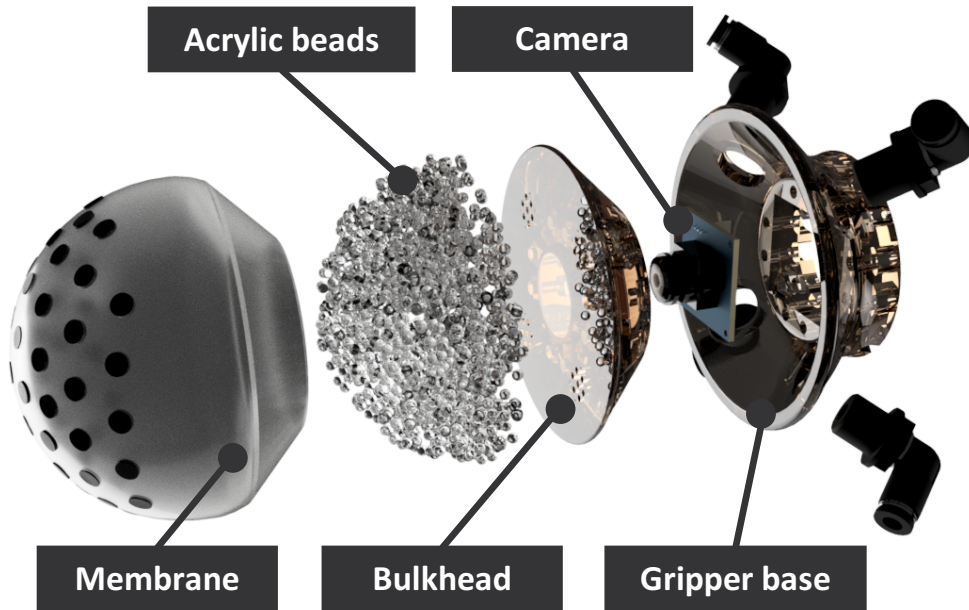


Figure 10: Structure of the proposed universal gripper

### 3.2.1 Design

**Elastomer membrane** As Amend *et al.* [52] notes, the elastomer membrane needs to be both flexible to maximize object conformation and thus grasping force, as well as durable to withstand many grasping operations. For our prototype, we chose a thickness of 1 mm and a hardness of Shore A-20 or less. We embedded circular markers with a diameter of 6 mm and a thickness of 1.5 mm into this membrane to increase the tactile information that the gripper can acquire along with the color information about the object.

**Filling materials** We fill the elastomer membrane with small cubic acrylic beads. Cubic shaped beads can be easily obtained by cutting the acrylic plate. This beads achieve object grasping by jamming transition and optical sensing using transparency.

**Bulkhead** The bulkhead has three functions:

- securing the membrane while preventing fluid leakage
- connecting the pump system to the membrane contents while filtering the granular filling
- providing a view port for the camera

**Camera** We chose a wide-angle camera to increase the visible area of the elastomer membrane. The camera we used had a 180-degree fisheye lens with a resolution of 1920 x 1080 pixels and 30 fps. We used the center area of 600 x 600 pixels (cropped from the undistorted image) for processing, because image undistortion creates some black pixels from distorted image.

### 3.2.2 Fabrication

**Elastomer membrane** Fig. 11(a) illustrates the fabrication process for our elastomer membrane. The mold, shown in Fig. 11(b), was printed using an ABS 3D printer (Fortus 250mc, Stratasys). The surface of the mold was treated with polyester putty (87097, TAMIYA) to make removal of the workpiece easier.

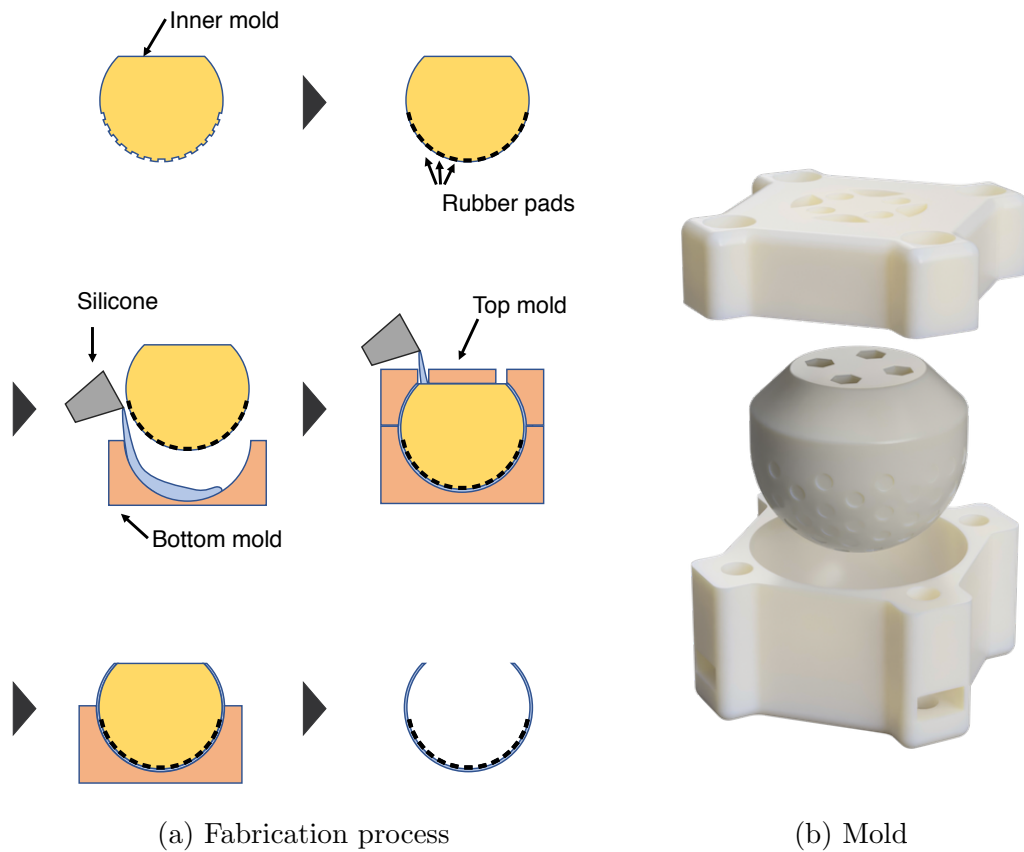


Figure 11: Fabrication description of the membrane

The inner mold has 0.5 mm holes in an icosahedral arrangement, into which the markers (rubber pads, 3M) are pasted. A film of silicone (transparent silicone, Zoukei-Mura) is then poured into the bottom mold, and the inner mold inserted into the bottom mold. The top mold is then fastened to the bottom mold. After the silicone hardens, the top and bottom mold are removed, and the silicone half-dome separated from the inner mold. Finally, the remaining adhesive is removed from the markers.

**Filling materials** The acrylic bodies used as the solid filling were cubes of 3mm side length, cut from an acrylic plate (EX001, ACRYSSUNDAY) using a laser processing machine (VLS6.60, Universal Laser Systems). For the interstitial fluid, we mixed paraffin and silicone oil at a ratio of 27:8, to approximate the



refractive index of the acrylic bodies. Because the refractive indices of the acrylic bodies and the paraffin oil were not known precisely, the mixing ratio was set experimentally.

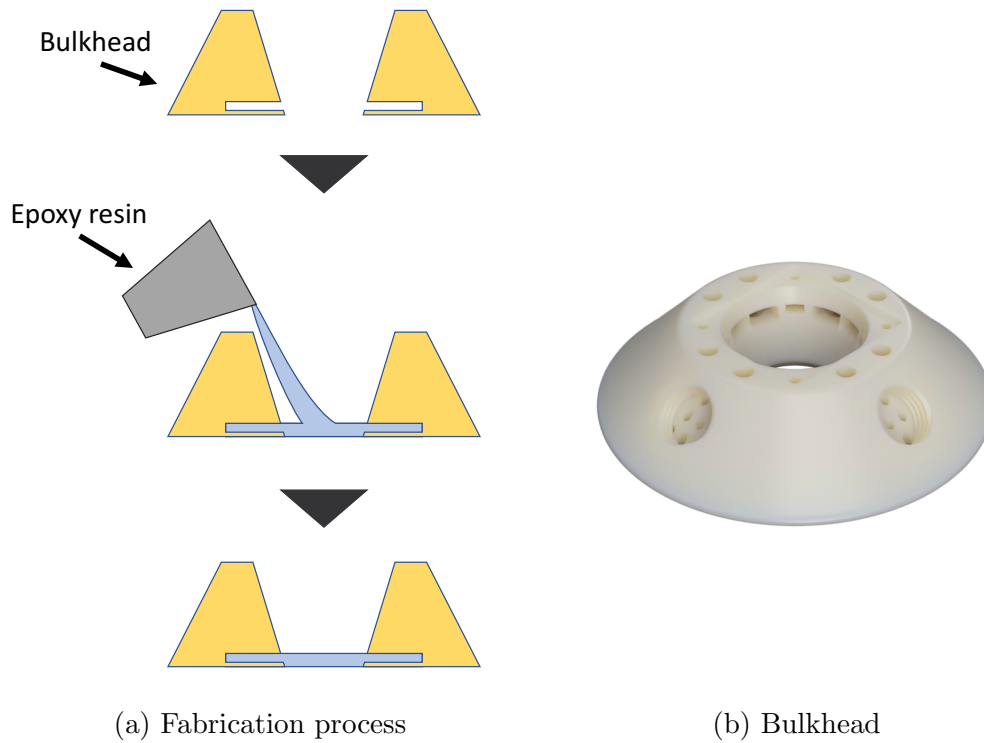


Figure 12: Fabrication description of the bulkhead

**Bulkhead** In order to create a window for the camera which has a watertight seal, the part shown in Fig. 12(b) was 3D printed and the window for the camera formed by pouring transparent epoxy resin (87136, TAMIYA) into the opening, as shown in Fig. 12(a). While this fabrication method ensures a good seal and prevents leakage, the resulting window is slightly warped due to surface tension of the resin and uneven drying. This distorts the camera image, which is evaluated through the experimental results.

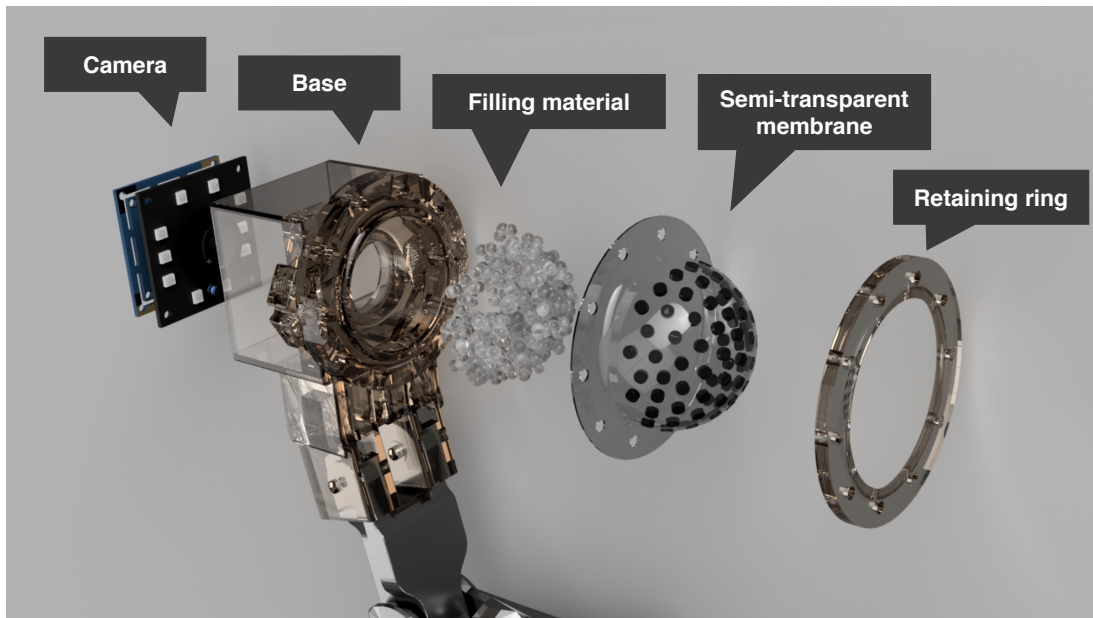


Figure 13: Structure of the proposed fingertip gripper

### 3.3 Fingertip device

#### 3.3.1 Design

Fig. 13 shows the structure of the proposed fingertip device, which is composed of the following five parts:

- a retaining ring to prevent leakage of filling liquid
- a semi-transparent elastomer membrane for object grasping
- a granular filling for the jamming transition
- a base part to assemble and mount the gripper
- a camera for optical sensing

**Semi-transparent membrane** In this device, the elastomer membrane was designed as shown in Fig. 13. The membrane is a hemisphere filled with beads and oil, with a brim to prevent leakage using a retaining ring. The diameter of

the hemispherical portion is 40 mm, the curvature is 28.5 mm, and the thickness of the membrane is 0.5 mm.

In order to perform optical sensing, we also set some markers on the membrane. These markers can improve the sensing spatial resolution using a high number density, improve the object recognition ability with carefully chosen marker positions, and ensure high flexibility by using the same material as the elastomer membrane.

73 markers have been set on the membrane. The diameter of each marker is 3 mm and the height is 1 mm.

**Filling material** We fill the elastomer membrane with spherical acrylic beads with a diameter of about 3 mm. Spherical beads move past each other smoothly, allowing them to fill the membrane as it conforms to the shape of the object. The tactile information can be acquired without optical refraction effects by using a mixture of paraffin oil and silicone oil between the beads to set the solution’s refractive index very close to that of acrylic.

**Base** We create a base part from semi-transparent resin that separates the camera from the liquid while still allowing visible recognition of the elastomer membrane markers. The base is equipped with resin-based filters with 1 mm holes to keep the beads in the membrane. The oil can flow through these filters from inside of the membrane to the oil tubes outside of the device.

The filters are composed of hexagonal honeycomb-like gaps in the semi-transparent resin. The cross-sections of the filters flare out compared to the oil inflow tubes, to compensate for obstruction caused by the honeycomb walls.

**Camera** We choose a wide-angle camera (ELP-USB100W05MT-KRL156, ELP) to capture the entire hemispherical portion of the membrane. This camera has a fisheye lens and an image resolution of  $1280 \times 720$  pixels at 30 fps. This camera can also acquire infrared images using infrared LEDs and filters. In infrared mode instead of RGB mode, the camera can recognize the membrane markers even in a very dark environment.

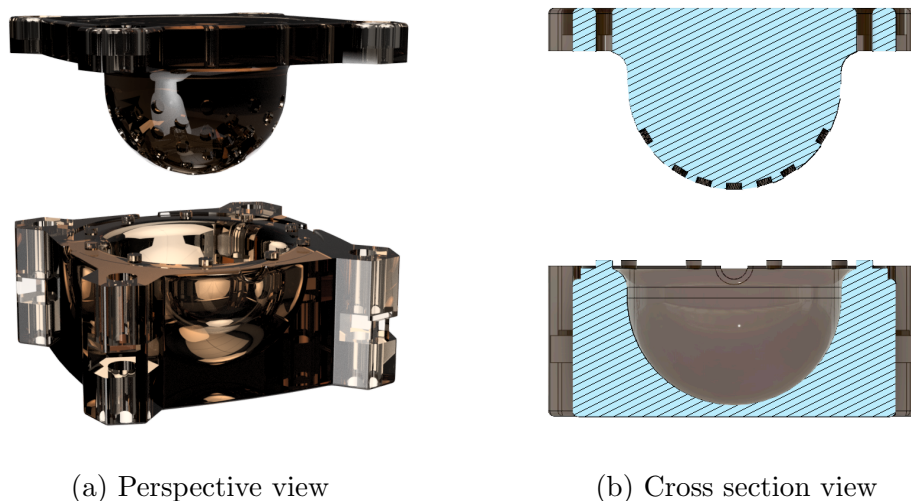


Figure 14: Mold for the membrane

### 3.3.2 Fabrication

**Semi-transparent membrane** The elastomer membrane is fabricated by coating and casting. The mold for our membrane is shown in Fig. 14 and the fabrication process for our membrane is shown in Fig. 15.

First, we color some of the semi-transparent silicone (transparent silicone, Zoukei-Mura) with black pigment (black pigment, EPOCH) for creating markers, and the upper mold is coated with black silicone. After the silicone hardens, the same semi-transparent silicone without black pigment is poured into the bottom mold, then the top mold is inserted. Finally, we remove both the upper and lower molds after the silicone hardens. In order to improve the transparency of the membrane, the molds are also polished beforehand.

**Filling material** Commercial acrylic beads (1/8 inch acrylic beads, Humanity) were chosen as solid filler. A mixture of silicon and paraffin oil was used for fluid filler, as used in Sec. 3.2.2.

**Base** The base part was printed on a 3D printer (AGILISTA-3200, Keyence) that can use semi-transparent resin, and then the camera viewport was polished with #1000-#10000 sandpaper to increase visibility.

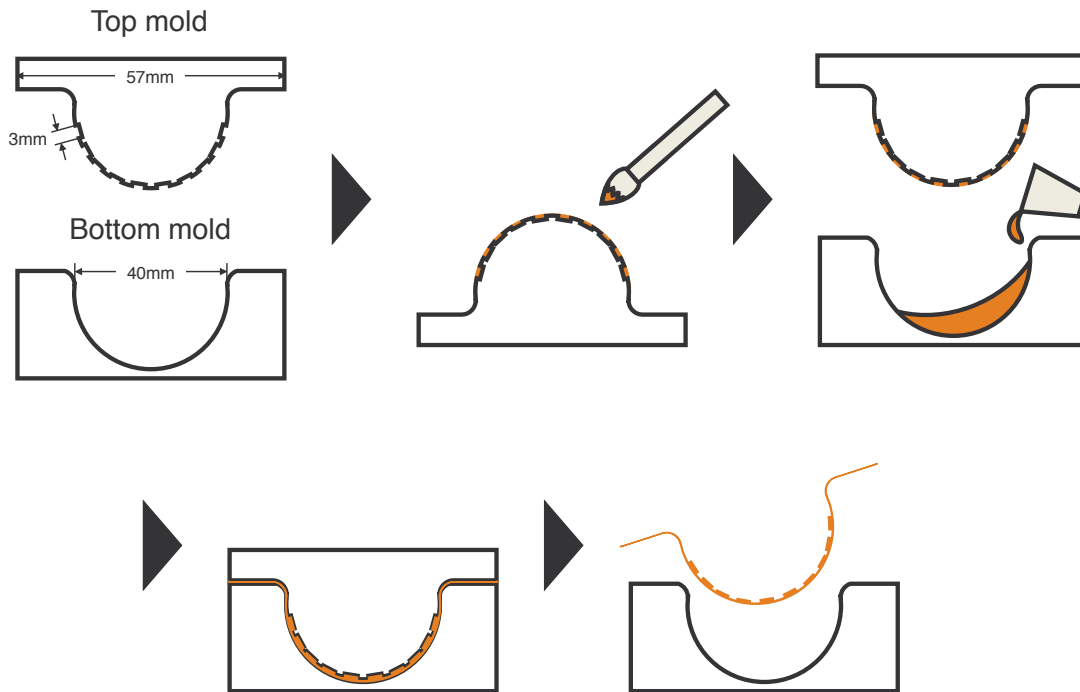


Figure 15: Fabrication of the membrane

### 3.3.3 A strategy for the grasping actions

The advantage of the fingertip device using proposed skin is that can achieve both force-closure and form-closure grasps. Form-closure grasps immobilize an object through geometric configuration of the gripper, independently of force or friction. Conversely, force-closure grasps immobilize an object by balancing forces applied by the gripper, relying on friction and adjustable contact forces. Therefore, while form-closure depends on the grasp's geometry, force-closure necessitates the application and adjustment of contact forces and friction.

Our device can arbitrarily choose between these two forms because it can use the jamming transition to change whether or not the fingertip is hardened along the shape of the object. We designed a strategy for the grasping actions based on the sensing results shown in Fig. 16. It enables robots to perform complex tasks like humans with a simply actuated gripper.

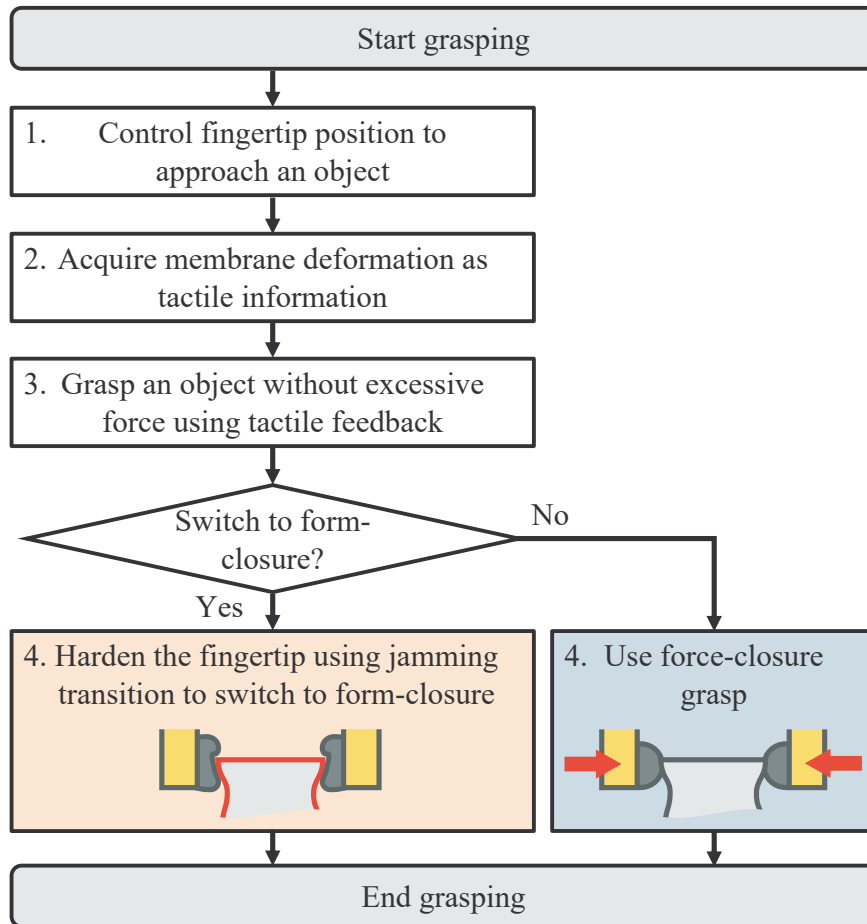


Figure 16: Grasping strategy using fingertip device. See Section 2.3 for Step 2 and Algorithm 1 for Step 3.

---

**Algorithm 1** Grasp an object without excessive force using tactile feedback

---

- 1: Initialize Gripper, Tactile Sensor
  - 2: Max = 100%, Min = 0%, Thr =  $x$
  - 3: SetGripper(Max); Wait
  - 4: **while** Gripper not at Min **do**
  - 5:   **if** ReadTactileSensor() > Thr **then** Break
  - 6:   **end if**
  - 7:   New = Current  $-\Delta$ ; SetGripper(New); Wait
  - 8: **end while**
-

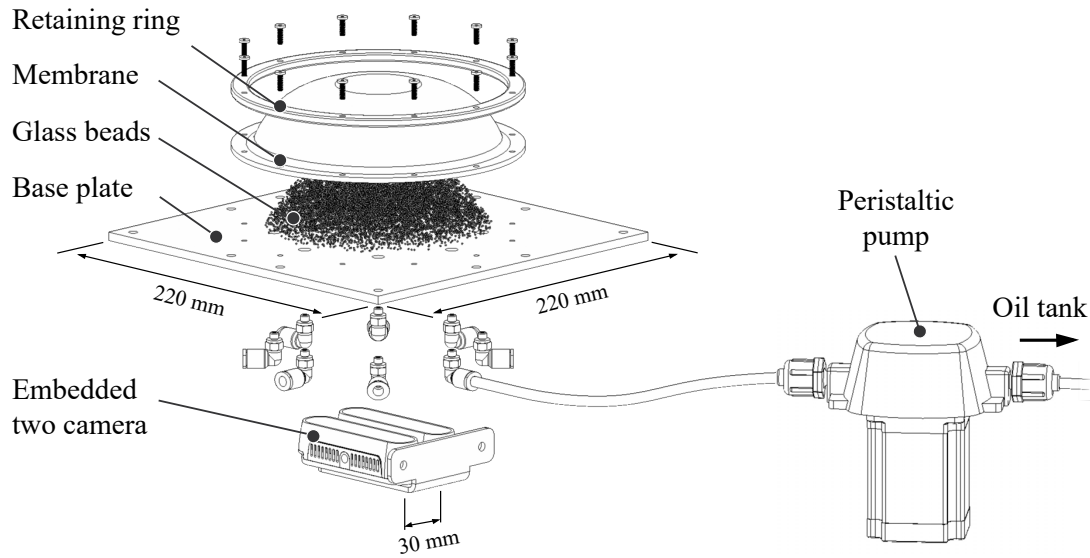


Figure 17: Structure of the soft jig

### 3.4 Soft jig

#### 3.4.1 Design

The soft-jig, shown in Fig. 17 comprises the following five key components:

- A silicone membrane with markers to capture the surface deformation
- Glass beads for jamming transition
- A base plate cut out of transparent polyethylene terephthalate
- A pump to create a jammed state
- Two cameras to acquire the point cloud data around the target object using triangulation

The base plate size was  $220\text{ mm} \times 220\text{ mm} \times 5\text{ mm}$  and the height of the silicone membrane was approximately 30 mm from the base plate. The pancake-like shape increases the robot's ability to reach the object from the top by preventing the object from sinking deeper in a hemispherical shape. As shown in Fig. 18, the soft-jig was filled with oil inside the membrane, and the markers were observed even when the membrane was filled with beads.



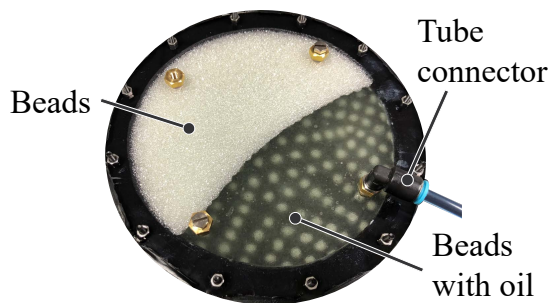


Figure 18: Appearance of the soft jig while being filled with oil, viewed from the camera side. Although the beads are packed tightly inside the membrane, the markers can be observed through the filling oil.

**Silicone Membrane** A silicone membrane with multiple rounded markers was formed using the mold shown in Fig. 19. The membrane thickness was less than 1 mm (approximately 0.7 mm). To form a thin membrane that easily deformed to assume the shape of the object, we employed a method for coating liquid silicone rubber (Dragon Skin FX-Pro, Smooth-On) on a mold surface instead of casting the material with several molds. The mold had hemispherical indentations to create markers, which in turn were filled with white silicone, which was colored with a pigment (Silc Pig, Smooth-On) and mixed with a thickener (THI-VEX, Smooth-On).

After the white silicone hardened, the black silicone adhered to the mold surface after filling the indentations. Instead of using the original color of the silicone, it was colored to allow easy detection of the marker during image processing. The mold was printed using a 3D printer. We removed the layer lines on the mold surface using polyester putty to allow easy removal of the hardened silicone from the 3D-printed plastic mold.

**Glass Beads** If large beads and a thin membrane are used, the shape of the bead will cause bumps on the surface of the membrane; as a result, the contact between the membrane and the object changes from surface contact to point contact, which decreases the coefficient of friction between the object and the membrane [53]. Therefore, beads covered with a silicone membrane should be small in diameter to avoid deteriorating the parts-fixing performance. Further-

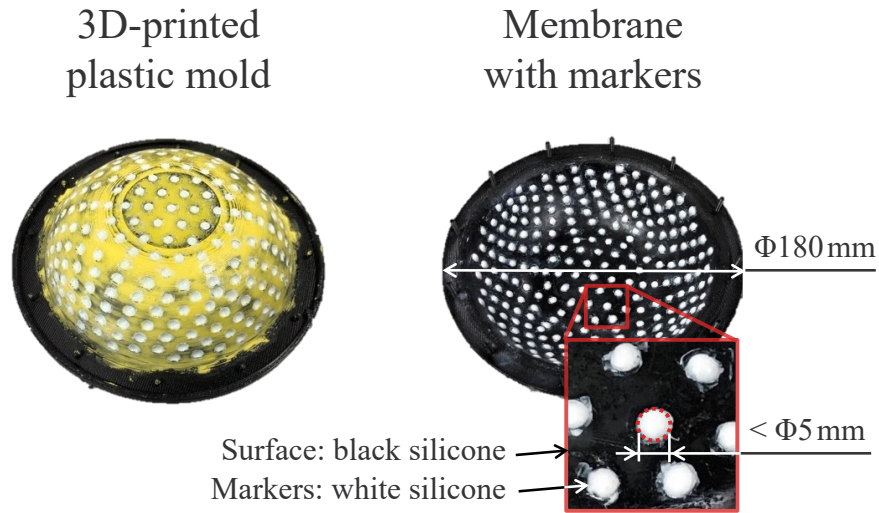


Figure 19: Mold (left) to fabricate the membrane (right) of the soft jig. The curved surface of the membrane can be formed by coating liquid silicone material onto a rigid mold.

more, the beads must be transparent to make the inner markers visible to the cameras. Based on these requirements, we selected 1 mm glass beads (FGB-20, Fuji Manufacturing).

**Base Plate** The base plate must be transparent to make the markers of the membrane visible. It cannot allow leakage of the oil and beads inside and must allow only oil to be pumped through the connected tube.

To achieve this, the plate serves to hold the silicone membrane and tube connectors. Tube connectors with a filter were attached to the underside of the base plate to pump the oil while preventing the beads from flowing out. Because of the small diameter of the beads, the filters must be finer, which reduces the cross-sectional area  $A$  required to enter the tube as well as the mass flow rate  $Q$ ; this is indicated by the equation  $Q = \rho AV$ , where  $\rho$  is the oil density,  $A$  is the cross-sectional area, and  $V$  is the velocity. In a production line, it is necessary to increase  $Q$  to shorten the time. Eight tube connectors were attached to the base plate to distribute the filter load.

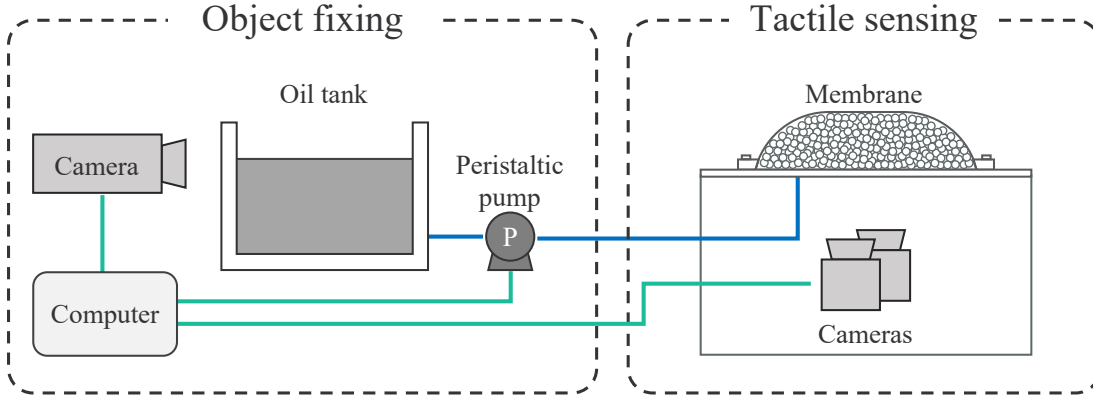


Figure 20: System configuration of the soft jig. The blue and green lines denote the oil flow tubes and electrical connections, respectively.

**Camera** To acquire the deformation of the membrane, we used two cameras embedded inside the jig to capture a pair of images. The two cameras (RealSense D435, Intel) were placed approximately 150 mm under the base plate with a baseline of 30 mm.

Although RealSense D435 can be used to acquire point cloud data based on the active stereo method, the function cannot be used in this hardware configuration of the soft-jig. This is because the infrared light projected from the camera is reflected by the transparent base plate without reaching the inner surface of the membrane.

To eliminate the influence of ambient light, the cameras were surrounded with black plastic plates, and light-emitting diode (LED) lights near the camera maintained a constant brightness during sensing.

### 3.4.2 Fixing and Sensing System

Fig. 20 shows the system configuration of the soft jig. To achieve parts fixing and object-pose estimation, the system comprises three parts: an object-fixing part, a membrane shape-sensing part, and an object pose estimation part.

**Object-Fixing Part** To fix an object in the proposed jig, controlling the input and output of the fluid inside the membrane is necessary. Table 2 shows the difference between pneumatic and hydraulic drives for the jamming transition.

Table 2: Fluid actuation methods for jamming transition.

	Pneumatic-driven	Hydraulic-driven
Fluid type	Compressible fluid	Incompressible fluid
Actuators to drive	Compressor + ejector, vacuum pump + valve, etc.	Peristaltic pump, hydraulic cylinder + linear actuator, etc.
Advantages	Easiness of actuation	Improving the holding force <sup>*1</sup>
Disadvantages	–	Difficulty of actuation <sup>*1</sup>
Remarks	Does not allow optical sensing because of opaque filling	Can be combined with optical sensing because of transparent filling

<sup>\*1</sup> are described in[52]

The advantage of the hydraulic-driven method is that it can be combined with optical sensing. It is challenging to perform optical sensing with the pneumatic-driven approach because no object has the same refractive index as air. However, the hydraulic-driven method requires precise control to prevent excessive input–output that causes cavitation and membrane breakage owing to the incompressibility of oil. Because cavitation inhibits the passage of light, it is prevented by precisely measuring the oil level of the tank and controlling the amount of oil using a peristaltic pump.

To achieve a highly precise oil-level measurement of less than 1 mm, which is unfeasible with commercially available level sensors, such as capacitive, conductive, or float sensors, a camera was used to capture the transparent oil tank from the side with a high resolution. This method allows for greater precision in oil-level control using a peristaltic pump. On the other hand, the method of sensing oil pressure is not suitable for this application, as the pressure value may change regardless of the oil level inside the jig, for example, when it comes into contact with an object. Fig. 21 (a) shows the setup of the oil tank and external camera, and Fig. 21 (b) shows the actual captured image, where the yellow box represents the area for creating a two-dimensional profile. Fig. 21 (c) shows a

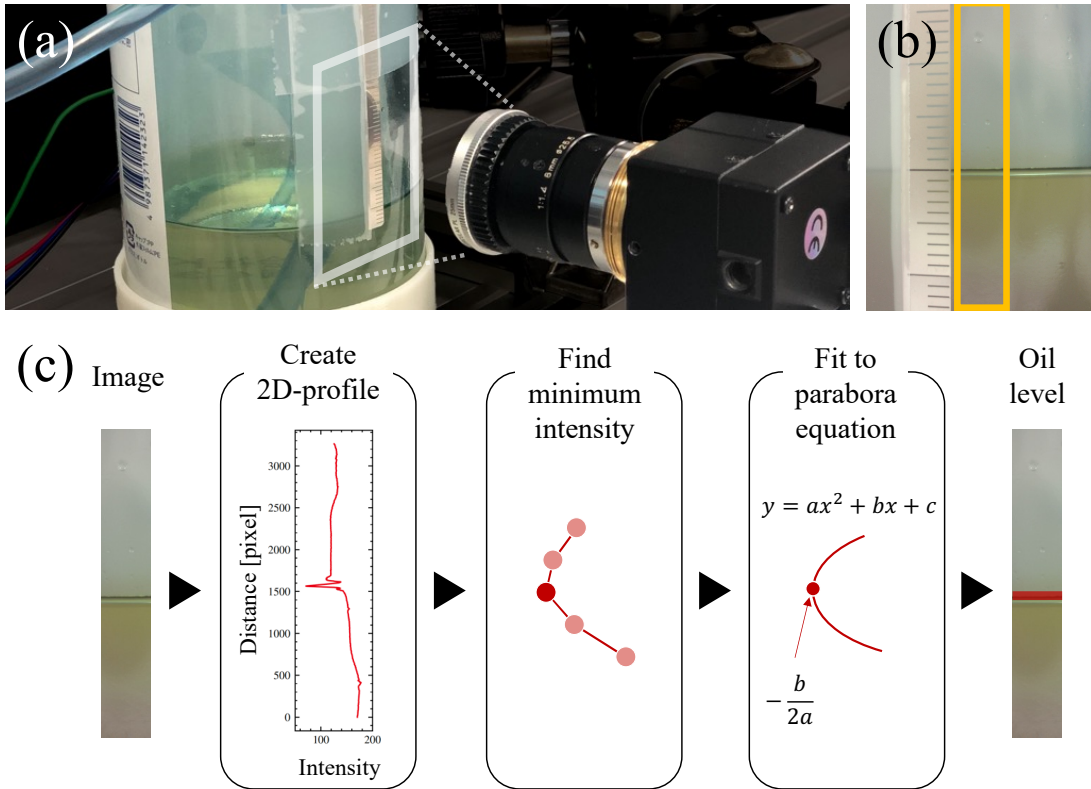


Figure 21: Oil level measurement system. (a) Setup of the oil tank and the external camera. (b) Appearance of the oil level from the external camera side. Oil level per pixel is approximately  $10\ \mu\text{m}$ . (c) Flowchart of the oil level measurement.

flowchart of the oil-level measurement procedure. The oil level per pixel in an image is approximately  $10\ \mu\text{m}$ . The liquid surface is black because the oil rises on the wall surface by capillary action and appears similar to a concave cylindrical lens when viewed from the side.

First, a two-dimensional profile was created by averaging the pixel values in the yellow box in the horizontal direction to analyze the intensity values of the image with respect to the height direction of the tank. Second, the minimum intensity candidate was detected to convert the two-dimensional profile into an oil level measurement, considering that the liquid surface viewed from the side appeared black. To achieve sub-pixel accuracy in the oil level measurement, a parabola function was fitted on measured points around the minimum intensity

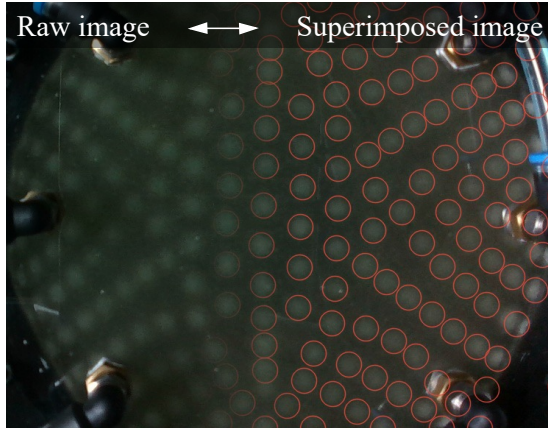


Figure 22: Appearance of markers on the inner surface of the soft jig when viewed from the camera side. The markers were blurred, making it challenging to determine their exact size; nevertheless, their positions could be captured. The red circles superimposed on the image result from marker detection by Laplacian of Gaussian (LoG).

candidate, and the minimum value with the fitted function was determined. This method enabled us to accurately measure the oil level in the tank.

The acquired oil level was used to control the jamming transition by driving the peristaltic pump until the target value was reached. Since the peristaltic pump was driven by a stepping motor, the system could control the amount of oil in response to the pulse input in a closed loop, using the oil level as a feedback parameter.

**Membrane Shape-Sensing** Fig. 22 shows the markers observed in the oil. The markers on the inner surface of the membrane were visible owing to the refractive index-tuned oil, although light travels through several beads to reach the membrane. Because the refractive index was adjusted by the human eye while changing the mixing ratio of paraffin and silicone oils, it did not perfectly match the glass beads and appeared blurred in the camera images.

Fig. 23 shows a flowchart of the proposed membrane shape-sensing that uses acquired images. The system captures a point cloud that represents the membrane shape from the image and treats it as a surface to acquire the membrane

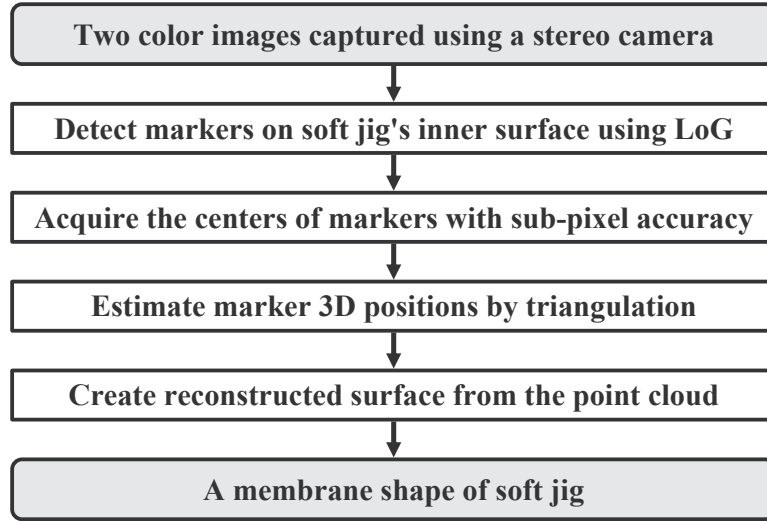


Figure 23: Flowchart of the proposed membrane shape-sensing. The inputs were two paired images, and the output was the pose of the object on the soft jig.

shape as a surface function.

LoG was used to accurately detect marker centers in blurred images. Using the known variation in the marker size in the image,  $\sigma$  of the Gaussian filter was determined, and the center of the markers was calculated by extracting the local maximum from the LoG image.

The centers of the markers detected in the left and right images were acquired in integer pixel units. To acquire the center with sub-pixel accuracy, a least-squares fitting is performed to a quadratic function in the x- and y-directions, respectively, using pixels in the neighborhood of the center. Subsequently, the marker centers were converted to the three-dimensional point cloud based on the triangulation method.

The acquired point cloud is equivalent to the bottom surface of the contacting object. Owing to the soft membrane, the object shape appeared on the membrane as a continuous curved surface smoothed from its original shape owing to the uniform distribution of the fluid. When the object is pressed against the membrane, the membrane enclosing the fluid maintains its surface as a smooth curve. Because a point cloud is a continuous curved surface, it can be defined as a differentiable surface function using the radial basis function. This allows

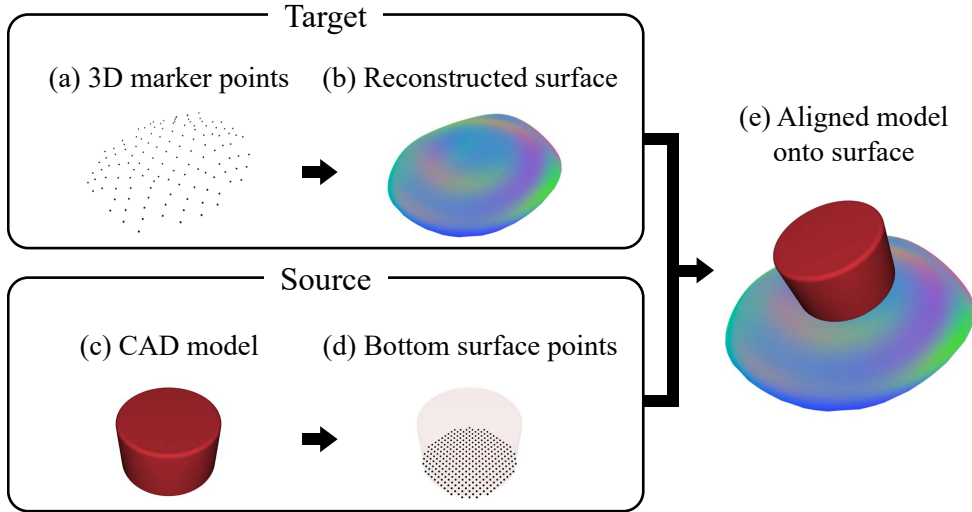


Figure 24: Point-to-function ICP that finds a transformation from the reconstructed membrane surface to the bottom surface of the object model.

interpolation of the surface heights and normals at any  $xy$ -position.

**Object Pose Estimation** Fig. 24 shows the point-to-function ICP, the proposed algorithm for estimating the orientation of a pushed object. Fig. 25 shows a point cloud of the bottom surface generated using the CAD model as the source for the pose estimation. The coordinate system of the CAD model is adjusted to the fixing pose, and the intersection points with the  $z$ -up vector are calculated by shifting the  $xy$ -position of the  $z$ -up vector at regular pitch intervals. The lowest value in the intersection area is treated as the bottom surface point.

The pose of the object is estimated by performing ICP using a CAD point cloud and a differentiable surface function. In point-to-plane ICP, the source and target point clouds are static, and the pair points of the source and target point clouds must match. Conversely, point-to-function ICP and the  $xy$ -position of all points in the source point cloud from CAD were used as inputs for the surface function, and the target point cloud (surface) was calculated from the function for each iteration. Because the function is differentiable, we calculated the target  $xyz$  points and the normals from the derivative at each surface position. This makes it straightforward to calculate the point correspondence between the source and



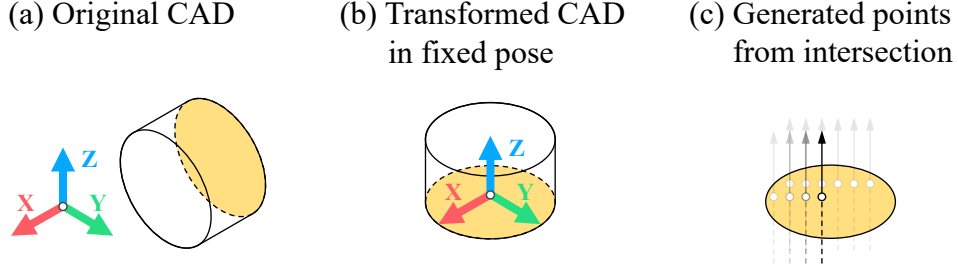


Figure 25: Pre-processing to convert a computer-aided design (CAD) model into points. (a) Original CAD model. The yellow surface is the bottom when fixed. (b) Transformed CAD model in the fixed pose coordinate system. (c) Generated points from the intersection of the z-up vector and the bottom surface.

target, even when the spatial resolutions of the source and target point clouds differ.

Here, the rotation around the z-axis in the objective function  $\varepsilon$  for ICP can be fixed if the object is rotationally symmetric (e.g., bearing). The objective function used in the point-to-plane and point-to-function metric is expressed as

$$\varepsilon = \sum_{i=1}^{N_p} [(\mathbf{R}\mathbf{p}_i + \mathbf{t} - \mathbf{q}_i) \cdot \mathbf{n}_i]^2 \quad (4)$$

where

$$\mathbf{R} = \begin{cases} \mathbf{R}_x \mathbf{R}_y & \text{if rotationally symmetric} \\ \mathbf{R}_x \mathbf{R}_y \mathbf{R}_z & \text{otherwise} \end{cases}$$

$\mathbf{R}_x, \mathbf{R}_y, \mathbf{R}_z$  are the rotation matrices around the x-, y-, and z-axes in the fixed coordinate system, respectively.  $\mathbf{R}$  is the combined rotation matrix,  $\mathbf{t}$  is the translation vector,  $\mathbf{p}_i$  (source), and  $\mathbf{q}_i$  (target) are the pairs of corresponding points,  $\mathbf{n}_i$  is the normal vector of the target, and  $N_p$  is the number of corresponding points found in the ICP. Here, we utilize a 5-DoF metric when  $\mathbf{R}$  is  $\mathbf{R}_x \mathbf{R}_y$  and a 6-DoF metric when  $\mathbf{R}$  is  $\mathbf{R}_x \mathbf{R}_y \mathbf{R}_z$ .

We minimized this  $\varepsilon$  using the Levenberg–Marquard algorithm[54] to search for pose parameters ( $\mathbf{R}$  and  $\mathbf{t}$ ) and treated the result as the pose of the object.

## 4. Sensing and grasping evaluation with developed robotic devices

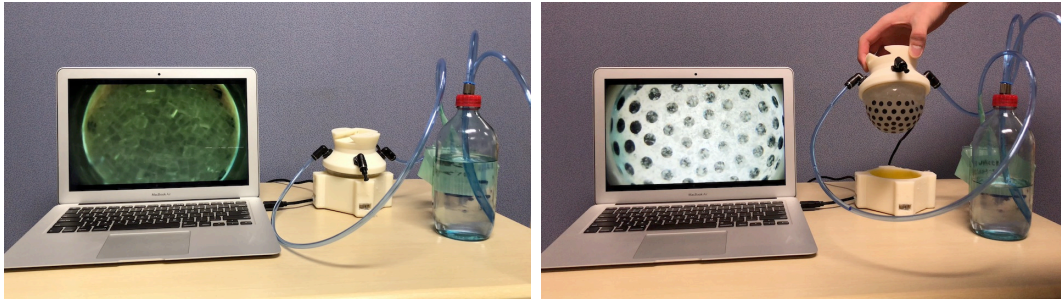
### 4.1 Evaluate universal gripper

We conducted three experiments, first testing the ability for tactile sensing with our gripper, then testing object grasping, and finally attempting to perform simultaneous grasping and sensing.

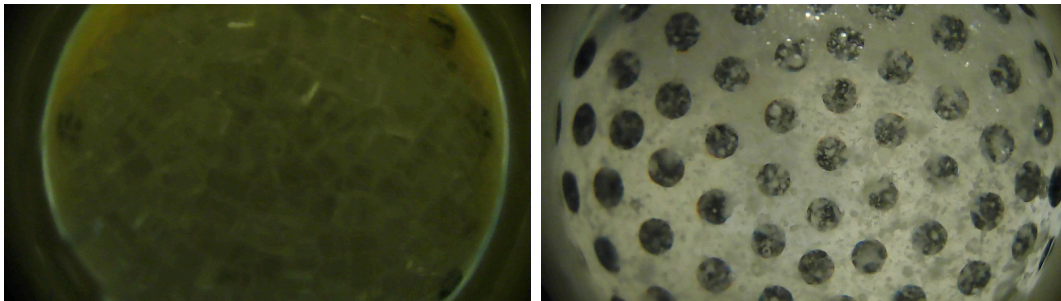
Before the experiment, we filled the gripper with the materials to evaluate the transparency of the granular filling mixed with the interstitial fluid,. Fig. 26 shows the prepared gripper mixed with/without the interstitial fluid. Immediately after filling the materials, the bubbles occluded the markers, but markers were recognized. To run the gripper hydraulically, a bottle was prepared as an air-hydro converter. In our experimental setup, a compressor (SRL-0.75DS6, HITACHI) generated dry compressed air at a pressure of 0.8 MPa which was converted to air with a negative pressure of -90 kPa air using an ejector (ZH10DSA-06-06-08S, SMC). This was then used to drive the hydraulic gripper.

#### 4.1.1 Tactile sensing

In this experiment, we used the gripper to touch cylinders of different heights arranged as shown in Fig. 27 while measuring the deformation of the center of the membrane. Fig. 28 shows how the measured deformation increases with the height of the palpated cylinder. We found that we could measure the relative deformation well, even though the absolute values are not completely correct. We believe that this may be due to distortion as the marker approaches the camera, when the assumptions of the weak perspective projection become less accurate. The distortion introduced by the resin window and the filling also affects the results.



(a) Appearance of the gripper before filling (b) Appearance of the gripper after filling



(c) Camera view of the gripper before filling (d) Camera view of the gripper after filling

Figure 26: Transparency of the granular filling mixed with/without the interstitial fluid. The occlusions are due to bubbles and surface imperfections in the filled gripper.

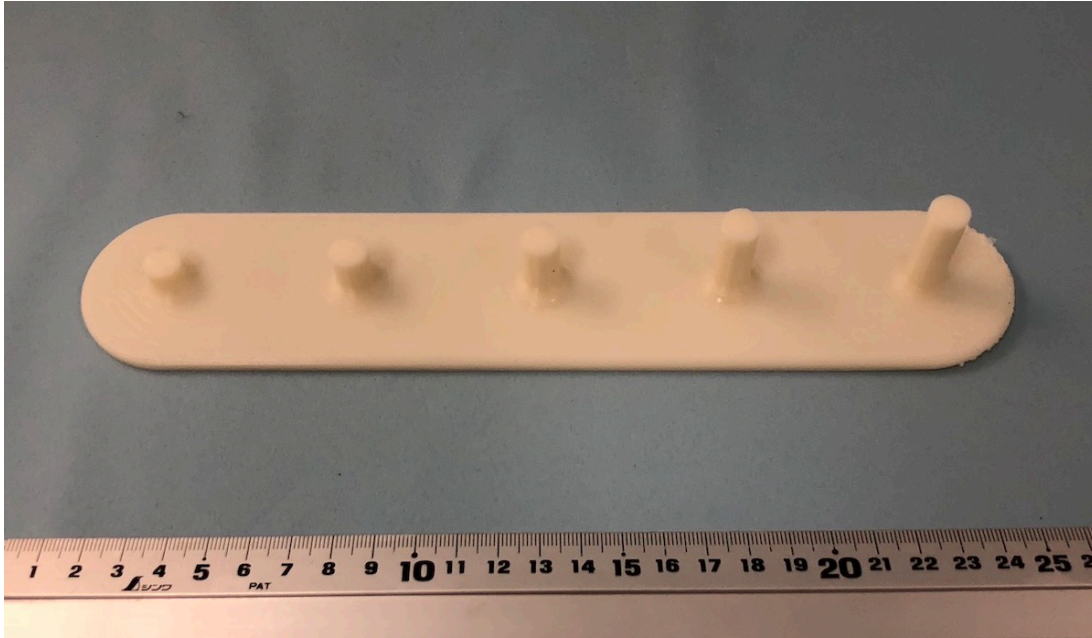


Figure 27: Pins of different heights. It was printed using a 3D printer. These heights increase by 5 mm from 10 mm to 30 mm.

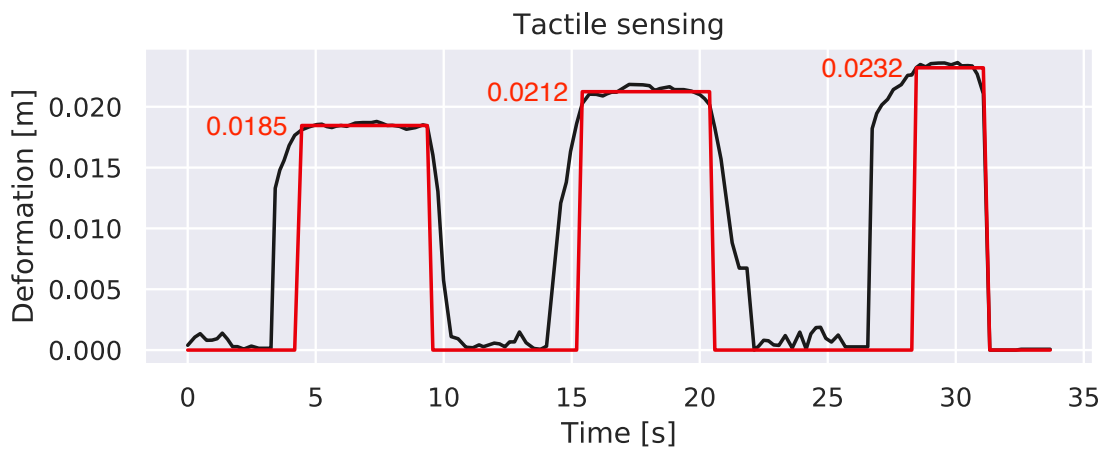


Figure 28: Membrane deformation while palpating pins that differ in height by 5 mm. The black line represents the calculated raw value and the red line represents the mean value of each of the plateaus.

Table 3: Performance when grasping long cylinders

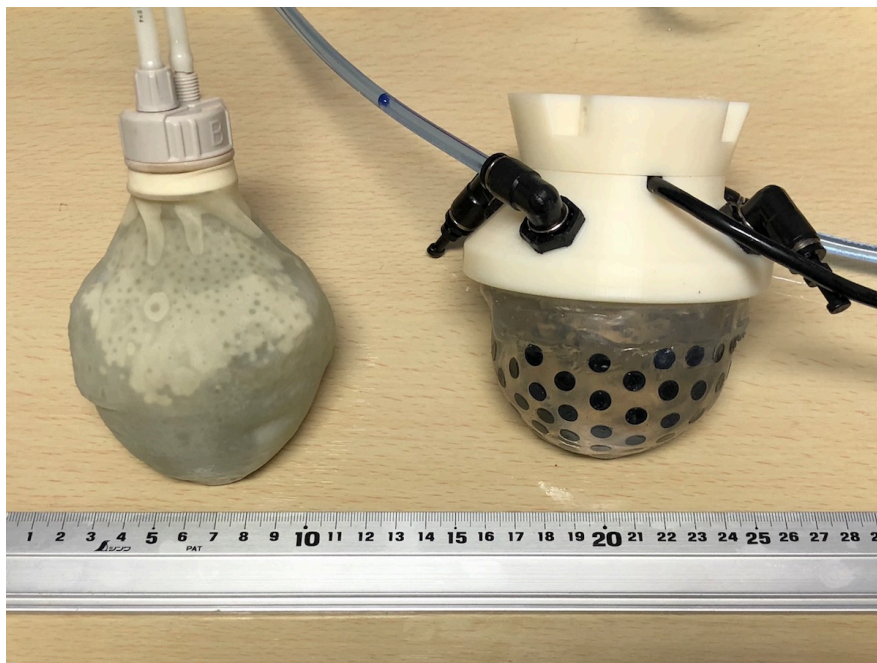
Diameter [mm]	∅10	∅15	∅20	∅30	∅40
Proposed gripper	✓	✓	✗	✗	✗
Prototype gripper using a balloon	✓	✓	✓	✗	✗

#### 4.1.2 Object grasping

In the grasping experiment, we evaluated the performance of our gripper by grasping cylinders of different diameter shown in Fig. 29(a), and compared this performance with a hydraulic universal gripper we manufactured using a balloon shown in Fig. 29(b). This prototype gripper using a balloon has a thin and flexible membrane because it uses a balloon as well as the universal gripper proposed by Amend *et al.* [3]. As shown in Table 3, the more conventional design could grasp slightly bigger objects, but we believe that this difference can be alleviated by improving the manufacturing and design of the prototype.



(a) Cylinders between 10 and 40 mm diameter



(b) Grippers with different membrane flexibility

Figure 29: Equipment used in the grasping experiment

### 4.1.3 Simultaneous grasping and sensing

Finally, we attempted to use our gripper to grasp objects of different sizes as shown in Fig. 30. Fig. 31 shows an example of an object grasped with the gripper along with the shape change visualization.

In this experiment, we were able to grasp all objects successfully and to visualize the gripper shape during the grasping process.



Figure 30: Cylindrical and rectangular objects between 10 to 70 mm length

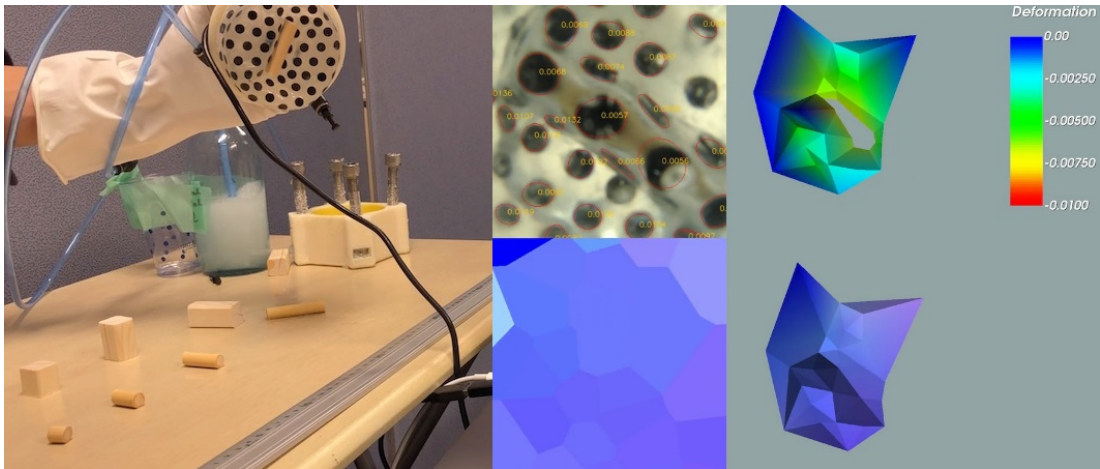
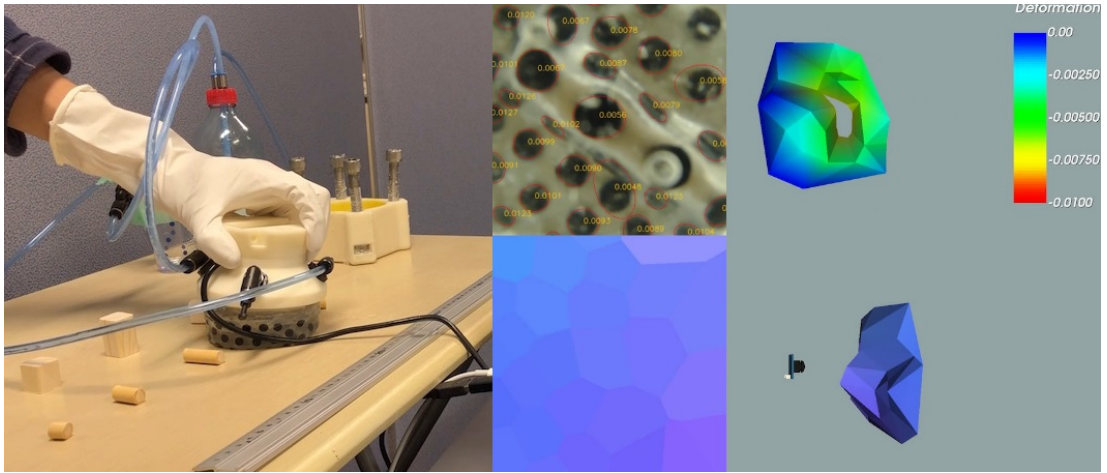


Figure 31: A scene from the grasping experiments shown with the live viewer display



#### 4.1.4 Discussion

Our prototype gripper suffers from some limitations due to the manufacturing process. Notably, its grasping force is not yet as high as our hydraulic prototype using a balloon, probably likely due to the rigid markers and the silicone material used for the elastomer membrane in the prototype.

Improved manufacturing should allow:

- smaller markers on the membrane, allowing improved resolution of the deformation
- improved transparency of the filling, by reducing visible imperfections and cuts on the acrylic bodies
- higher grasping forces due to improved material properties of the membrane

Other issues that could be solved are deteriorated recognition due to bubbles entering the filling of the gripper, which occurred during the grasping experiment, and occasional leakage.

As mentioned in Section 3.2.2, the camera viewport was slightly warped due to its manufacture from poured epoxy resin. This introduced additional distortion in the camera image, and thus errors in the resolution of the markers. We used this method to ensure a watertight seal, but using a glass or acrylic plate for the camera opening should improve its visual properties. Improving this design is part of our future work, as well as compensating for refraction caused by the plate in front of the camera.

## 4.2 Evaluate fingertip device

Several experiments have been conducted to evaluate the performance of the proposed device. The experimental setup is shown in Fig. 34.

We conducted experiments using the manipulator to confirm grasping status with the following procedure.

1. place an object directly under the gripper
2. close the gripper to touch the object and acquire contact information
3. catch the object and stop closing the gripper
4. lift the gripper up using the manipulator and confirm the success or failure of the grasp

### 4.2.1 Tactile sensing

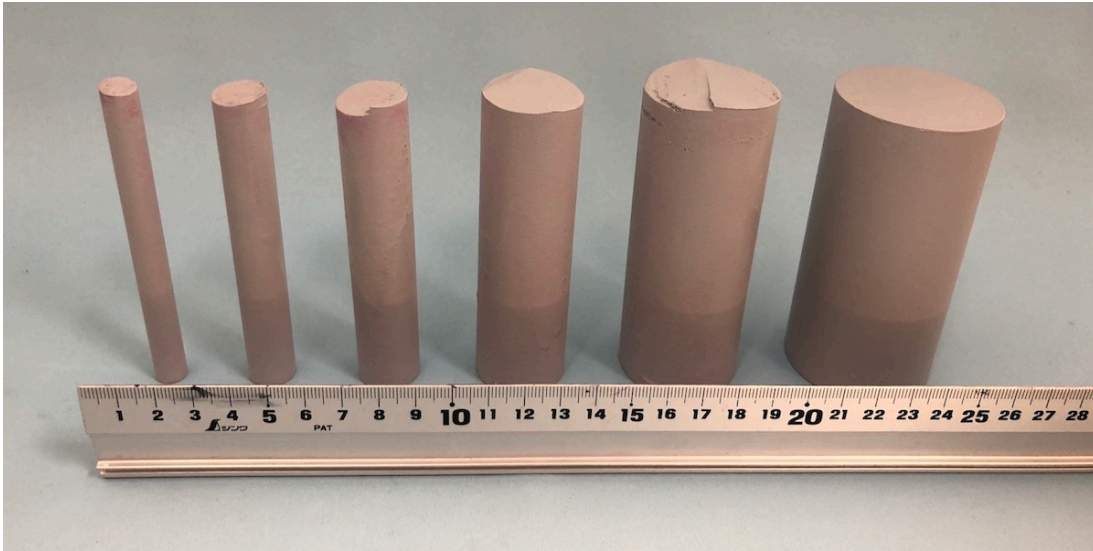
We evaluated the tactile information by grasping cylinders of length 100 mm with diameters ranging from 10 to 50 mm as shown in Fig. 32(a).

Fig. 32(b) shows an example visualization of tactile information, and Fig. 33 shows an example of tactile information during the grasping operation. Because the initial opening angles of the gripper are all equal, we confirmed that the larger cylinders can be grasped more quickly as the gripper has less distance to travel by using the tactile information.

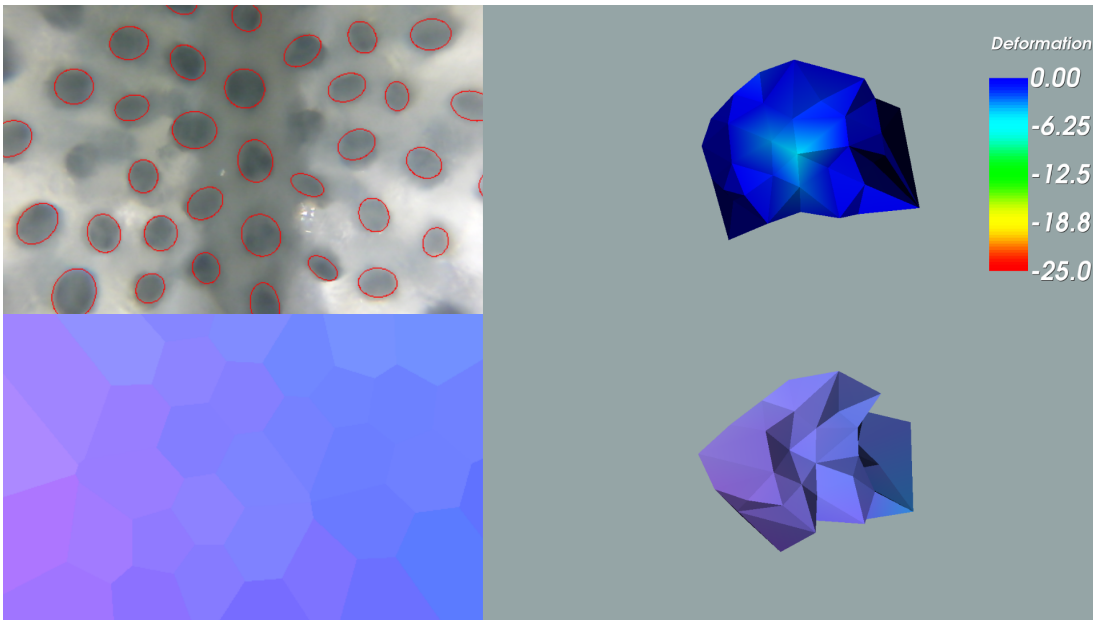
Noise can be seen in Fig. 33, but we can see that the data still captures membrane deformation.

Unfortunately, the 50 mm diameter cylinder slipped down under its own weight.

Soft membranes give a large contact area, but because they are easily deformed, heavy object grasping becomes unstable while keeping it soft. This problem can be solved by increasing the membrane stiffness using the jamming transition.



(a) Cylinders between 10 and 50 mm diameter. All cylinders have the same length of 100 mm.



(b) Visualization of tactile information during object grasping. The upper left shows the image captured by the camera, the lower left shows the estimated normal map, and the right shows the three-dimensional shape of the membrane.

Figure 32: Tactile sensing with cylinders

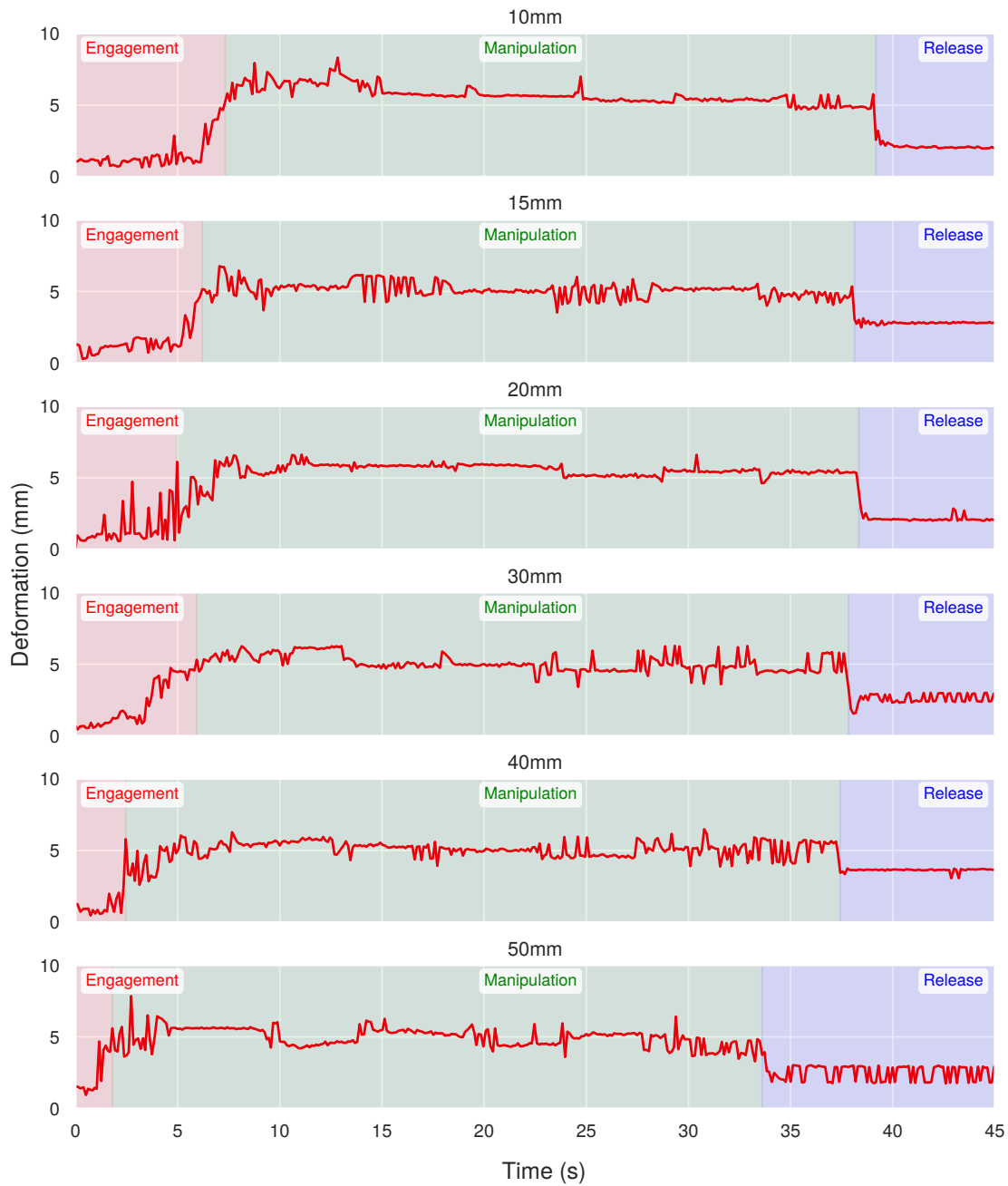


Figure 33: Deformation depth of the membrane with cylinders. The red area indicates that the gripper is closing, the green area indicates that the gripper is closed and grasped, and the blue area indicates that the object is released.

### 4.2.2 Fragile object grasping

To verify the feasibility of the sensing method, we conducted object-grasping experiments using membranes filled with beads and oil on fragile objects with the closed loop system. In this experiment, the system closes the gripper, stopping when the membrane deformation reaches 5 mm so as not to apply excessive force. Fig. 35 shows two examples of foods being grasped gently. With this device, even fragile objects can be grasped without being damaged thanks to the optical tactile feedback. For the tofu, although it could be grasped without breaking, there was a case where it slipped and fell because the surface was very wet.

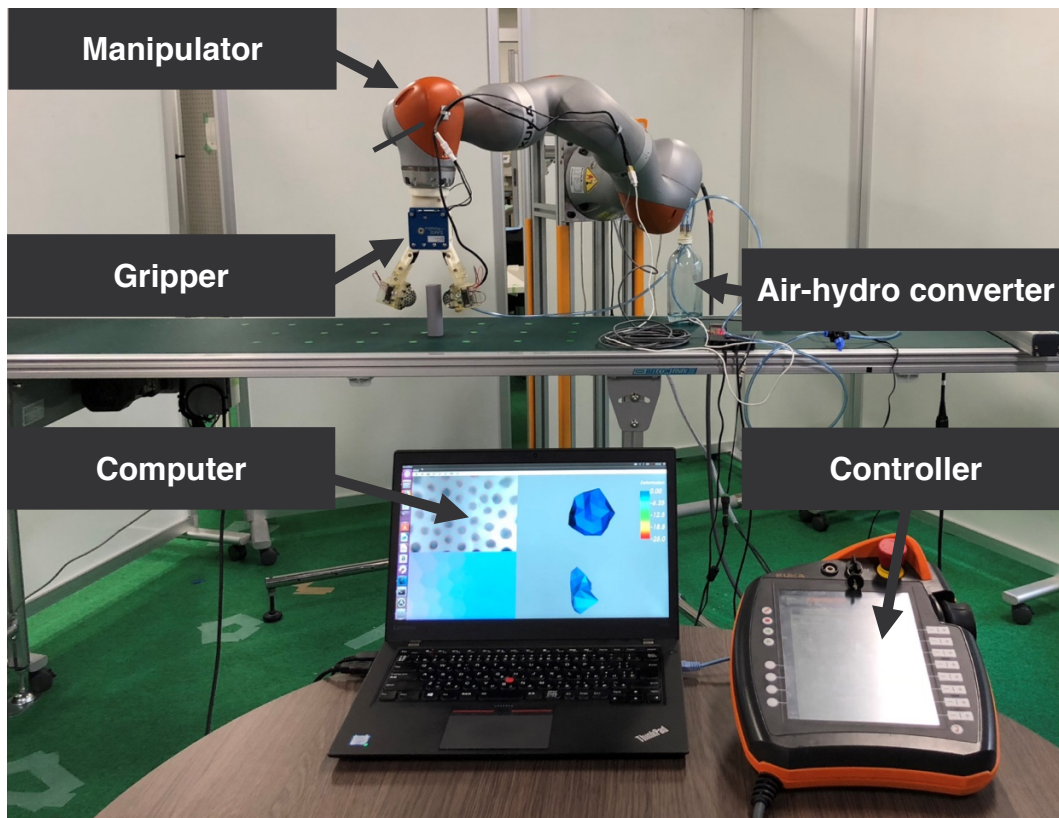
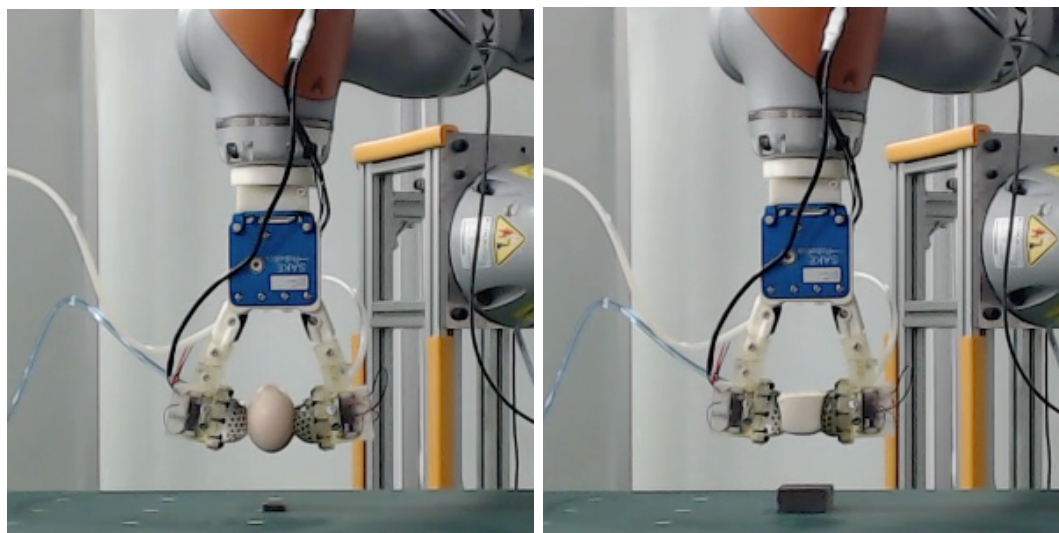


Figure 34: Experimental setup for fragile object grasping



(a) Egg

(b) Tofu

Figure 35: Grasping experiment with closed loop system

Table 4: Performance when grasping dumbbells

Weight of dumbbells	1 kg	2 kg	3 kg	5 kg
Without jamming transition	✓	✓	✗	✗
With jamming transition	✓	✓	✓	✗

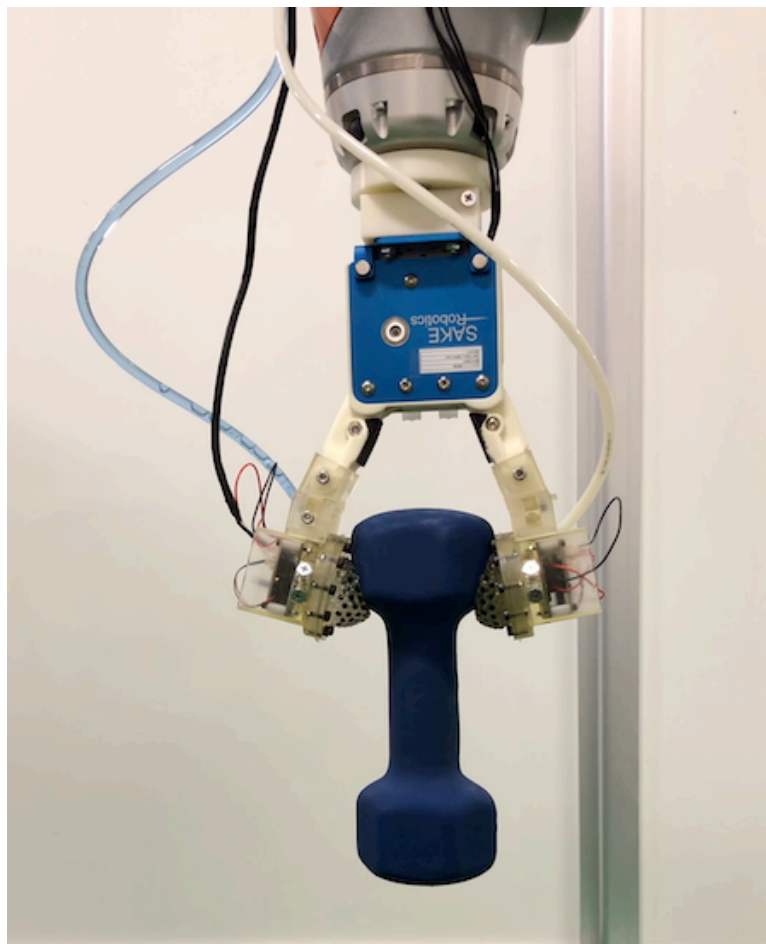
### 4.2.3 Heavy object grasping using jamming transition

We used heavy loads to verify the grasping performance improvement using the jamming transition. In these experiments, we used an air-hydro converter with an air compressor (CP-12Si, Minato Electric Works) and an ejector (ZH10DSA-06-06-08S, SMC) to change the internal pressure in the device. The internal pressure was controlled manually after confirming that the object was grasped.

Fig. 36(a) shows the dumbbells used, Fig. 36(b) shows an example of grasping, and Table 4 shows the result of the grasping experiments. During the grasp, the jamming transition was used to suppress membrane deformation due to dumbbell weight, and we confirmed that even though the fingertip device had a flexible contact part, the holding performance on the heavy object could be improved.



(a) Dumbbells between 1 to 5 kg weight



(b) Grasping 3 kg dumbbell

Figure 36: Heavy grasping experiment using jamming transition



Table 5: Performance when pouring beads without slipping the cup

Weight of beads [g]	0	50	100	150	200	250	300
Force-closure grasps	✓	✓	✓	✗	✗	✗	✗
Form-closure grasps	✓	✓	✓	✓	✓	✓	✗

#### 4.2.4 Stable grasping for manipulation

We present a demonstration of pouring motion using a deformable cup filled with beads to show the potential of combination of both tactile sensing and more-constrained grasping. If a robot just grasps a deformable cup, force-closure grasp using the tactile information is efficient. However, when the robot pours the contents of the cup, an advanced grasping strategy is required to prevent slippage without damaging the cup. We verify the achievement of both force-closure and form-closure grasp by the jamming transition and tactile sensing.

In this demonstration, a plastic cup measured by tactile sensing is manipulated with two different closure types (*i.e.* force-closure and form-closure) that switch using jamming transition. We compare two closure types using a pouring motion. Fig. 37 shows the snapshots of the pouring motion. The tactile sensing was performed only the first time in order to prevent changes in grasping force due to measurement errors, and the fingers are controlled to the same angle in subsequent trials. Glass beads are poured into the cup in advance by 50 g each time until pouring motion fails. Also, to efficiently incorporate the jamming transition into the demonstration, a peristaltic pump (KHL-SZS35, Kamoer) is used to control the internal fluid, both input and output using the sensing results. Fig. 38 shows the electrical and piping system connected to the pump. A PWM signal is transmitted from a Raspberry Pi to a motor driver based on the driving time sent from another PC connected via Ethernet.

Table 5 and Fig. 39 show the results of the experiments. The grasping states when manipulating a cup filled with 150 g of beads are shown in Fig. 40. As a result of the experiment, it was impossible to maintain the grasp from 150 g in the force-closure grasp, and slipping occurred from the 300 g in the form-closure grasp.

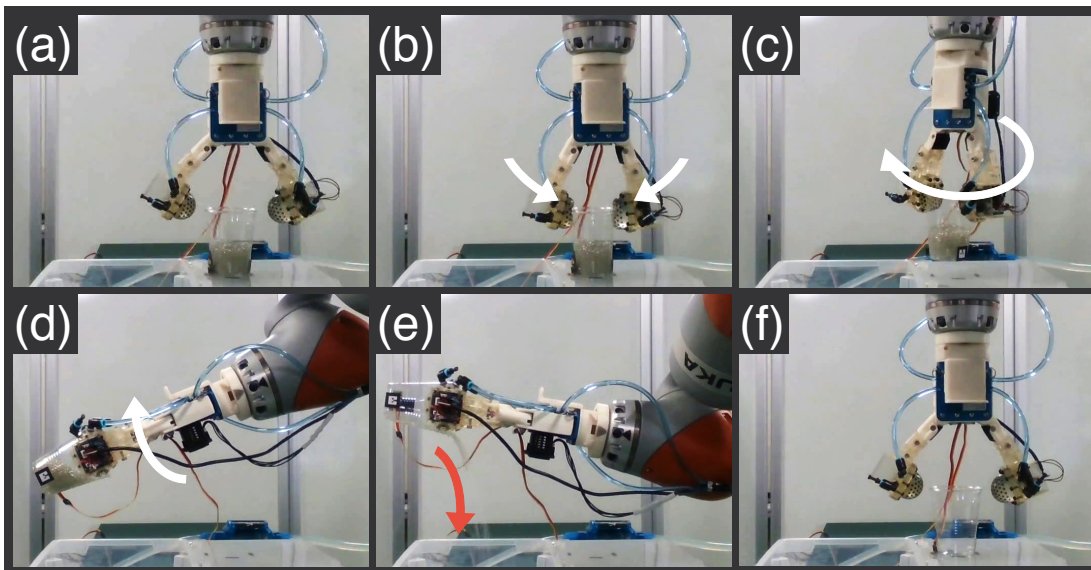


Figure 37: Snapshots of the pouring motion. (a) A cup filled with beads is placed under the gripper. (b) Fingertips of a parallel gripper are fitted to the cup. The fingertips can be hardened as necessary. (c) Gripper is rotated to pour. (d) Gripper is tilted until it reaches  $100^\circ$ . (e) Beads are poured into the container. (f) The poured cup is released at the initial position.

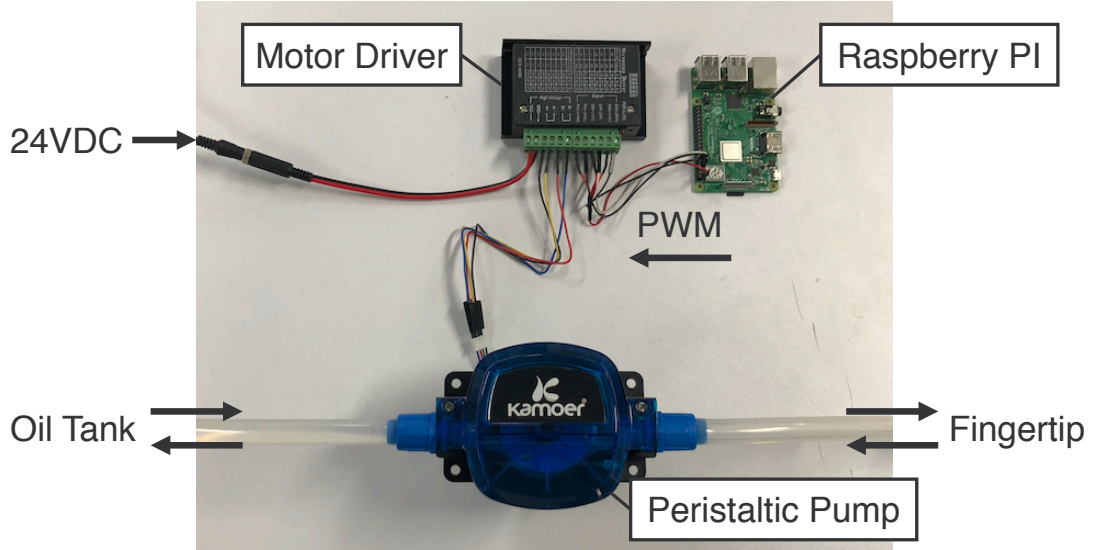


Figure 38: Electrical and piping system connected to the pump

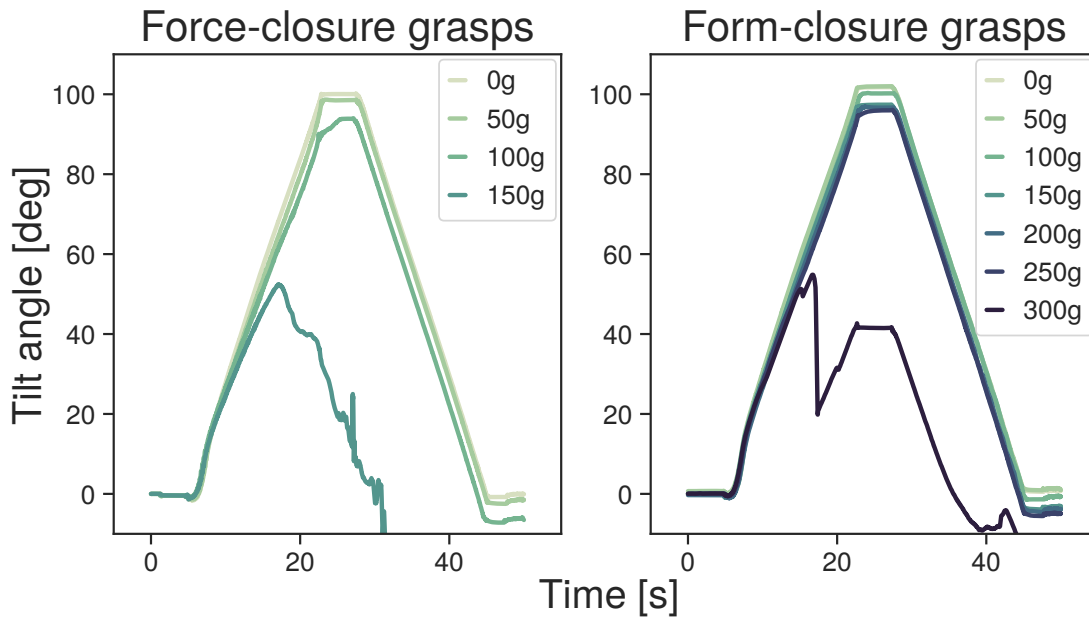


Figure 39: Tilt angle of the cup at each trial measured by the IMU sensor attached to the side of the cup

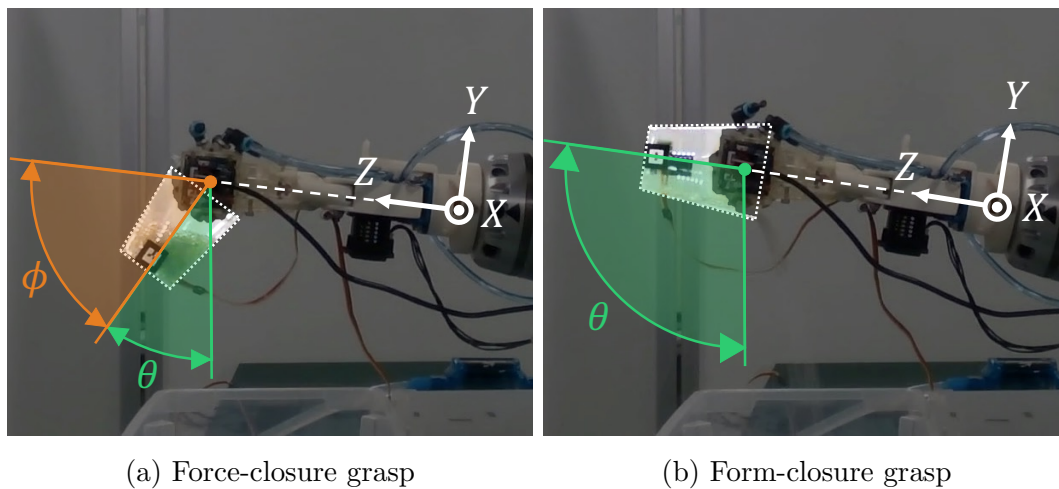


Figure 40: The grasping states when manipulating a cup filled with 150 g of beads. In the left figure, we can not maintain the pose of the cup by applying force, but in the right figure it is maintained by the shape of the hardened membrane. Where  $\theta$  is the tilt angle of the cup, and  $\phi$  is the angle error between the gripper and the cup caused by the slippage.

### 4.2.5 Discussion

As the results show, the prototype can obtain necessary tactile information to grasp objects without applying excessive force.

In Section 4.2.4, we improved the stability of the grasping using jamming transition, which is activated by draining the oil inside the membrane. By fixing the shape of the membrane, the grasp becomes stable in the sense of form-closure. Since unlike the force-closure, the form-closure does not rely on the friction force to grasp, the normal forces are easily reduced. Note that the membrane may shrink due to draining, it is better to adjust the closing angle of the gripper.

The accuracy of the tactile information can be improved by increasing the accuracy of the estimation of the membrane deformation. For example, the three-dimensional position errors due to camera calibration and due to refraction as the light proceeds from the filling material through the semi-transparent base and into the air layer in front of the camera can both be resolved by measuring the distance and the pixel size of the object beforehand. The deformation of the membrane is nonlinearly related to the applied force and the pressure of the oil inside. By calibrating these relationships, we believe that the force estimation can be achieved using machine learning techniques.

One issue with the current design includes small oil leaks as well as bubbles that affect optical information acquisition. These problems will be solved by improving the hydraulic design. Another issue is the beads underneath the membrane form bumps on the membrane surface when the oil pressure in the device is lowered for the jamming transition. Unevenness on the membrane surface is expected to prevent slippage of objects with a rough surface. On the other hand, if it is judged that the object is a primitive shape having a flat surface using the estimated object shape, force-closure grasp should be used to prevent an increase in slip due to a decrease in contact area.

## 5. Gentle grasping with a manipulator and a parallel gripper

### 5.1 Introduction

In this section, we propose automatic object recognition and gentle grasping method to show how to use the proposed parallel gripper on unknown objects with the tactile sensing as an example of application. We also evaluate the performance of the proposed parallel gripper by experiment.

Although parallel grippers are widely used in factories, they can only restrain the target object from two directions, which allows slippage in the remaining directions. To prevent this, we normally restrain it by applying a large force to the object. However, when fragile object contained in the target objects, this will not be the proper solution.

We propose a better solution that constraining objects with a flexible membrane. We aim to handle objects gently by combining flexible membrane and tactile information.

### 5.2 Experiment setup

To run multiple grasp experiments, we use grasping system shown in Fig. 41.

To acquire tactile information, we use a laptop computer connected to the gripper via the USB interface. The motion planning is performed by another laptop to increase the sampling rate of tactile information. The point cloud processing is performed in order to automatically detect the object to be grasped. This processing pipeline is run on single board computer (Jetson TX2, NVIDIA) and used a depth camera (RealSense Depth Camera D415, Intel). Also, the motion capture (OptiTrack Flex3, NaturalPoint) is used to match the coordinate system of the manipulator with the depth camera. Fig. 43 shows the retro-reflective markers attached to the depth camera to recognize by the motion capture.

Fig. 42 shows the experimental environment. The green bounding box indicates the detection area of the object, the axis inside the bounding box indicates the detected object coordinate, and the axis outside the bounding box indicates the storage box coordinate in which the grasped object is stored.

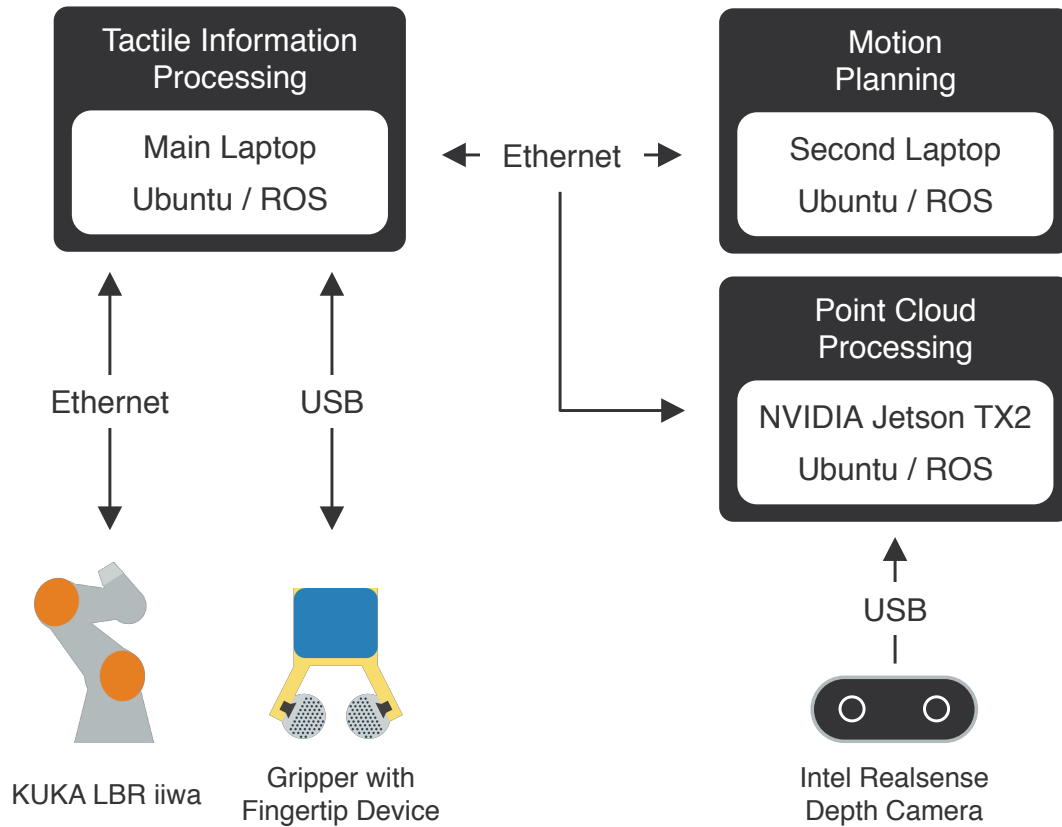


Figure 41: The grasping system configuration to communicate between tactile information processing with main computer and another processing nodes

### 5.3 Object recognition

The object pose is estimated by point cloud processing in order to recognize various objects without depending on shape and texture.

First, a point cloud acquired by the camera is filtered. Since the camera coordinate is known, only parts of the point cloud on the table is cropped. we set the grasping region as  $0.4\text{ m} \times 0.4\text{ m} \times 0.2\text{ m}$  on the table. Also, a point cloud is downsampled by using three-dementional voxel grids that has a leaf size of 5 mm.

Second, a point cloud is segmented using Euclidean cluster extraction method. Segments are estimated using a Euclidean distance and a Kd-tree for finding the nearest neighbors. We choose a Euclidean distance with a cluster tolerance of 10 mm.

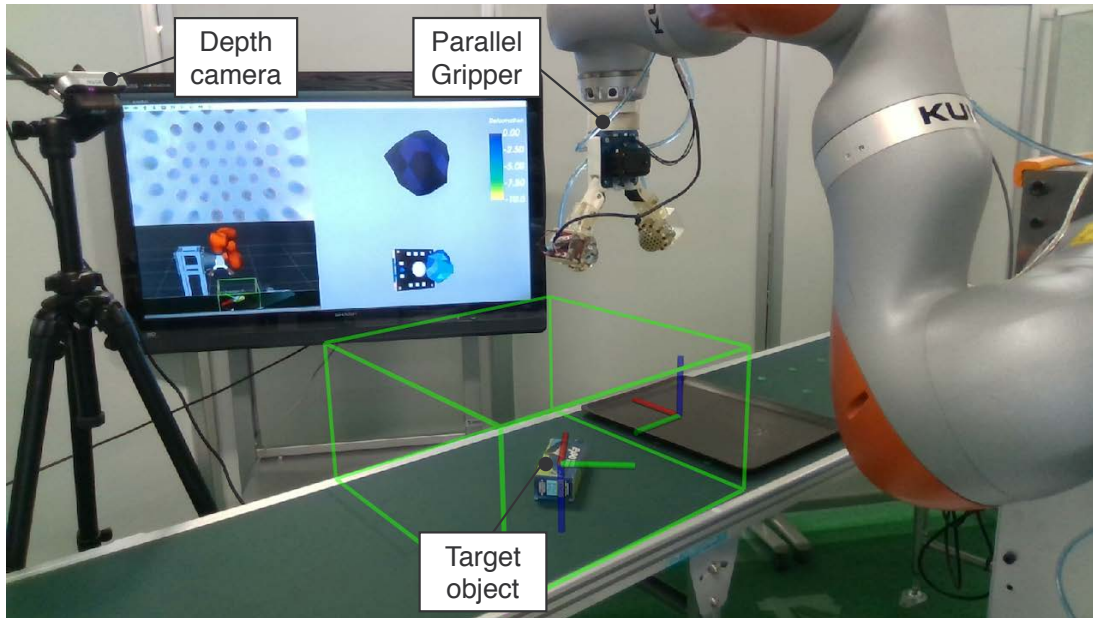


Figure 42: Experimental setup for automatic grasping system. An object inside the green bounding box is detected and stored in a storage box outside the bounding box

Finally, the object pose is estimated using Principal component analysis (PCA). Cluster points are projected to the plane of the table, then applied PCA to obtain eigenvector as the direction of the object.

The detected object posed is dealt with the lateral direction as the Y direction, and the gripper is rotated by the object's yaw angle using the manipulator.

## 5.4 Objects grasping and sensing

Fig. 44 shows the grasping and sensing procedure to test the accuracy.

A manipulator in a pre-defined neutral position moves to the recognized object position after the gripper is rotated to grasp object at the shortest direction in the XY plane. Then the gripper is being closed while acquiring tactile information. At this time, if three or more markers on the membrane have moved beyond the threshold (here that is defined by 5 mm), the gripper is stopped as reached the goal. Finally, a manipulator moves and releases the object to the storage box. The reason why we monitored three or more markers on the membrane is because





Figure 43: The depth camera with retro-reflective markers. The markers are arranged to register marker set as the origin of the camera coordinate system.

sensor noise can be filtered, and the approximate contact area can be calculated.

## 5.5 Experiment

We test the accuracy of grasping and sensing from eight daily objects with different shapes, textures and masses which are shown in Table 6. The eggshell is fragile, the toothbrush and crayon are relatively thin, the epsom salt is deformable, and the dumbbell is heavy.

We prepared two orientations for the whiteboard eraser and crayons because these objects have two types of placement which is stable.

We judge the grasping accuracy by whether it falls while picking and placing objects. Also, we judge the sensing accuracy by the joint angle reached by the gripper with grasping result.

As shown in the Fig. 45, fingertip devices move radially and stop when large membrane deformation is detected. When the gripper is first turned on, this

gripper moves to the closed position to calibrate the zero position of the gripper, and the operation range of the grippers is scaled in the range 0 to 100. Therefore, we calculate the distance between the fingertip devices as follows:

$$\frac{W_{obj}}{2} = \cos((\phi + (\theta/100) * (100 - \alpha)) * R_k + W_p + D_{mem}) \quad (5)$$

$$\alpha = 100 - (74.63 * \arccos(\frac{W_{obj} - 2 * D_{mem} - 59.20}{218.60})) - 37.38 \quad (6)$$

where:

- $\alpha$  : Position range between 0 (close) to 100 (open)
- $\theta$  : Range of motion of membrane tip (> 48.3 [deg])
- $\phi$  : Difference between knuckle and membrane tip (28.7 [deg])
- $R_k$  : Rotation radius of knuckle (109.3 [mm])
- $W_p$  : Width from the origin of the knuckle to the center (29.6 [mm])
- $W_{obj}$  : Object width
- $D_{mem}$  : Deformation depth of the membrane

Since the contacting membranes are deformed when calibration is performed, calculated  $\alpha$  is smaller than the actual value. Hence, if the object is lifted and the reached angle is larger than  $\alpha$ , we regard the sensing as successful.

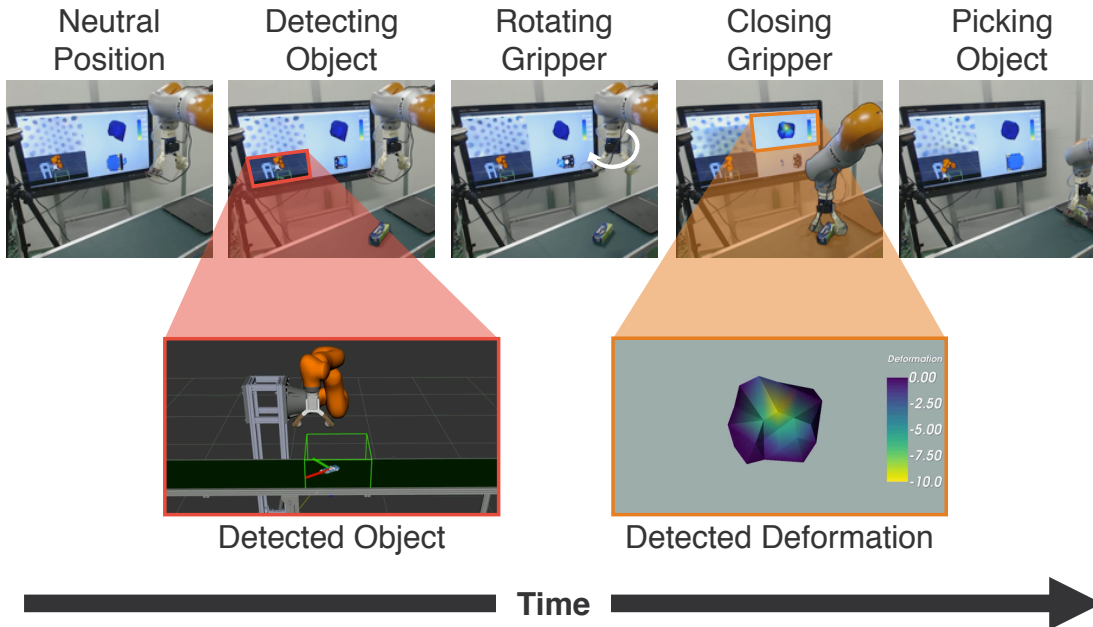


Figure 44: Chronology of the object grasping and sensing

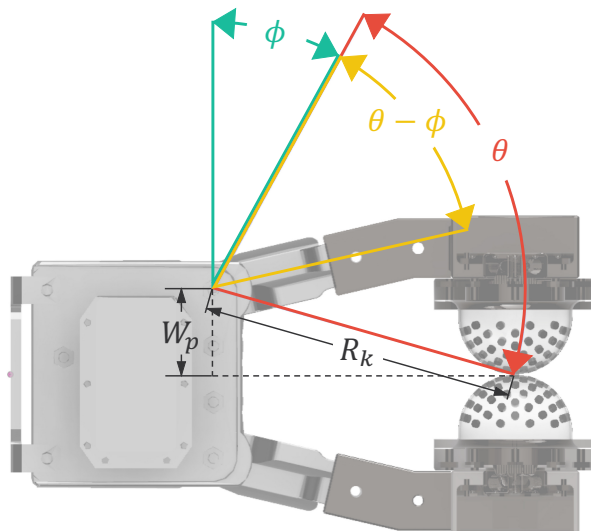




Figure 45: Joint angle limitation of the parallel gripper. Red lines show the membrane locations of the minimum and maximum.

Table 6: Target objects to test the accuracy of grasping and sensing

Objects	Eggshell	Whiteboard eraser	Toothbrush	Crayons
Images				
Weights	6 g	20 g	60 g	132 g





Objects	Wrap	Bottled water	Epsom salt	Dumbbell
Images				
Weights	393 g	484 g	896 g	1360 g

Table 7: Results of grasping and sensing accuracy

Objects	Eggshell	Whiteboard eraser	Toothbrush	Crayons
Grasping	10/10	20/20	6/10	20/20
Sensing	10/10	9/10	0/10	9/10

Objects	Wrap	Bottled water	Epsom salt	Dumbbell
Grasping	8/10	8/10	2/10	0/10
Sensing	0/10	0/10	0/10	0/10

## 5.6 Result

Table 7 and Fig. 46 shows the result of the experiments. Only the eggshell was lifted as gently using tactile sensing perfectly. The whiteboard eraser and crayons didn't fail grasping but fail sensing several times. Objects with dark texture like the wrap and dumbbell are hardly sensed. When the tactile sensing is disturbed by the texture, the gripper bends the fingers to the maximum angle, so that excessive force is applied. The wrap and bottled water were lifted under this circumstance and grasping was successful. Since the toothbrush is thin, it contacts only a part of the membrane, failing to grasp and sense. The dumbbell is dropped due to deformation of the membrane caused by dumbbell's weight.

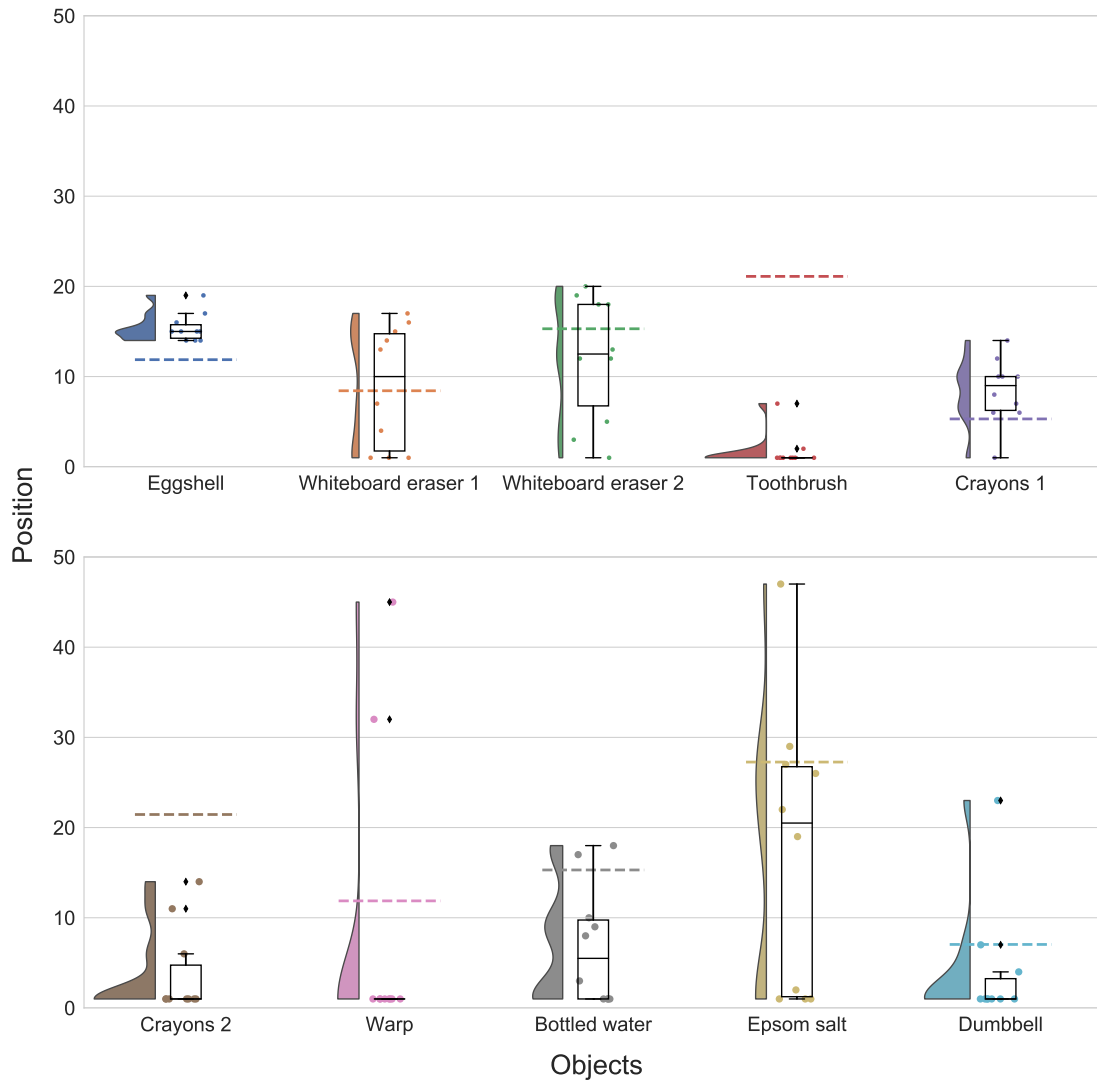


Figure 46: Sensing result from reached goal position. Scatter plots show reached goal position and dotted line shows calculated goal position using the expression Eq. 6.

## 5.7 Discussion

As a result of the experiment, sensor noise due to the influence of light from the outside and color information of the object greatly affected the grasping. Although this problem can be ignored if the object has bright and uniform texture like an egg, the combination of the current transparent film and marker recognition method is not suitable for many objects. The color information of the object is very useful and it is possible to execute tasks such as object recognition or localization and mapping within grasping. However, we should choose to cover the membrane with monochromatic film to make a large contribution to noise elimination.

Also, even when excessive force was applied to the object, we could grasp without damaging the object. This is because the pressure applied to the object becomes uniform when a fluid is used as described in the previous study that developed the fingertip filled with incompressible fluid [55].

## 6. Evaluate soft jig

### 6.1 Jig Coordinate Calibration

We performed jig coordinate calibration to evaluate the pose estimation method and convert the pose acquired from the jig into a coordinate system for the robot.

For calibration, we used a manipulator (LBR iiwa 14 R820, KUKA) to precisely control the pose of the object pressed against the jig. The robot and soft jig were arranged as shown in Fig. 47. To transform the pose of the grasped object from a robot coordinate system to a jig coordinate system, a hand-eye camera and four circular markers on the jig were used for coordinate alignment. To obtain the transformation, we solved the perspective-n-point problem [56].

Fig. 48 shows the cylindrical objects used for calibration. The robot grasps these objects and moves to the origin within a horizontal orientation in the xy-plane of the jig coordinate system, using the marker recognized by the camera. Fig. 49 shows a diagram of the motion of the robot pressing the object. The robot presses the grasped object against the jig, and the grasped object is tilted to specified angles  $\alpha$ ; however, the tilt direction of the object was changed by  $360^\circ$  within a period of  $1^\circ$  per second without using a pump to fix the object.

While changing the pose of an object, we estimated the object orientation from the jig using plane estimation [57], a point-to-plane ICP algorithm (applied to a point cloud), and the proposed point-to-function ICP algorithm (applied to a function). Here, we apply ICP algorithms with the 6-DoF and 5-DoF metrics (without rotation around the z-axis) while considering the target objects to be cylindrical.

The x-tilt  $\mathbf{Ax}$  and y-tilt  $\mathbf{Ay}$  were calculated using plane estimation, the ICP algorithms, and ground truth by projecting the normal vector of the object pose onto the yz- and xz-planes and converting them into angles.

Next, we calculated three parameters (offsets  $O_x, O_y$ , and scale  $S$ ) for cylinders with diameters of 50 mm as calibration results to obtain the correct value of the acquired tilt angle.  $Ax_j$  and  $Ay_j$  can be regarded as pure sine waves in the yz- and xz-planes, considering the tilt direction was changed by  $360^\circ$  while maintaining the angle  $\alpha$  constant in the radial direction determined by the robot. Therefore, the offsets  $O_x, O_y$ , and the scale  $S$  can be calculated using the following equations:



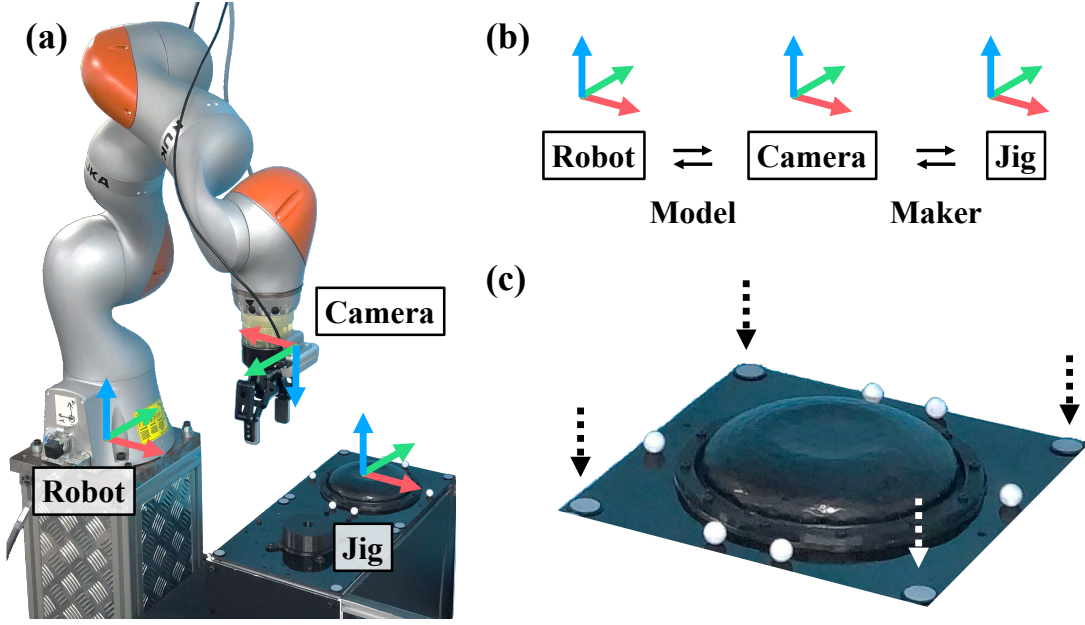


Figure 47: Experimental setup for soft jig. (a) A manipulator is used to push the object in a fixed pose. (b) Transformation relationships for each coordinate. The transformation from the robot to the camera is computed using model information and kinematics. The transformation from the camera to the jig is computed using known camera parameters and marker placement. (c) Four white circular markers at the ends of the dotted arrows align the soft jig with the robot coordinates.

$$O_x = \frac{1}{N_s} \sum_{j=1}^{N_s} Ax_j, \quad (7)$$

$$O_y = \frac{1}{N_s} \sum_{j=1}^{N_s} Ay_j, \quad (8)$$

$$S = \frac{2 \times \alpha}{\sqrt{2} \times (\sigma_x + \sigma_y)}, \quad (9)$$

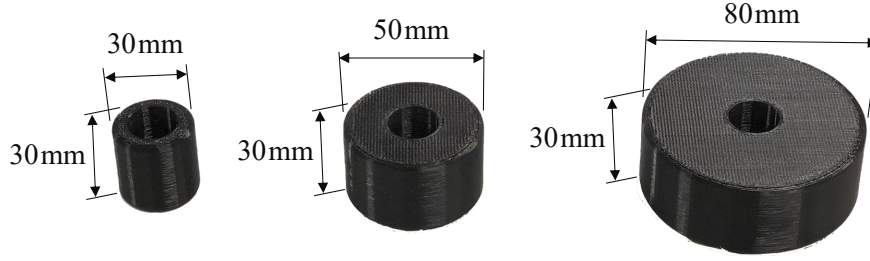


Figure 48: Three cylindrical objects with different diameters: 30 mm, 50 mm, and 80 mm. All objects have the same height of 30 mm.

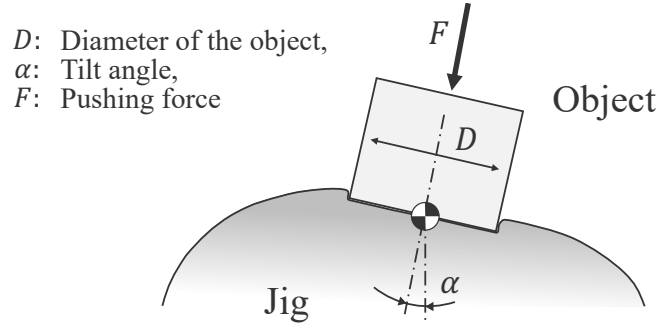


Figure 49: Illustration of the motion of the robot to press the object against the jig.

where:

$$\sigma_x = \sqrt{\frac{1}{N_s} \sum_{j=1}^{N_s} (Ax_j - O_x)^2}, \quad (10)$$

$$\sigma_y = \sqrt{\frac{1}{N_s} \sum_{j=1}^{N_s} (Ay_j - O_y)^2}, \quad (11)$$

$N_s$  is the number of samples used for calibration.

The tilt angles of a cylinder with a diameter of 50 mm acquired using plane estimation, ICP algorithms, and ground truth used as a command value to the robot are shown in Fig. 50. The tilt angles calibrated for cylinders with diameters of 50 mm using these parameters are shown in Fig. 51. The tilt angles calibrated for cylinders with diameters of 30 mm and 80 mm, using the same parameters as

those of 50 mm, are shown in Fig. 52 and Fig. 53. The RMSE for the results are listed on the right in Fig. 50–53.

We observed that the planar estimation [57] and the proposed method (5-DoF) have approximately the same results and can be estimated with high accuracy at an RMSE of less than  $4^\circ$  in Fig. 51–53. When the diameter of the object was small, the number of markers that could be referenced was small, and the pose estimation result became noisy. This is evident from the considerable noise observed in the pose estimation results at the diameter of 30 mm, where the point-to-plane ICP method failed to produce accurate estimates. However, it is clear that the proposed method improves estimation accuracy with an RMSE more than twice as large. In addition, the noise level varied depending on the estimated degrees of freedom during the pose estimation.

At a diameter of 80 mm, the residuals were larger when the tilt was large because when a large object is tilted and pressed against the jig at a large angle, a part of the bottom surface of the object lifts and loses contact with the jig.

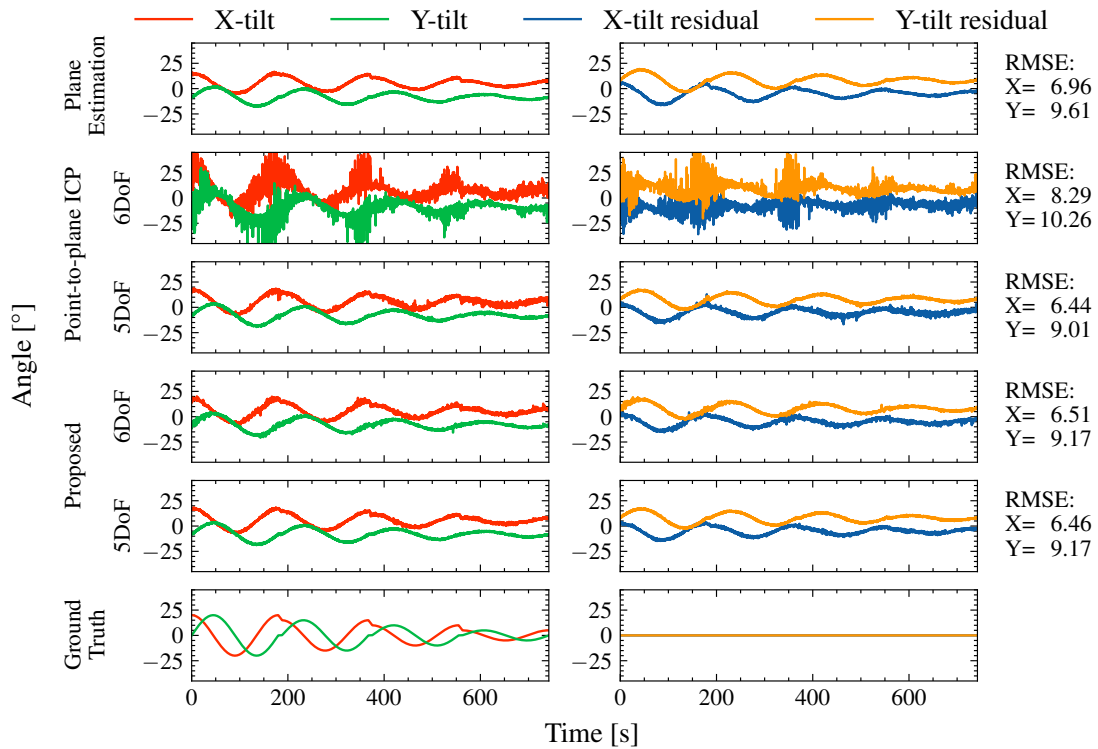


Figure 50: Tilt angles and residuals before calibration of cylinders with a diameter of 50 mm. The red and green lines denote the x- and y-tilts acquired from the jig, respectively, whereas the blue and orange lines denote the x- and y-tilt residuals from the ground truth, respectively.

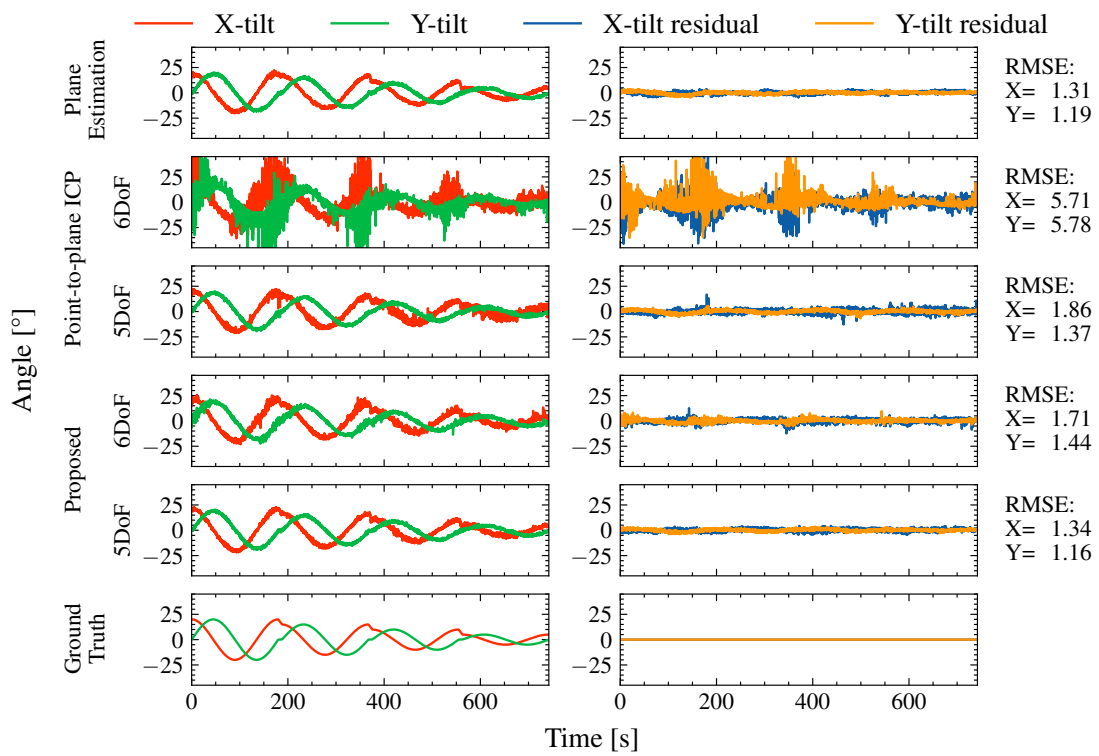


Figure 51: Estimated tilt angles and their residuals after calibration of a cylinder with a diameter of 50 mm.

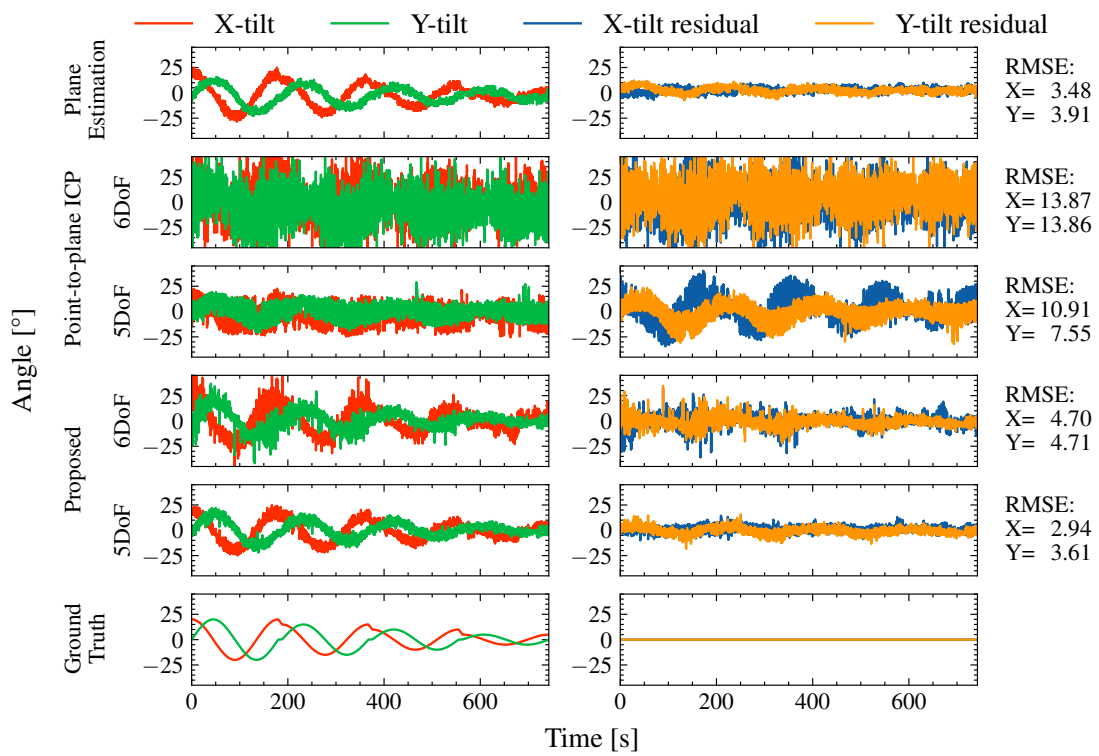


Figure 52: Estimated tilt angles and their residuals after the calibration of a cylinder with a diameter of 30 mm.

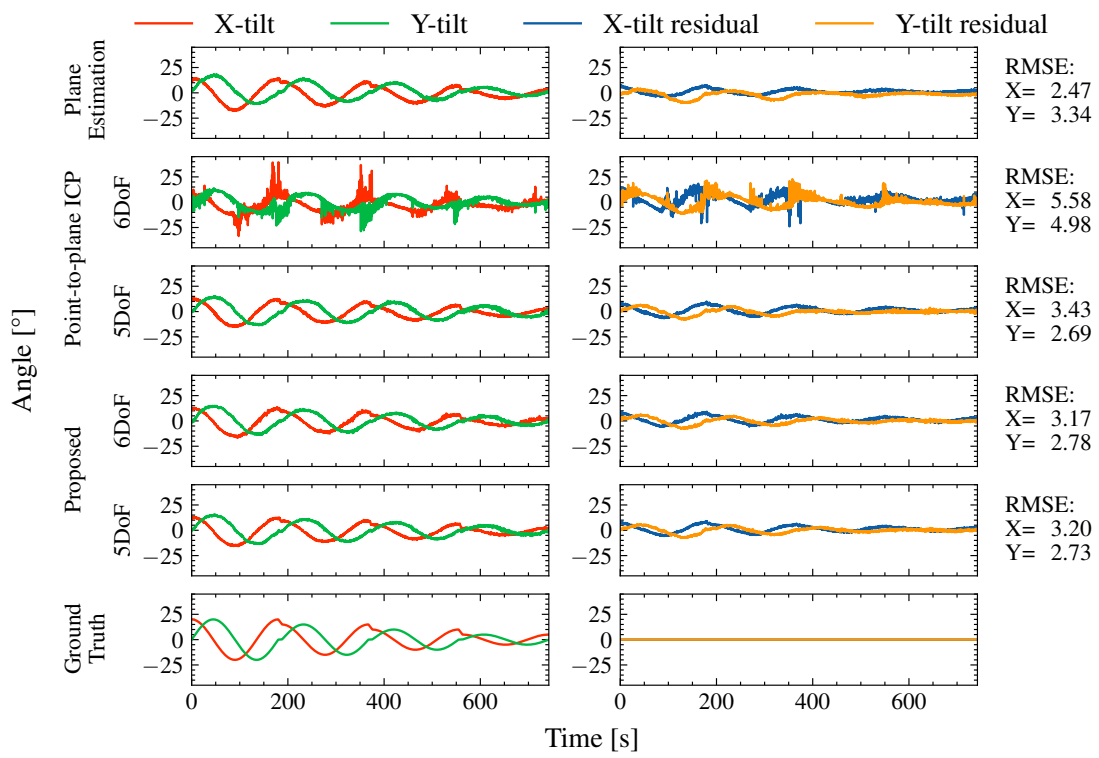


Figure 53: Estimated tilt angles and their residuals after the calibration of a cylinder with a diameter of 80 mm.

## 6.2 Pushed Object Pose Estimation

We performed pose estimation at various positions and angles to evaluate the pose estimation results when the pressed position was not at the center.

The robot grasps a cylinder with a diameter of 50 mm and moves the cylinder to the coordinates away from the center in 10 mm increments, as shown in Fig. 54. This cylinder was tilted around the y-axis by the robot to specific angles  $\alpha$  of  $5^\circ$ ,  $10^\circ$ ,  $15^\circ$ , and  $20^\circ$  from the center of the contacting bottom. The contact with the jig was determined when the force applied to the wrist of the manipulator was changed by 1 N or more. After contact detection, the robot pushed the object with a force of 5 N; the jig estimated the object pose from the jig using plane estimation [57] and the proposed point-to-function ICP algorithm (5-DoF).

Six reflective markers on the jig and four on the cylinder were measured from the top using a motion capture system (V120: Trio, OptiTrack), as shown in Fig. 55. The y-tilt of the object determined by the jig and motion capture system was calculated by projecting the normal vector of the object pose onto the xz-planes and converting it into an angle.



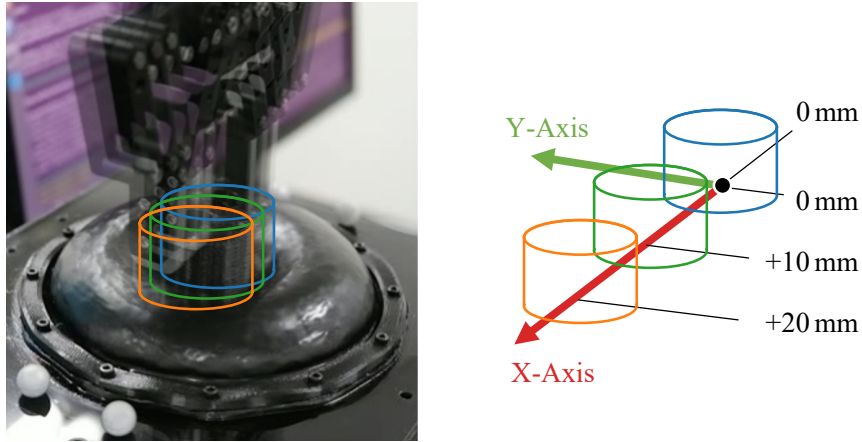


Figure 54: Variations of the positions that the robot pressed on the jig. The position is varied in 10 mm increments only in the x-axis direction in the jig coordinate system.

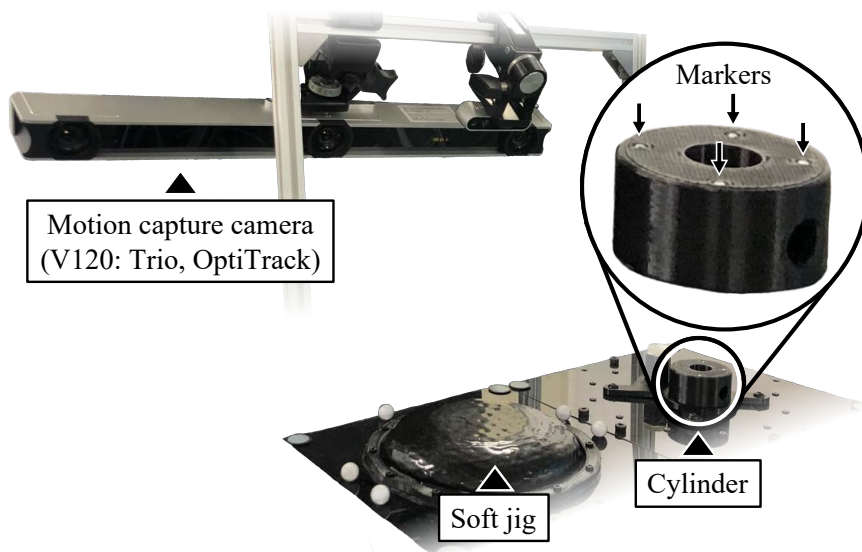


Figure 55: Setup to evaluate the estimation performance of the soft jig. A motion capture camera is mounted from above to capture a cylinder at various orientations and positions on the jig.

The results of the tilt estimation around the y-axis are shown in Fig. 56. During planar estimation, angle errors were included in the estimates as the object moved away from the center. Additionally, when the angle of the object was large, the position of the object changed when pressed with a force of 5 N, indicating that errors occur even when the object is pressed at the center. However, the proposed method compensates for this by exploiting the fact that the estimated angle values are roughly equivalent to the ground truth at an RMSE of less than  $4^\circ$  and a coefficient of determination  $R^2$  greater than 0.98, regardless of the position when the offset is between 0 mm and 10 mm. Furthermore, we confirmed that an offset larger than 20 mm includes estimation errors; however, this is not a problem because such large positioning errors are unlikely to occur in many cases under robot control of object positions.

The position estimation results in the x-direction are shown in Fig. 57. In cases of planar estimation, the position cannot be estimated; however, in the proposed method, the position is also included in the output result. Although the deviations from the ground truth occur at an RMSE of less than 6 mm when the offset is between 0 mm and 10 mm, it is possible to correct because  $R^2$  is higher than 0.92.

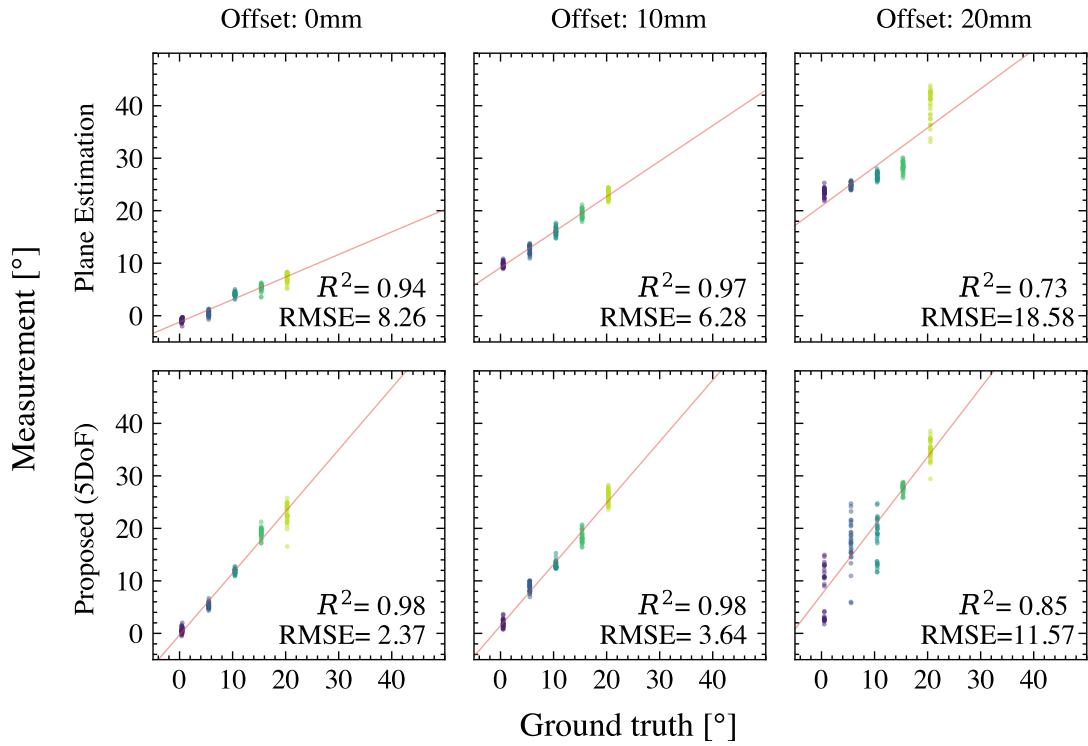


Figure 56: Tilt estimation results around the y-axis and the ground truth measured by motion capture when the position is varied from 0 mm to 20 mm and the angle is varied from 0° to 20°. The data are plotted for each pose for a period of 3 s. The red line denotes equal relation.

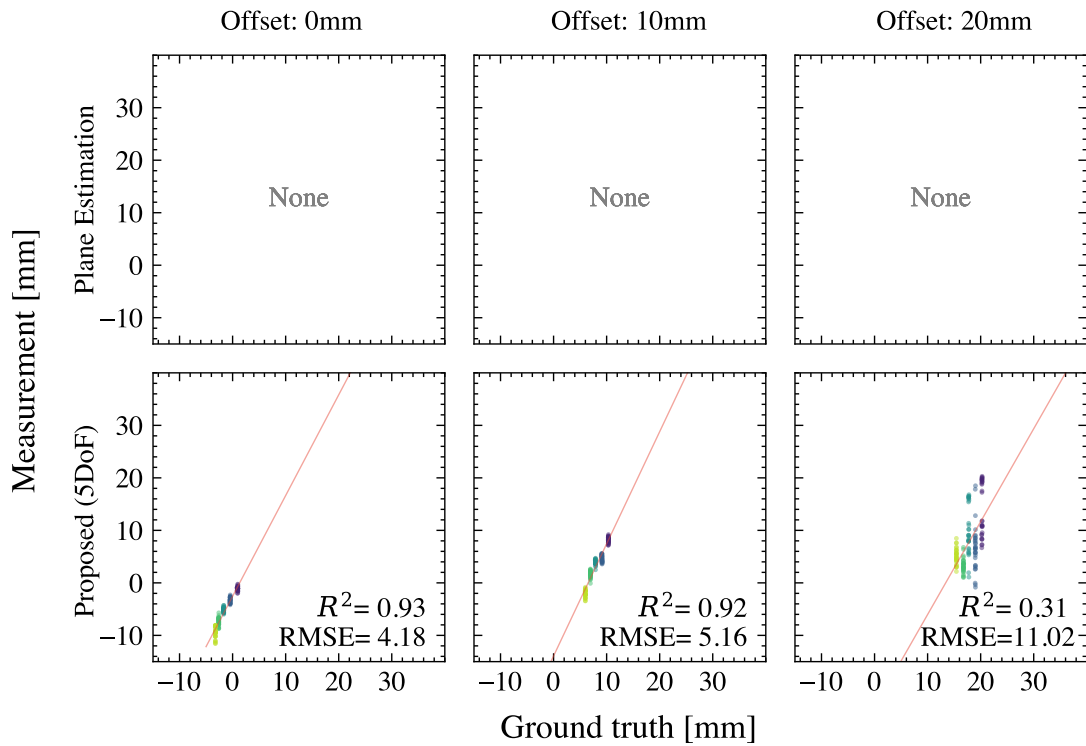


Figure 57: Position estimation results in the x-direction and the ground truth measured by motion capture when the position is varied from 0 mm to 20 mm, and the angle is varied from  $0^\circ$  to  $20^\circ$ . The data are plotted for each pose for a period of 3 s. The red line denotes equal relation.

### 6.3 Placed Object Fixing

We performed an object-fixing experiment to clarify when the pose should be estimated with the jig and to analyze the fixed pose variability caused by supporting an object with a flexible material instead of a rigid material.

The setup and procedure for pushing the object were the same as those described in Section 6.2. In this experiment, the object was pressed against the center of the jig only. After the robot pushed the object with a force of 5 N, a peristaltic pump was used to fill the soft jig with oil; pumping stopped when the liquid level limit acquired from the camera was reached.

Snapshots of the robot pushing an object and after parts fixing are shown in Fig. 58. The angle was accurately estimated when the object was pressed against it; however, as the oil was pumped out for fixation, the accuracy of the estimation decreased.

Snapshots showing the after parts fixing and the robot releasing an object are displayed in Fig. 59. The results illustrating the difference between the pushed and released poses are shown in Fig. 60. The results show that the pose of the object changed slightly when the gripper was released; however, the amount was sufficiently small to be compensated for by compliance with the remote center compliance (RCC) devices.

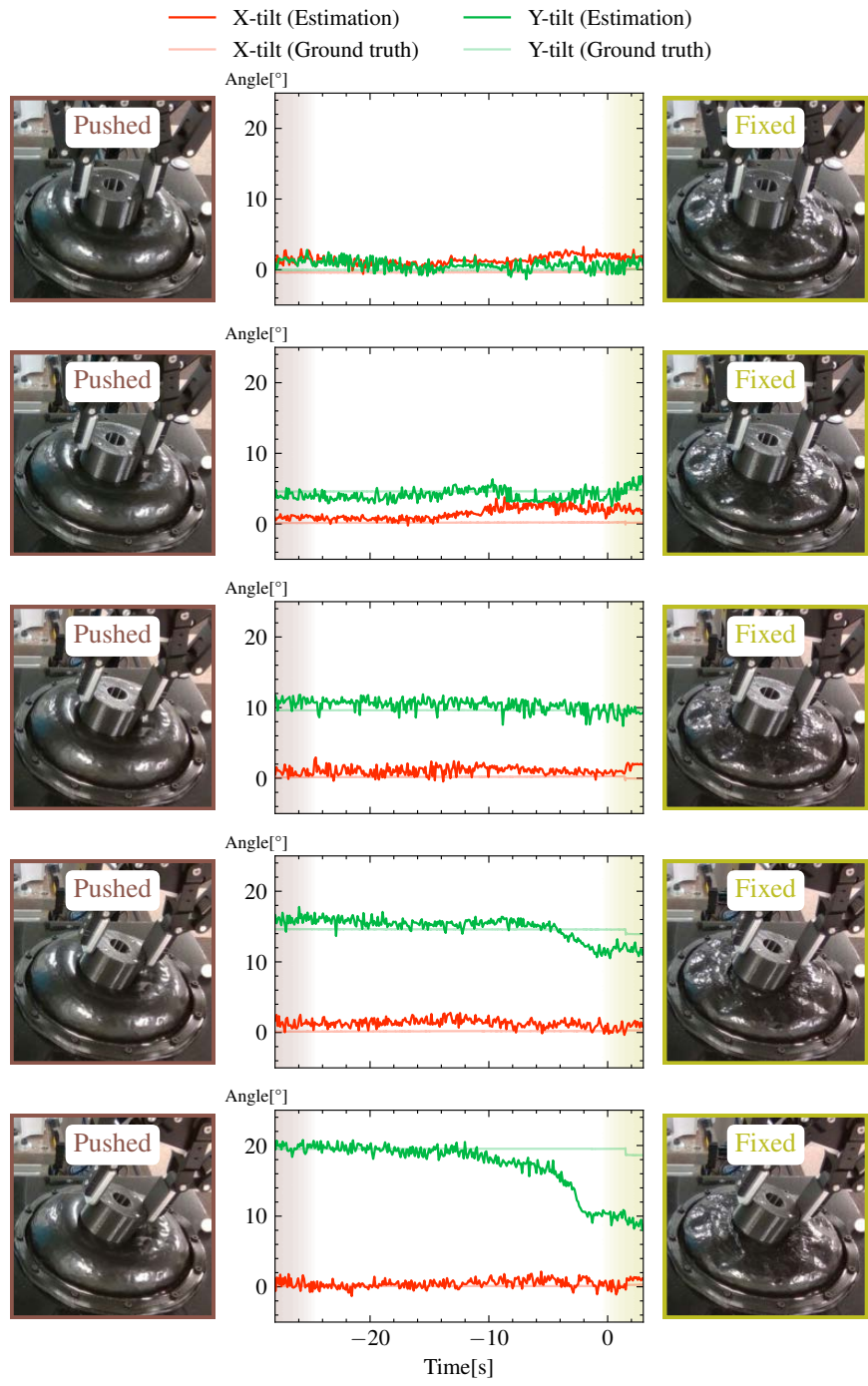


Figure 58: Estimated tilt angles from pressed to fixed.

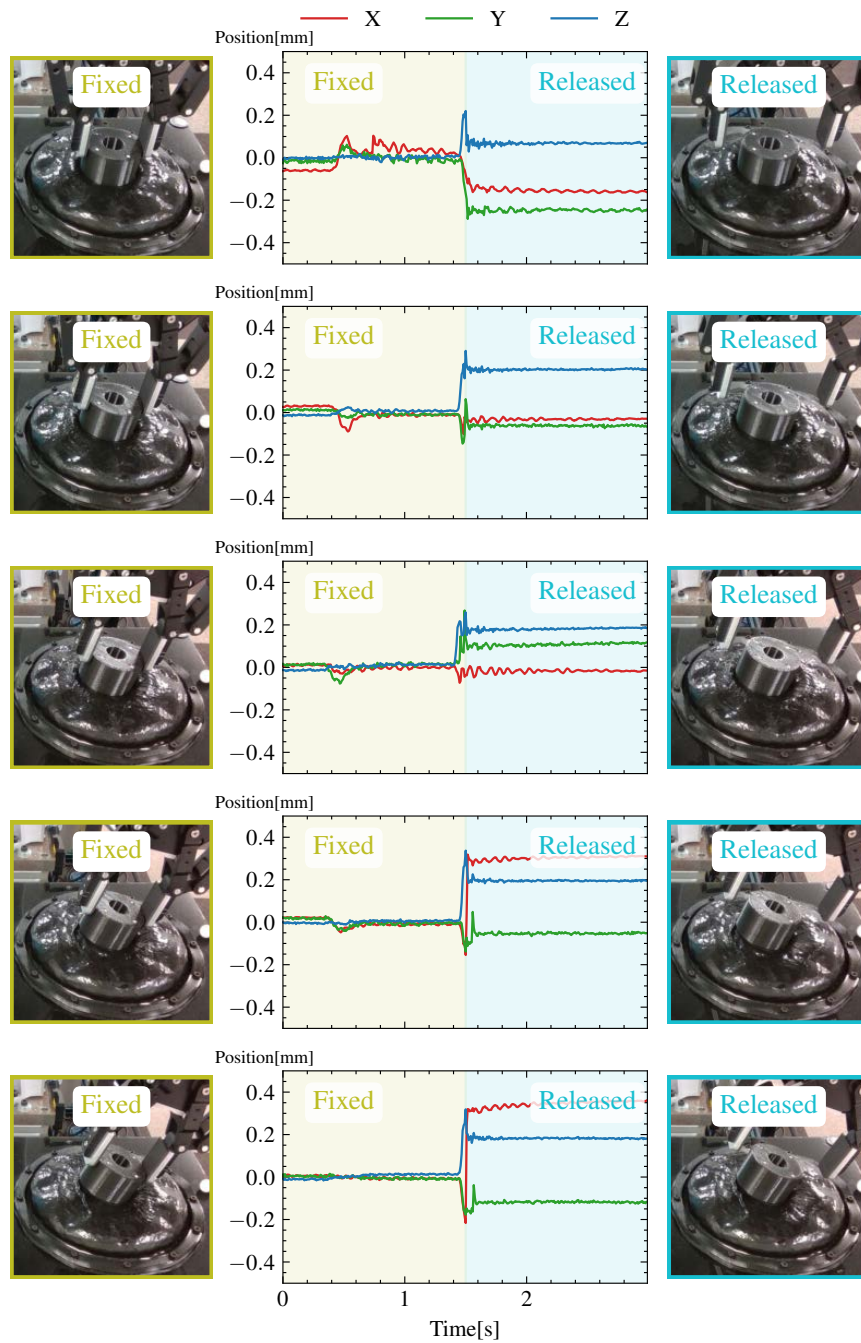


Figure 59: Displacements from pressed to released. The minute displacement after 0.5 s was caused by vibration when the robot control was switched from force control to position control.

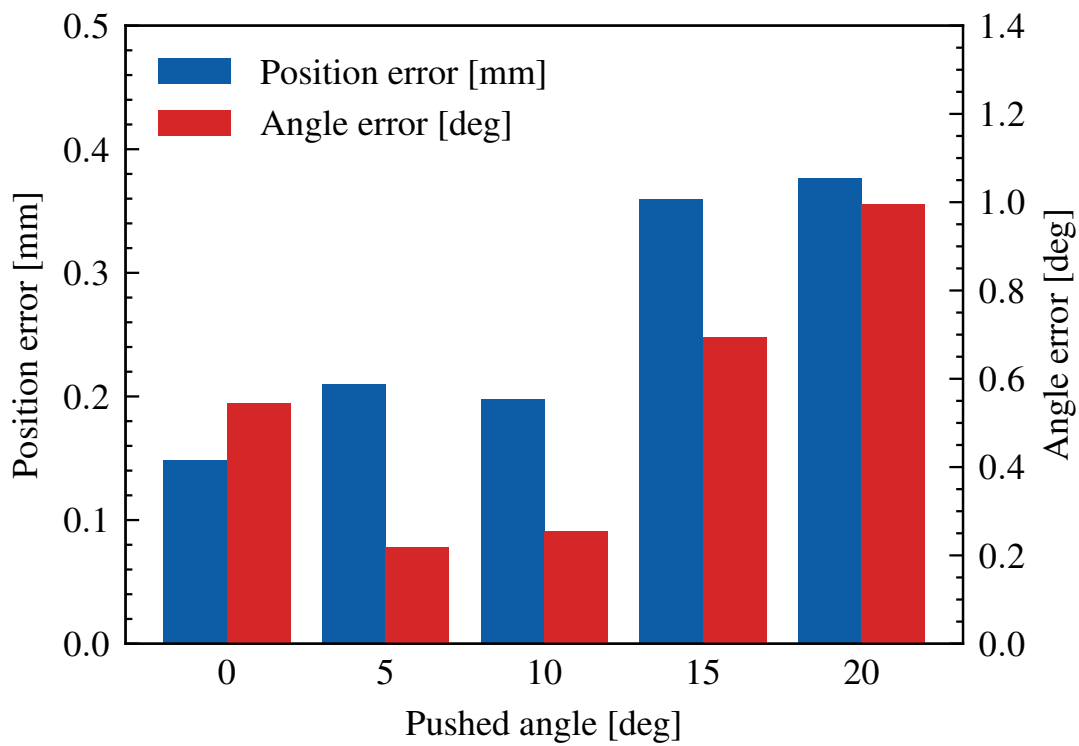


Figure 60: Difference between pushed and released pose. The pushed pose is the average of the 0–1 s timeframe in Fig. 59, and the released pose is the average of the 2–3 s timeframe in Fig. 59. The difference in position is the Euclidean distance between the two postures, and the difference in angle is calculated from the angular difference between the unit vectors when the unit vector is rotated by the two postures.



## 6.4 Fixing Force

To evaluate the effectiveness of the proposed jig in securing an object with a threaded hole, we measured the rotation angle generated during screw-tightening using the jig.

For the experiment, we used an electric screwdriver (Bosch GO 2 Professional, Bosch) with various tightening torques. The preselected torque mode (PTM) of the electric screwdriver was adjusted using a torque-presetting ring. We measured the tightening torques for different PTMs using a joint torque sensor, as shown in Fig. 61. We used pre-measured PTM-1 to PTM-3 (0.25 Nm–1.03 Nm) in our experiment.

The soft jig, screwdriver, and target object were arranged as shown in Fig. 62 (a). We followed the screw-tightening procedure before and after measuring the rotation angle of the object, as depicted in Fig. 62 (b). The procedure involved fixing the target object in place using the jig, grasping the screwdriver, and tightening the screw. We used three types of objects as targets: a circular, octagonal, and square cylinder with a nut embedded in the center and markers for motion capture. The angle of rotation of the object being measured is shown in Fig. 62 (c) and was measured using motion capture to calculate the rotation angle around the z-axis.

The experiment results are shown in Fig. 63. The x-axis of the graph shows the combination of object geometry and PTM used in the experiments, and the y-axis shows the amount of object rotation when screwing was performed.

We found that the circular and octagonal cylinders rotated during screw-tightening, even with PTM-1, because their shape provided little constraint. However, the square cylinder was fixed and screw-tightened using PTM-1. When screw tightening was performed using PTM-2 and PTM-3, the object rotated significantly from PTM-3.

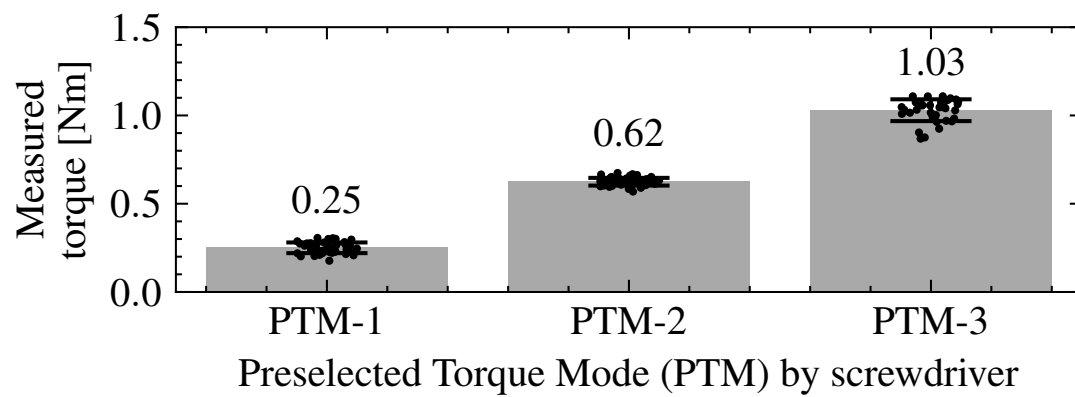


Figure 61: Measurement results of the torque exerted by the driver. The joint torque of the manipulator was used for the measurement.

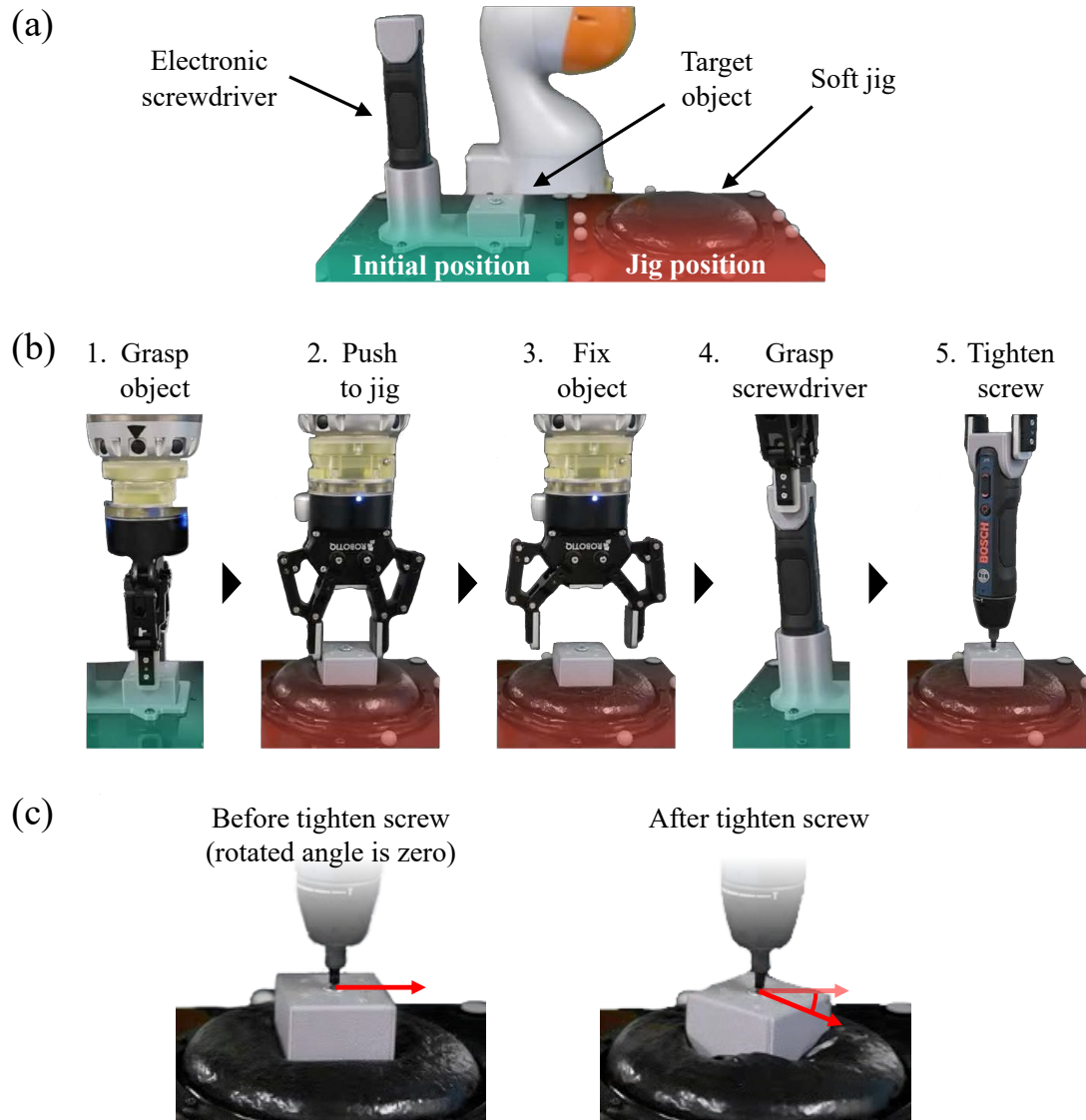


Figure 62: Screw tightening experiment. (a) Setup for the screw tightening experiment. (b) Procedure for screw tightening using a jig. (c) Angle of the object after screw tightening used for evaluation. The angle was calculated using motion capture.

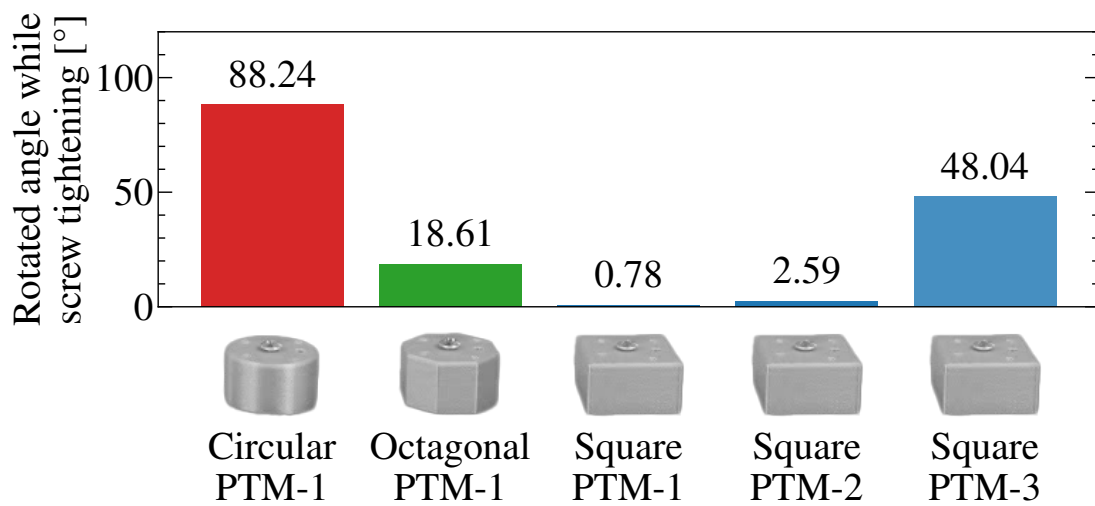


Figure 63: Rotation angle of the object during screw tightening. Each measurement value was calculated as the pose after the screw tightening procedure.

## 7. Discussion

### 7.1 Precise Estimation

The soft jig performs object pose estimation for contacted objects by acquiring the membrane shape using optical sensing and registering the object CAD model to the membrane shape.

From the results in Section 6.1, we confirmed that point-to-function ICP, which expresses the shape of the membrane as a function and estimates the object’s pose, improves the accuracy. This is because the correspondence of the points can be obtained more appropriately than if the points were used directly to estimate the object pose. We also confirmed that changing the number of pose estimation parameters from 6-DoF to 5-DoF when using a cylindrical object improves the accuracy, indicating the importance of limiting the DoF of the estimation according to the object shape.

From the results in Section 6.3, we confirmed that highly accurate orientation estimation can be achieved using the estimation result before fixation instead of that after fixation. The pose estimation converges correctly because the oil increases the shape difference between the object contact region and the object non-contact region.

### 7.2 Hardware Limitations for Sensing

Section 6.1 shows that there are limitations to the estimated allowable tilt angle and size of the soft jig. To address these limitations and improve performance, adjustments to the jig’s diameter and the volume of the membrane interior may be necessary.

The current marker size of 5 mm and the distance between the markers on the membrane of approximately 10 mm pose accuracy challenges in object pose estimation. For instance, a cylinder with a diameter of 30 mm has only about seven reference markers. To enhance the accuracy, we propose reducing the marker size and distance by half, which would increase the number of reference points to 19.

Alternatively, we could improve pose estimation accuracy by introducing a mechanism that can change the membrane’s color to visible or invisible, as shown

in a previous study [58]. Another option would be to use multi-color illumination techniques [9][59] to minimize the uncertainty of the pose estimation process.

### **7.3 Hardware Limitation for Fixing**

The results in Section 6.3 demonstrate that the proposed jig successfully placed objects with high accuracy. Moreover, the jig can be used for re-grasping to further improve the gripper’s object grasping posture, as demonstrated in a previous study [60].

However, the results in Section 6.4 reveal challenges in constraining objects using the proposed jig. This is because the jig relies on a form closure, which utilizes the shape of the object to constrain it, rather than a force closure, which applies a force to constrain the object. To determine the effectiveness of form closure for fixing an object, it would be helpful to analyze the CAD model of the object being fixed and examine the distribution of normal directions on each face of the CAD model. Nevertheless, it is worth noting that the mechanical clutch was activated during screw tightening, and the screw was tightened to the specified torque. This can be attributed to the frictional effect of the flexible membrane on the jig.

## 8. Conclusion

In this research, we developed a new grasping mechanism as robotic skin combining both object holding using the jamming transition and optical sensing function.

We showed experimentally that a prototype of grippers could measure deformation of the membrane by tracking the markers embedded in it. And, we could grasp cylindrical and rectangular objects while tracking deformation of the universal gripper. Importantly, these capabilities for tactile information provision and variable stiffness are retained even when the device is scaled to fit either smaller parallel gripper or larger jig.

As for future research directions, performance enhancements and sensory expansions are actively being considered. As shown in Table 8, only shape and pose are currently acquired, but other perceptual parameters can be achieved by improving the hardware and system, and by adding sensors. These implementations would allow for further development of grasping strategies.

Looking ahead, the technology discussed in this thesis has the potential to be extended to cover a robot’s entire body. This holistic approach would not only augment localized grasping but also provide new opportunities for whole-body tactile sensing and interactive functionalities. The groundwork established by this study serves as a valuable stepping stone for both theoretical and practical advancements in robotic grasping and sensory capabilities.

<b>Perceptual Parameter</b>	<b>Capability of Proposed Skin</b>	<b>Potential Extension</b>
Shape	Accessible	Higher density can be achieved by replacing round markers with patterns [61]
Pose	Accessible	Higher accuracy can be achieved by machine learning technique[62]
Temperature	Inaccessible	Temperature can be measured by using thermo-sensitive paint to color the marker [63]
Pressure	Inaccessible	Pressure can be measured by sensing the internal oil state with a pressure sensor [64]
Vibration	Inaccessible	Vibration can be measured using a pressure sensor [65]
Texture	Inaccessible	Texture can be measured by pressure analysis [65] or by image processing using the transparent membrane [66]
Proximity	Inaccessible	Proximity can be measured by image processing using the transparent membrane [14]
Rigidity	Inaccessible	Rigidity (or hardness) can be estimated using internal pressure and shape changes [22]
Force/Torque	Inaccessible	Force and Torque can be estimated using internal pressure and shape changes [9]

Table 8: Capabilities of proposed skin in acquiring tactile information and potential extensions



## Acknowledgements

I would like to express my deepest gratitude to my supervisor, Professor Takamitsu Matsubara. His support was not only invaluable during my third year in the Doctoral program at the Robot Learning Laboratory, but also continued after my graduation. I also wish to extend my thanks to Professor Takahiro Wada, who provided me with support during my second year in the Doctoral program at the Human Robotics Laboratory, and to Professor Tsukasa Ogasawara, who assisted me during my Master's program and my first year in the Doctoral program at the Robotics Laboratory. I am grateful to all the Thesis Committee members: Assistant Professor Takuya Kiyokawa and Assistant Professor Hikaru Sasaki for their thoughtful comments for improving this thesis. I would also like to thank my colleagues and all the members of the Robotics Laboratory, Human Robotics Laboratory, and Robot Learning Laboratory who encouraged me. I couldn't complete this thesis without their support.

Finally, I must express my very profound gratitude to my parents for their understanding and support during my years of study.

## References

- [1] A. Billard and D. Kragic, Trends and challenges in robot manipulation, *Science*, vol. 364, no. 6446, p. eaat8414, 2019.
- [2] J. Hughes, U. Culha, F. Giardina, F. Guenther, A. Rosendo, and F. Iida, Soft manipulators and grippers: a review, *Frontiers in Robotics and AI*, vol. 3, p. 69, 2016.
- [3] J. R. Amend, E. Brown, N. Rodenberg, H. M. Jaeger, and H. Lipson, A positive pressure universal gripper based on the jamming of granular material, *IEEE Transactions on Robotics*, vol. 28, no. 2, pp. 341–350, 2012.
- [4] Z. Kappassov, J.-A. Corrales, and V. Perdereau, Tactile sensing in dexterous robot hands, *Robotics and Autonomous Systems*, vol. 74, pp. 195–220, 2015.
- [5] S. Luo, J. Bimbo, R. Dahiya, and H. Liu, Robotic tactile perception of object properties: A review, *Mechatronics*, vol. 48, pp. 54–67, 2017.
- [6] Y. Tenzer, L. P. Jentoft, and R. D. Howe, The feel of mems barometers: Inexpensive and easily customized tactile array sensors, *IEEE Robotics and Automation Magazine*, vol. 21, no. 3, pp. 89–95, 2014.
- [7] T. P. Tomo, A. Schmitz, W. K. Wong, H. Kristanto, S. Somlor, J. Hwang, L. Jamone, and S. Sugano, Covering a robot fingertip with uskin: A soft electronic skin with distributed 3-axis force sensitive elements for robot hands, *IEEE Robotics and Automation Letters*, vol. 3, no. 1, pp. 124–131, 2018.
- [8] K. Shimonomura, Tactile image sensors employing camera: A review, *Sensors*, vol. 19, no. 18, 2019.
- [9] W. Yuan, S. Dong, and E. H. Adelson, Gelsight: High-resolution robot tactile sensors for estimating geometry and force, *Sensors*, vol. 17, no. 12, p. 2762, 2017.
- [10] E. Donlon, S. Dong, M. Liu, J. Li, E. Adelson, and A. Rodriguez, Gelslim: A high-resolution, compact, robust, and calibrated tactile-sensing finger, *Proceedings of the IEEE International Conference on Intelligent Robots and Systems*, pp. 1927–1934, 2018.

- [11] D. Ma, E. Donlon, S. Dong, and A. Rodriguez, Dense tactile force estimation using gelslim and inverse fem, in *Proceedings of the IEEE International Conference on Robotics and Automation (ICRA)*, 2019, pp. 5418–5424.
- [12] I. H. Taylor, S. Dong, and A. Rodriguez, Gelslim 3.0: High-resolution measurement of shape, force and slip in a compact tactile-sensing finger, in *Proceedings of the IEEE International Conference on Robotics and Automation (ICRA)*, 2022, pp. 10 781–10 787.
- [13] B. Ward-Cherrier, N. Pestell, L. Cramphorn, B. Winstone, M. E. Giannacini, J. Rossiter, and N. F. Lepora, The tactip family: Soft optical tactile sensors with 3d-printed biomimetic morphologies, *Soft Robotics*, vol. 5, no. 2, pp. 216–227, 2018.
- [14] A. Yamaguchi and C. G. Atkeson, Combining finger vision and optical tactile sensing: Reducing and handling errors while cutting vegetables, *Proceedings of the IEEE International Conference on Humanoid Robots*, pp. 1045–1051, 2016.
- [15] J. Ueda, Y. Ishida, M. Kondo, and T. Ogasawara, Development of the naist-hand with vision-based tactile fingertip sensor, *Proceedings of the IEEE International Conference on Robotics and Automation*, pp. 2332–2337, 2005.
- [16] A. Alspach, K. Hashimoto, N. Kuppuswamy, and R. Tedrake, Soft-bubble: A highly compliant dense geometry tactile sensor for robot manipulation, in *Proceedings of the IEEE International Conference on Soft Robotics (RoboSoft)*, 2019, pp. 597–604.
- [17] N. Kuppuswamy, A. Alspach, A. Uttamchandani, S. Creasey, T. Ikeda, and R. Tedrake, Soft-bubble grippers for robust and perceptive manipulation, in *Proceedings of the IEEE International Conference on Intelligent Robots and Systems (IROS)*, 2020, pp. 9917–9924.
- [18] X. Lin, L. Willemet, A. Bailleul, and M. Wiertlewski, Curvature sensing with a spherical tactile sensor using the color-interference of a marker array, in *Proceedings of the IEEE International Conference on Robotics and Automation (ICRA)*, 2020, pp. 603–609.

- [19] J. W. James, N. Pestell, and N. F. Lepora, Slip detection with a biomimetic tactile sensor, *IEEE Robotics and Automation Letters*, vol. 3, no. 4, pp. 3340–3346, 2018.
- [20] J. Li, S. Dong, and E. Adelson, Slip detection with combined tactile and visual information, *Proceedings of the IEEE International Conference on Robotics and Automation*, pp. 7772–7777, 2018.
- [21] A. Yamaguchi and C. G. Atkeson, Implementing tactile behaviors using finger-vision, *Proceedings of the IEEE International Conference on Humanoid Robots*, pp. 241–248, 2017.
- [22] W. Yuan, C. Zhu, A. Owens, M. A. Srinivasan, and E. H. Adelson, Shape-independent hardness estimation using deep learning and a gelsight tactile sensor, *Proceedings of the IEEE International Conference on Robotics and Automation*, pp. 951–958, 2017.
- [23] R. Calandra, A. Owens, D. Jayaraman, J. Lin, W. Yuan, J. Malik, E. H. Adelson, and S. Levine, More than a feeling: Learning to grasp and regrasp using vision and touch, *IEEE Robotics and Automation Letters*, vol. 3, no. 4, pp. 3300–3307, 2018.
- [24] F. R. Hogan, M. Bauza, O. Canal, E. Donlon, and A. Rodriguez, Tactile re-grasp: Grasp adjustments via simulated tactile transformations, *Proceedings of the IEEE International Conference on Intelligent Robots and Systems*, pp. 2963–2970, 2018.
- [25] G. Pang, G. Yang, and Z. Pang, Review of robot skin: A potential enabler for safe collaboration, immersive teleoperation, and affective interaction of future collaborative robots, *IEEE Transactions on Medical Robotics and Bionics*, vol. 3, no. 3, pp. 681–700, 2021.
- [26] F. Liu, S. Deswal, A. Christou, Y. Sandamirskaya, M. Kaboli, and R. Dahiya, Neuro-inspired electronic skin for robots, *Science Robotics*, vol. 7, no. 67, p. eabl7344, 2022.

- [27] A. Schmitz, P. Maiolino, M. Maggiali, L. Natale, G. Cannata, and G. Metta, Methods and technologies for the implementation of large-scale robot tactile sensors, *IEEE Transactions on Robotics*, vol. 27, no. 3, pp. 389–400, 2011.
- [28] G. Cheng, E. Dean-Leon, F. Bergner, J. Rogelio Guadarrama Olvera, Q. Leboutet, and P. Mittendorf, A comprehensive realization of robot skin: Sensors, sensing, control, and applications, *Proceedings of the IEEE*, vol. 107, no. 10, pp. 2034–2051, 2019.
- [29] L. Van Duong and V. A. Ho, Large-scale vision-based tactile sensing for robot links: Design, modeling, and evaluation, *IEEE Transactions on Robotics*, vol. 37, no. 2, pp. 390–403, 2021.
- [30] Y. Zhang, G. Zhang, Y. Du, and M. Yu Wang, Vtacarm. a vision-based tactile sensing augmented robotic arm with application to human-robot interaction, in *Proceedings of the IEEE International Conference on Automation Science and Engineering (CASE)*, 2020, pp. 35–42.
- [31] M. Guo, D. V. Gealy, J. Liang, J. Mahler, A. Goncalves, S. McKinley, J. A. Ojea, and K. Goldberg, Design of parallel-jaw gripper tip surfaces for robust grasping, *Proceedings of the IEEE International Conference on Robotics and Automation*, pp. 2831–2838, 2017.
- [32] K. Mizushima, T. Nishimura, Y. Suzuki, T. Tsuji, and T. Watanabe, Surface texture of deformable robotic fingertips for a stable grasp under both dry and wet conditions, *IEEE Robotics and Automation Letters*, vol. 2, no. 4, pp. 2048–2055, 2017.
- [33] J. Amend and H. Lipson, The jamhand: Dexterous manipulation with minimal actuation, *Soft robotics*, vol. 4, no. 1, pp. 70–80, 2017.
- [34] Y. Tsugami, T. Barbié, K. Tadakuma, and T. Nishida, Development of universal parallel gripper using reformed magnetorheological fluid, *Proceedings of the 2017 Asian Control Conference*, pp. 778–783, 2017.
- [35] H. Asada and A. By, Kinematic analysis of workpart fixturing for flexible assembly with automatically reconfigurable fixtures, *IEEE Journal on Robotics and Automation*, vol. 1, no. 2, pp. 86–94, 1985.

- [36] A. Gameros, S. Lowth, D. Axinte, A. Nagy-Sochacki, O. Craig, and H. Siller, State-of-the-art in fixture systems for the manufacture and assembly of rigid components: A review, *International Journal of Machine Tools and Manufacture*, vol. 123, pp. 1–21, 2017.
- [37] M. V. Gandhi and B. S. Thompson, Automated design of modular fixtures for flexible manufacturing systems, *Journal of Manufacturing Systems*, vol. 5, no. 4, pp. 243–252, 1986.
- [38] C. Yi and G. A. Bekey, Assembly planning for modular fixtures, in *Proceedings of the IEEE International Conference on Intelligent Robots and Systems (IROS)*, vol. 2, 1996, pp. 704–711.
- [39] S. Lu, Z. Ahmad, M. Zoppi, X. Ding, D. Zlatanov, and R. Molfino, Design and testing of a highly reconfigurable fixture with lockable robotic arms, *Journal of Mechanical Design*, vol. 138, no. 8, pp. 1–8, 2016.
- [40] R. Müller, M. Esser, and M. Vette, Reconfigurable handling systems as an enabler for large components in mass customized production, *Journal of Intelligent Manufacturing*, vol. 24, no. 5, pp. 977–990, 2013.
- [41] G. Levi, Y. Golan, and A. Shapiro, Simjig - smart independent minimalist jig, *IEEE Robotics and Automation Letters*, vol. 7, no. 2, pp. 3396–3403, 2022.
- [42] A. Mo and W. Zhang, A novel universal gripper based on meshed pin array, *International Journal of Advanced Robotic Systems*, vol. 16, no. 2, pp. 1–12, 2019.
- [43] P. Shi, Z. Hu, K. Nagata, W. Wan, Y. Domae, and K. Harada, Development of a shape-memorable adaptive pin array fixture, *Advanced Robotics*, vol. 35, no. 10, pp. 591–602, 2021.
- [44] J. W. Park, J. Park, H. Kim, N. Kim, and D. Y. Kim, Assembly part positioning on transformable pin array fixture by active pin maximization and joining point alignment, *IEEE Transactions on Automation Science and Engineering*, vol. 19, no. 2, pp. 1047–1057, 2022.

- [45] T. Kiyokawa, T. Sakuma, J. Takamatsu, and T. Ogasawara, Soft-jig-driven assembly operations, in *Proceedings of the IEEE International Conference on Robotics and Automation (ICRA2021)*, 2021, pp. 3466–3472.
- [46] A. Rubio-Mateos, M. Casuso, A. Rivero, E. Ukar, and A. Lamikiz, Vibrations characterization in milling of low stiffness parts with a rubber-based vacuum fixture, *Chinese Journal of Aeronautics*, vol. 34, no. 6, pp. 54–66, 2021.
- [47] J. Hughes and F. Iida, Localized differential sensing of soft deformable surfaces, *Proceedings of the IEEE International Conference on Robotics and Automation*, pp. 4959–4964, 2017.
- [48] J. Hughes and F. Iida, Tactile sensing applied to the universal gripper using conductive thermoplastic elastomer, *Soft Robotics*, vol. 5, no. 5, pp. 512–526, 2018.
- [49] B. Ward-Cherrier, L. Cramphorn, and N. F. Lepora, Exploiting sensor symmetry for generalized tactile perception in biomimetic touch, *IEEE Robotics and Automation Letters*, vol. 2, no. 2, pp. 1218–1225, 2017.
- [50] Z. Zhang, A flexible new technique for camera calibration, *IEEE Transactions on Pattern Analysis and Machine Intelligence*, vol. 22, 2000.
- [51] A. Fitzgibbon, M. Pilu, and R. B. Fisher, Direct least square fitting of ellipses, *IEEE Transactions on Pattern Analysis and Machine Intelligence*, vol. 21, no. 5, pp. 476–480, 1999.
- [52] J. Amend, N. Cheng, S. Fakhouri, and B. Culley, Soft robotics commercialization: Jamming grippers from research to product, *Soft Robotics*, vol. 3, no. 4, pp. 213–222, 2016.
- [53] J. Gómez-Paccapelo, A. Santarossa, H. Bustos, and L. Pugnali, Effect of the granular material on the maximum holding force of a granular gripper, *Granular Matter*, vol. 23, no. 4, pp. 1–6, 2021.
- [54] J. J. Moré, The levenberg-marquardt algorithm: implementation and theory, in *Numerical analysis*, 1978, pp. 105–116.

- [55] T. Nishimura, K. Mizushima, Y. Suzuki, T. Tsuji, and T. Watanabe, Variable-grasping-mode underactuated soft gripper with environmental contact-based operation, *IEEE Robotics and Automation Letters*, vol. 2, no. 2, pp. 1164–1171, 2017.
- [56] V. Lepetit, F. Moreno-Noguer, and P. Fua, Epnp: An accurate  $\mathcal{O}(n)$  solution to the pnp problem, *International Journal of Computer Vision*, vol. 81, no. 2, pp. 155–166, 2009.
- [57] T. Sakuma, T. Kiyokawa, J. Takamatsu, T. Wada, and T. Ogasawara, Soft-jig: A flexible sensing jig for simultaneously fixing and estimating orientation of assembly parts, in *Proceedings of the IEEE International Conference on Robotics and Automation (ICRA)*, 2022, pp. 10 945–10 950.
- [58] F. R. Hogan, M. Jenkin, S. Rezaei-Shoshtari, Y. Girdhar, D. Meger, and G. Dudek, Seeing through your skin: Recognizing objects with a novel visuotactile sensor, in *Proceedings of the IEEE/CVF Winter Conference on Applications of Computer Vision (WACV)*, 2021, pp. 1218–1227.
- [59] S. Li, X. Yin, C. Xia, L. Ye, X. Wang, and B. Liang, Tata: a universal jamming gripper with high-quality tactile perception and its application to underwater manipulation, in *Proceedings of the IEEE International Conference on Robotics and Automation (ICRA)*, 2022, pp. 6151–6157.
- [60] Z. Hu, W. Wan, K. Koyama, and K. Harada, Reducing uncertainty using placement and regrasp planning on a triangular corner fixture, *IEEE Transactions on Automation Science and Engineering*, pp. 1–19, 2023.
- [61] W. K. Do, B. Jurewicz, and M. Kennedy, Densetact 2.0: Optical tactile sensor for shape and force reconstruction, in *Proceedings of the IEEE International Conference on Robotics and Automation (ICRA)*, 2023, pp. 12 549–12 555.
- [62] M. Bauza, O. Canal, and A. Rodriguez, Tactile mapping and localization from high-resolution tactile imprints, in *Proceedings of the IEEE International Conference on Robotics and Automation (ICRA)*, 2019, pp. 3811–3817.



- [63] K. Sato, H. Shinoda, and S. Tachi, Finger-shaped thermal sensor using thermo-sensitive paint and camera for telexistence, in *Proceedings of the IEEE International Conference on Robotics and Automation (ICRA)*, 2011, pp. 1120–1125.
- [64] R. Adachi, Y. Fujihira, and T. Watanabe, Identification of danger state for grasping delicate tofu with fingertips containing viscoelastic fluid, *Proceedings of the IEEE International Conference on Intelligent Robots and Systems (IROS)*, pp. 497–503, 2015.
- [65] N. Komeno and T. Matsubara, Tactile perception based on injected vibration in soft sensor, *IEEE Robotics and Automation Letters*, vol. 6, no. 3, pp. 5365–5372, 2021.
- [66] R. Li and E. H. Adelson, Sensing and recognizing surface textures using a gelsight sensor, in *The IEEE Conference on Computer Vision and Pattern Recognition (CVPR)*, 2013, pp. 1241–1247.